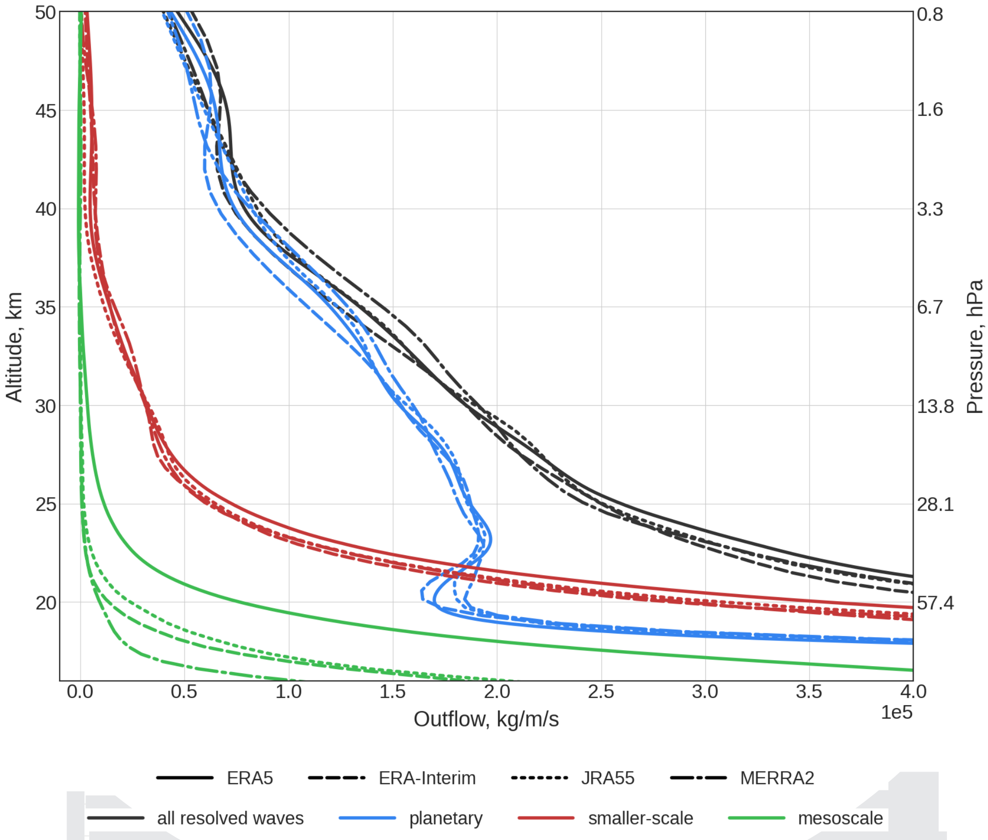

Dynamical drivers of deep and shallow branches in the stratospheric circulation and transport

Rasul-Akhun Baikhadzhaev

Energie & Umwelt / Energy & Environment
Band / Volume 735
ISBN 978-3-95806-997-8

Mitglied der Helmholtz-Gemeinschaft

JÜLICH Forschungszentrum

Schriften des Forschungszentrums Jülich
Reihe Energie & Umwelt / Energy & Environment Band / Volume 735

Forschungszentrum Jülich GmbH
Institute of Climate and Energy Systems (ICE)
Stratosphäre (ICE-4)

Dynamical drivers of deep and shallow branches in the stratospheric circulation and transport

Rasul-Akhun Baikhadzhaev

Schriften des Forschungszentrums Jülich
Reihe Energie & Umwelt / Energy & Environment Band / Volume 735

ISSN 1866-1793 ISBN 978-3-95806-997-8

Bibliografische Information der Deutschen Nationalbibliothek.
Die Deutsche Nationalbibliothek verzeichnet diese Publikation in der Deutschen Nationalbibliografie; detaillierte Bibliografische Daten sind im Internet über http://dnb.d-nb.de abrufbar.

Herausgeber und Vertrieb:	Forschungszentrum Jülich GmbH Zentralbibliothek, Verlag 52425 Jülich Tel.: +49 2461 61-5368 Fax: +49 2461 61-6103 zb-publikation@fz-juelich.de www.fz-juelich.de/zb
Umschlaggestaltung:	Grafische Medien, Forschungszentrum Jülich GmbH
Druck:	Grafische Medien, Forschungszentrum Jülich GmbH
Copyright:	Forschungszentrum Jülich 2026

Schriften des Forschungszentrums Jülich
Reihe Energie & Umwelt / Energy & Environment, Band / Volume 735

D 468 (Diss. Wuppertal, Univ., 2025)

ISSN 1866-1793
ISBN 978-3-95806-996-1 (Print)
ISBN 978-3-95806-997-8 (E-Book)

Vollständig frei verfügbar über das Publikationsportal des Forschungszentrums Jülich (JuSER) unter www.fz-juelich.de/zb/openaccess.

Abstract

The wave-driven Brewer-Dobson circulation plays a crucial role in transporting radiatively active trace gases and aerosols through the stratosphere, which, in turn, impact the Earth's radiation budget. A detailed understanding of this transport, particularly within a changing climate, is therefore critical. This thesis aims to achieve a dynamical separation of the BDC into distinct branches based on their wave driving, examining the circulation's structure in terms of residual circulation and isentropic mixing. The analysis in this work is based on multiple meteorological reanalysis datasets (ERA5, ERA-Interim, MERRA2, JRA55) and data from the Lagrangian chemistry transport model (CLaMS), utilizing the Transformed Eulerian Mean (TEM) framework, the Downward Control Principle, and tracer continuity equation-based transport diagnostics.

The analysis relies on two metrics generated by wave drag: residual circulation is quantified by the outflow (the total mass flow across turn-around latitudes), while isentropic mixing is assessed via the horizontal mixing tendency in the tracer continuity equation (the horizontal component of tracer transport by eddy mixing). The results reveal the existence of distinct circulation regimes: a deep branch mainly driven by planetary waves (wavenumbers 1–3) and a shallow branch primarily driven by smaller-scale waves (wavenumbers > 3). It is shown that the separation level between the shallow and deep branches can be robustly defined as the lowest altitude where outflow or isentropic mixing from planetary waves exceeds that from smaller-scale waves. Based on analysis of both residual circulation and eddy mixing, this separation level is found at approximately 22 km (about 45 hPa pressure, or about 500 K potential temperature), and shows a weak annual cycle with the highest levels during boreal winter. This climatological structure is robust across the various reanalyses. Above this separation level, the variability of residual circulation and isentropic mixing in the deep branch is mainly related to planetary waves. In the shallow branch, smaller-scale waves play a more important role in the variability of the residual circulation and mixing compared to the deep branch. Trends

in the isentropic mixing and outflow over the period 1980–2017 indicate a weakening of the Brewer-Dobson circulation below the separation level and a strengthening at altitudes slightly above it. In climate model inter-comparisons, the strength and wave driving of the BDC are usually compared at fixed pressure levels, where different circulation branches likely dominate stratospheric transport in different models. Past and present model inter-comparisons generally show a large spread regarding the strength of the simulated BDC. Taking into account differences in wave driving between the circulation branches and in the separation level will likely reduce the spread in model inter-comparisons.

Contents

Chapter 1

Introduction

The stratosphere, the second major layer of Earth's atmosphere, holds about 20% of atmospheric mass and is located roughly between 10 and 50 kilometers above the surface (NOAA, 2024). The stratospheric trace gases, such as ozone, water vapor, and other greenhouse gases, impact the radiative balance and drive climate feedbacks. Changes in the stratosphere, whether due to natural phenomena like volcanic eruptions or human-induced factors such as ozone-depleting substances and greenhouse gas emissions, can propagate downward and influence surface weather and climate patterns.

One of the key features of the stratosphere is the presence of a large-scale meridional circulation known as the Brewer-Dobson Circulation (BDC). This circulation is characterized by the slow ascent of air in the tropical stratosphere, poleward transport, and subsequent descent in middle and high latitudes (Holton et al., 1995; Butchart, 2014). The BDC is typically characterized by a single, broad circulation cell in the winter hemisphere within the middle and upper stratosphere, referred to as the deep branch. In contrast, faster and more localized shallow branches are observed in the lower stratosphere of both hemispheres. The BDC plays a central role in shaping the global distributions of stratospheric trace gases, such as ozone and water vapor, and is therefore critical for both climate and atmospheric chemistry. Particularly in the UTLS (Upper Troposphere and Lower Stratosphere) region, small changes in radiatively active species, like water vapor and ozone, can cause substantial radiative effects (e.g. Solomon et al., 2010; Riese et al., 2012) and impacts on atmospheric circulation (Charlesworth et al., 2023). The existence of the BDC was first inferred from ozone and water vapor observations by Gordon Dobson (Dobson et al., 1929; Dobson, 1956) and Alan Brewer (Brewer, 1949), whose work is described in more detail in Chapter 2.

A mechanistic understanding of the BDC was later developed through the theory of wave–mean flow interaction, particularly by Andrews and McIntyre (1976, 1978a,b,c), who showed how atmospheric waves drive a residual mean circulation through the deposition of momentum in the stratosphere. These waves dissipate throughout the stratosphere, thereby decelerating the predominantly westerly background flow. This mechanism drives poleward mass flow in the subtropical to mid-latitude stratosphere, along with upwelling in the tropics and downwelling at high latitudes. Hence, the global-scale BDC is a wave-driven circulation in the meridional plane. Different waves drive the stratospheric circulation at different levels, including planetary-scale and synoptic-scale Rossby waves as well as small-scale gravity waves (e.g. Plumb, 2002). However, the precise zonal wavenumber that delineates the transition between waves driving the deep and shallow branches remains poorly defined.

From a zonal mean perspective, transport by the BDC can be separated into a residual mean mass circulation and additional, two-way eddy mixing without net mass transport (Garny et al., 2014). Still, the two-way eddy mixing may cause transport of trace gases, due to the strong gradients of these gases in the stratosphere. The residual circulation velocities can be directly related to the wave forcing using the Transformed Eulerian Mean (TEM) framework (Andrews et al., 1987). As found by Haynes et al. (1991), the upward mass flow in the tropics is caused by the wave forcing from all atmospheric levels above ("Downward Control" principle). Hence, variations in tropical upward mass flow across a given level ("tropical upwelling") are expected to correlate with variations in the wave drag above that level.

Birner and Bönisch (2011) found a clear distinction between the deep and shallow circulation branches in terms of transit times along the residual circulation and minimum pressure reached by the air parcels traveling with the residual circulation flow. Based on their trajectory analysis, the shallow circulation branch extends throughout the subtropics and mid-latitudes, vertically up to about 30–50 hPa. Motivated by these results, Lin et al. (2013) defined the shallow circulation branch to extend up to 30 hPa, the deep branch to be located above that level, and an additional transition branch in the lowest stratosphere below 70 hPa. These simplified definitions have the advantage that they equally divide the tropical upward mass flux between the shallow and deep branches, and have been applied for multi-model inter-comparisons of the BDC strength and changes therein (Lin et al., 2013). Furthermore, the shallow and deep stratospheric circulation branches have been argued to be driven by different mechanisms. Gerber (2012) showed from simulations with a mechanistic model that the shallow branch is mainly "tropospherically controlled" by variations of wave sources close to the surface, whereas the deep branch is "stratospherically controlled" by the structure of the stratospheric wave guide.

In a future climate, the stratospheric circulation is expected to accelerate as a response to increasing carbon dioxide levels, and climate models simulate this increase very robustly and throughout the stratosphere (e.g. Butchart, 2014). As the stratospheric residual circulation is too slow to be directly measurable, its strength needs to be inferred indirectly from observations. One commonly used diagnostic for that is stratospheric mean age of air, i.e. the average transit time of air parcels while transported through the stratosphere (Waugh and Hall, 2002). In the lower stratosphere, most recent inter-comparisons of atmospheric reanalyses show decreasing stratospheric mean age of air, indicating that consistently with climate model simulations, a circulation increase over time is also present in observation-based datasets (Garny et al., 2024). It should be noted that these comparisons are not straightforward and that, for instance, the mean age decrease in in-situ observations depends on sampling-correction methods (Ray et al., 2014). At upper levels in the middle stratosphere, there is a remaining discrepancy between stratospheric circulation trends simulated by free-running climate models and observation-based estimates (Garny et al., 2024), which had been already noted for different generations of climate models (e.g. Abalos et al., 2021; Butchart, 2014; Waugh, 2009). At higher altitudes, climate models typically simulate an accelerating circulation, while both in-situ and satellite observations show no evidence of such a trend (Ray et al., 2014; Mahieu et al., 2014; Stiller et al., 2017). However, related observational uncertainties are too large to invalidate model predictions (Garny et al., 2024).

Meteorological reanalyses combine model simulations with observational data by data assimilation, and investigations of the stratospheric circulation in these datasets can give additional insights. In the lower stratosphere, most recent reanalyses show decreasing mean age while in the middle stratosphere mean age trends may differ even in sign between different reanalyses (Chabrillat et al., 2018; Ploeger et al., 2019). Such differences between trends in residual circulation and trends in age of air are likely related to the fact that age of air is not solely controlled by the residual circulation but also strongly affected by mixing processes (Waugh and Hall, 2002). Overall, differences in the vertical structure of stratospheric circulation trends between different datasets raise the question as to whether the dynamical processes driving these changes also differ vertically.

Analysis of the forcing of circulation trends in climate models at a given level shows that particularly the partitioning of the forcing into contributions of different wave types differs substantially between different models (Abalos et al., 2021). These discrepancies in circulation and wave forcing trends might potentially be attributed to variations in the depths of circulation branches across different datasets, such that comparisons at a given level might contrast different dynamical regimes. Hence, an improved interpretation of the stratospheric circulation and its potential changes requires an improved and more detailed understanding of how the different (shallow and deep) circulation branches are separated dynamically.

In this thesis, we investigate the wave forcing of two BDC components (residual circulation and isentropic mixing) and aim to establish a dynamical separation criterion for the different circulation branches. The analysis involves circulation estimates based on the TEM framework and the downward control principle, isentropic mixing of trace gases, as well as separation into contributions from different waves. These diagnostics are applied to various meteorological reanalyses. The specific research questions addressed in this thesis are:

1. Can different shallow and deep branches of the stratospheric circulation be defined in terms of dynamics based on the wave driving classified by spatial scale?

2. Did different branches of the stratospheric circulation change differently over the past decades?

3. How robust is the representation of the circulation structure and its changes in different reanalyses?

4. Does the wave driving-based definition of the branches also hold for isentropic eddy mixing transport?

To address these questions, the contributions of atmospheric waves of different scales to the driving of the overturning circulation have been quantified and compared. A similar approach has been applied when addressing the guiding questions in the context of isentropic mixing.

Following this general introduction, Chapter 2 describes the BDC in more detail and provides historical context for its discovery. The applied circulation diagnostics and considered reanalysis data are described in Chapter 3. Subsequently, in Chapters 4 and 5, the climatological structure, variability, and trends in the stratospheric circulation are investigated. Finally, the results are summarized with respect to the research questions, conclusions are drawn, and an outlook for future research is provided in Chapter 6.

As part of this thesis, a comprehensive Python package was developed to compute residual circulation and transport tendencies, including the separation of wave contributions. The implementation was designed for computational efficiency, allowing application to high-resolution datasets. An overview of this package is presented in Appendix B.

- Some of the main results of this thesis are presented in the following article: Baikhadzhaev R., Ploeger F., Preusse P., Ern M., and Birner T.: A dynamics based separation of deep and shallow stratospheric circulation branches, Atmos. Chem. Phys., accepted for publication, doi: https://doi.org/10.5194/egusphere-2024-4088

- In addition, this thesis contributed to another study: Charlesworth, E., Plöger, F., Birner, T., Baikhadzhaev, R., Abalos, M., Abraham, N. L., Akiyoshi, H., Bekki, S.,

Dennison, F., Jöckel, P., Keeble, J., Kinnison, D., Morgenstern, O., Plummer, D., Rozanov, E., Strode, S., Zeng, G., Egorova, T., and Riese, M.: Stratospheric water vapor affecting atmospheric circulation, Nat. Commun., 14, 3925, doi: https://doi.org/10.1038/s41467-023-39559-2, 2023.

Chapter 2

The Brewer-Dobson circulation

This chapter introduces the stratosphere, providing a brief historical context of its discovery. It examines the apparent contradiction between the observed distribution of trace gases, which suggests substantial vertical and poleward transport, and the combined effects of strong static stability and angular momentum conservation in a rotating system, which inhibit such motion. The chapter also presents the eventual discovery of wave drag as the mechanism that balances angular momentum. Key stratospheric chemical species and their roles in climate processes are also discussed. Finally, the concept of the age of air is introduced, along with the influence of overturning circulation and isentropic mixing on its distribution.

2.1 A short journey through history

Through sensory observations of weather in mountain regions, it has long been known that temperature decreases with altitude (Aristotle and Lee, 1952). However, these surface-based observations alone provided no indication that this trend might reverse at some higher level. As a result, the existence of a distinct atmospheric layer above the troposphere, where temperature increases with height, was not anticipated. The stratosphere was discovered only after the development of balloon-borne measurements capable of reaching the tropopause and beyond in 1902. Independent measurements by Richard Assmann and Léon Teisserenc de Bort at the beginning of the 20th century revealed a layer in the atmosphere where temperature ceased decreasing and began to rise with height, marking the transition from the troposphere to the stratosphere (Assmann, 1902; de Bort, 1902).

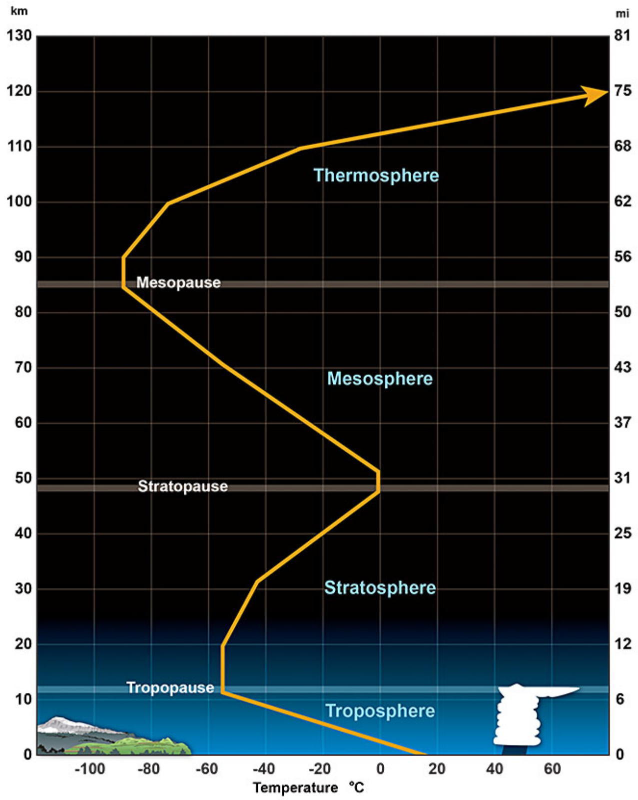

Figure 2.1: Mean temperature profile of the Earth's atmosphere. Figure courtesy (NOAA, 2024)

The stratosphere, which extends from approximately 10–16 km to 50 km altitude, is a distinct atmospheric layer lying above the troposphere (see Fig. 2.1). It is characterized by a temperature inversion due to absorption of ultraviolet radiation by ozone, resulting in a temperature increase with altitude. This inversion leads to a stably stratified environment that essentially prohibits buoyancy-driven convection (Andrews et al., 1987). The conservation of angular momentum imposes a fundamental constraint on large-scale atmospheric motions. Any meridional motion must be accompanied by changes in the zonal wind to conserve angular momentum. However, in the stably stratified stratosphere, such wind adjustments are dynamically suppressed. Consequently, persistent meridional and vertical motion is strongly inhibited in the absence of external forcing (Haynes et al., 1991).

Due to the combined effects of strong static stability and the conservation of angular momentum in a rotating system, the stratosphere was thought to be largely devoid of mean meridional transport; for a time, it was generally regarded as a near-perfect reservoir or “storage layer,” where tracers and constituents could remain for extended periods. Yet, in the mid 20th century, it was observed that ozone concentrations were significantly higher in the extratropical stratosphere than in the tropics, despite the fact that most ozone is produced photo-chemically in the tropical stratosphere. This counter-intuitive distribution pointed to a large-scale poleward transport mechanism. The explanation emerged from the work of Alan Brewer (Brewer, 1949) and Gordon Dobson (Dobson, 1956), who proposed a persistent meridional circulation within the stratosphere. Brewer hypothesized the existence of a slow, large-scale circulation in the stratosphere, characterized by upwelling in the tropical lower stratosphere, poleward transport, and subsequent descent in the extratropics. However, he also acknowledged a major unresolved issue: such a circulation would imply substantial angular momentum transport, which could not be readily explained by the known mechanisms at the time. Dobson provided additional observational support for this circulation, including evidence from balloon soundings and ozone measurements.

The problems concerning the apparent violation of angular momentum conservation were eventually resolved in the mid-1970s by Andrews and McIntyre (1976, 1978a,b,c). By introducing the so-called TEM (see Sect. 3.3) formulation, the angular momentum budget was found to be balanced by wave drag. Hence, the BDC is primarily driven by the interaction between atmospheric waves and the mean flow. These waves propagate upward from the troposphere and deposit momentum in the stratosphere, inducing a residual circulation. Thus, while fundamental dynamical constraints suppress vertical and meridional motion in the stratosphere, wave–mean flow interactions provide the necessary momentum sources to drive the observed circulation patterns. These processes are central to understanding transport and variability in the stratosphere.

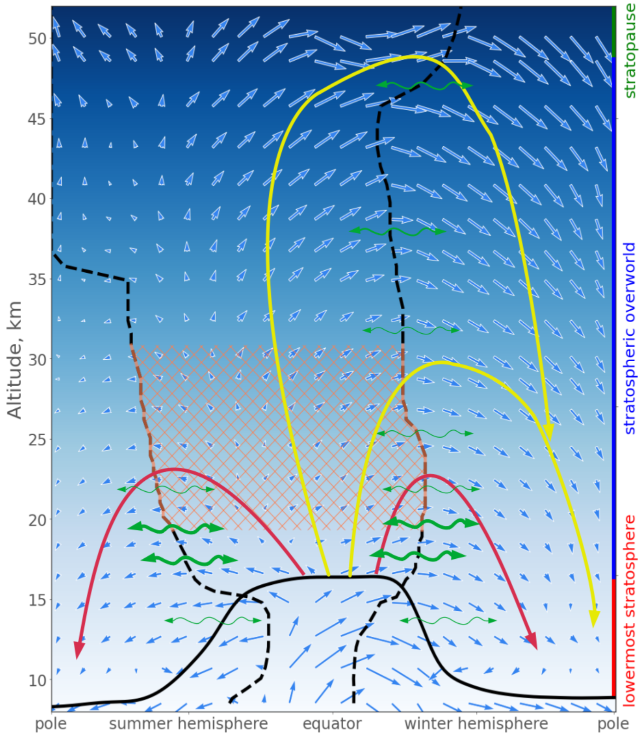

Figure 2.2: Schematic of the BDC. Yellow arrows illustrate the deep branch, red arrows indicate the shallow branches, and green arrows represent isentropic mixing. The solid black line marks the tropopause, while the dashed black lines denote the turn-around latitudes, the area with coral cross-hatching represents the tropical pipe. Blue arrows overlaid with white contours show the residual circulation as estimated from ERA5 reanalysis data.

The BDC comprises a residual circulation with shallow branches, which are most active in the lower stratosphere, a deep branch extending into the middle and upper stratosphere, and additional two-way isentropic mixing (see Fig. 2.2). This circulation governs the meridional distribution of trace gases. As these gases interact with radiation and hence influence the global radiation budget, the BDC may influence the climate system on seasonal to decadal time scales (e.g. Baldwin and Dunkerton, 2001).

2.2 Chemical composition and transport

The stratosphere, bounded below by the tropopause, plays a critical role in the chemical and radiative balance of the atmosphere. The trace gas composition of the stratosphere exerts a disproportionately large influence on the Earth's radiative balance, stratospheric thermal structure, and may also influence surface climate (Solomon et al., 2010; Riese et al., 2012). Among the most important of these are ozone (O_3), water vapor (H_2O), and anthropogenic halogenated compounds.

Ozone and water vapor are the strongest radiatively active species in the stratosphere. The amount of ozone is primarily maintained in the stratosphere through the Chapman cycle. The cycle begins with the absorption of high-energy ultraviolet (UV) radiation by molecular oxygen (O_2), which splits into individual oxygen atoms. These atoms can then react with other O_2 molecules to form ozone (O_3), creating the so-called ozone layer that peaks at approximately 25 to 30 km. Ozone itself absorbs UV radiation, leading to its dissociation back into O_2 and a single oxygen atom. Additionally, ozone can be destroyed when it reacts with a free oxygen atom, resulting in the formation of two O_2 molecules. This cycle establishes a dynamic equilibrium that regulates the concentration of ozone in the stratosphere. The cycle is further modified by catalytic loss cycles involving NO_x, HO_x, ClO_x and BrO_x radicals (Chapman, 1930; Crutzen, 1970; Molina and Rowland, 1974; Solomon, 1999).

Ozone's primary radiative role stems from its strong absorption of harmful solar UV radiation (wavelengths $<\sim 310$ nm), protecting biological systems at the surface. The absorption of UV radiation through photo-chemical reactions heats the stratosphere, creating the characteristic temperature inversion that defines the stratosphere and suppresses vertical convection. This heating plays a key role in maintaining the thermal structure of the stratosphere and strongly influences stratospheric dynamics (Brasseur and Solomon, 2005). In addition, O_3 functions as a significant greenhouse gas through its absorption and emission of terrestrial longwave radiation, primarily centered around $9.6\,\mu\mathrm{m}$. Therefore, ozone depletion, driven primarily by anthropogenic halogens, leads to increased UV transmission to the surface, but, critically, also causes a significant cooling of the lower stratosphere (Ramaswamy et al., 2001). This cooling has, in turn, been shown to affect the strength and persistence of the polar vortex and to induce shifts in tropospheric circulation patterns and surface climate, particularly in the Southern Hemisphere (Polvani et al., 2011). Conversely, the recovery of the ozone layer due to the Montreal Protocol is expected to moderate this stratospheric cooling, with consequent, but complex, impacts on circulation and surface climate trends, potentially reducing some impacts driven by increasing greenhouse gases (WMO, 2022).

Although water vapor concentrations in the stratosphere are relatively low (typically 3–6 ppmv), it remains a significant greenhouse gas and a source of hydroxyl radicals (OH), which are important for the oxidative capacity of the atmosphere. As tropospheric air enters the stratosphere through the tropical tropopause, the amount of water vapor that reaches the stratosphere is primarily regulated by the cold temperatures at the tropical tropopause, a phenomenon known as the ‘cold trap’. Small variations in these temperatures can result in significant variability in stratospheric water vapor. A secondary, in-situ, source is the oxidation of methane within the stratosphere (LeTexier et al., 1988). Increases in stratospheric water vapor, whether driven by changes in tropical tropopause temperatures, changes in the BDC, or increasing methane concentrations, exert a positive radiative forcing, contributing to surface warming, and also contribute to radiative cooling of the stratosphere itself (Forster and Shine, 1999). Furthermore, water vapor plays a role in heterogeneous chemistry on polar stratospheric clouds, contributing to ozone depletion processes. Changes in water vapor concentrations in the lowermost stratosphere (LMS) are particularly critical due to their disproportionate impact on the radiative budget and, consequently, on surface climate. Water vapor in the LMS is affected by additional key processes such as convective overshoots and isentropic mixing across the tropopause, and therefore is more complex and less well understood. Numerical diffusion in Eulerian models leads most current climate models to show a significant positive moist bias in the LMS. The sensitivity of stratospheric and tropospheric circulation to the moist bias in the LMS has been shown by Charlesworth et al. (2023).

Halogenated substances of anthropogenic origin (e.g., CFCs, Halons, CCl_4, HCFCs), once widely used as refrigerants and propellants, are chemically inert in the troposphere but undergo photolytic breakdown in the stratosphere. These species are the primary ozone-depleting substances (ODSs). Upon dissociation, they release chlorine and bromine atoms, initiating highly efficient catalytic cycles that destroy ozone through well-known reaction cycles (Molina and Rowland, 1974). The resulting depletion of ozone leads to changes in radiative heating rates and has been linked to observed trends in stratospheric temperature, particularly in the polar lower stratosphere. The Montreal Protocol (1987) and its amendments have led to a reduction in atmospheric concentrations of many ozone-depleting substances (ODSs) (Newman et al., 2009; Morgenstern et al., 2008), and signs of stratospheric ozone recovery have been observed (WMO, 2022).

The halogenated compounds are extremely potent, long-lived greenhouse gases. Many halogenated compounds absorb strongly in the $8–12\,\mu\mathrm{m}$ atmospheric "window" region of the electromagnetic spectrum, where IR radiation would otherwise escape efficiently to space. Per-molecule, their global warming potential can be many times greater than that of carbon dioxide (Masson-Delmotte et al., 2021). The radiative forcing from halogenated species contributes directly to surface warming. The Montreal Protocol and its amendments, while designed to protect the ozone layer, have therefore also had the significant co-benefit of mitigating a substantial fraction of potential greenhouse-gas-induced warming (Velders et al., 2007).

In summary, the chemical composition of the stratosphere is an important factor in the climate system. Ozone, water vapor, and halogenated species directly modulate the fluxes of shortwave and longwave radiation, influencing temperatures in both the stratosphere and troposphere. In addition, the resulting radiative changes in the stratosphere also feed back on stratospheric dynamics, influencing the BDC, subtropical jets, and the polar vortices. These effects include establishing chemical-radiative-dynamical feedbacks that have demonstrable impacts on tropospheric circulation and surface climate (Baldwin and Dunkerton, 2001; Charlesworth et al., 2023). Understanding the transport of different trace gas constituents by the BDC through the stratosphere is therefore essential for understanding past and current climate as well as projecting future trends. The mathematical description of trace gas transport in the TEM framework is described in Sect. 5.1.

2.3 Age of air

The BDC is characterized by very slow velocities, with tropical upwelling typically on the order of millimeters per second, and thus cannot be measured directly using standard observational techniques. Because of this, the mean age of air (AoA, Γ) is commonly used as a diagnostic tool to infer the cumulative effects of stratospheric transport. AoA represents the mean transit time of an air parcel since entering the stratosphere. Hence, for a conservative tracer χ, whose mixing ratio at the tropopause increases with a constant growth rate c, the mean age Γ at location x and time t is the calculated time lag between the measurement of its current mixing ratio and the moment when that same mixing ratio was recorded at the tropopause (Garny et al., 2024; Waugh and Hall, 2002).

$$\chi(x,t) = c(t - \Gamma(x,t)). \tag{2.1}$$

The individual contributions of residual circulation and isentropic mixing to the mean age of air can be separated (e.g. Ploeger et al., 2015).

$$\overline{\Gamma}(x,t) = \tau_{\mathrm{RCTT}}(x,t) + \int_{t_0}^{t} \mu(x,t')dt', \tag{2.2}$$

where τ_{RCTT} denotes the residual circulation transit time corresponding to transport from the tropical tropopause, which is assumed to be crossed at time t_0, and μ represents the mixing tendency of the mean age integrated along the residual circulation. The mixing tendency μ is described in more detail in Sect. 5.1. The first term on the right-hand side of Eq. 2.2 reflects the effect of the residual circulation on the mean age, while the second term accounts for the additional contribution from mixing, termed "aging by mixing" (Garny et al., 2014).

AoA is typically derived from either atmospheric models or observations of long-lived trace gases with well-characterized surface trends, such as sulfur hexafluoride, CFCs, or carbon dioxide (Hall and Plumb, 1994). The time lag between observed stratospheric concentrations of these species and the corresponding tropospheric concentrations acts as a time marker, allowing the backward inference of how long air has resided in the stratosphere. AoA serves as a comprehensive diagnostic of the integrated transport within the stratosphere and is widely used to assess the performance of chemical transport models and climate simulations (Butchart, 2014). Unlike local wind or tracer diagnostics, AoA encapsulates the combined influence of both advective and mixing processes over the air parcel's history. It is a critical quantity for understanding the distribution and transport of trace gases. Moreover, it is commonly used to study the response of stratospheric transport to climate change, as well as to identify and evaluate trends and variability in the BDC over decadal timescales (Linz et al., 2017). Age of air is also useful in diagnosing the exchange between stratosphere and troposphere, helping to characterize transport barriers and mixing regions.

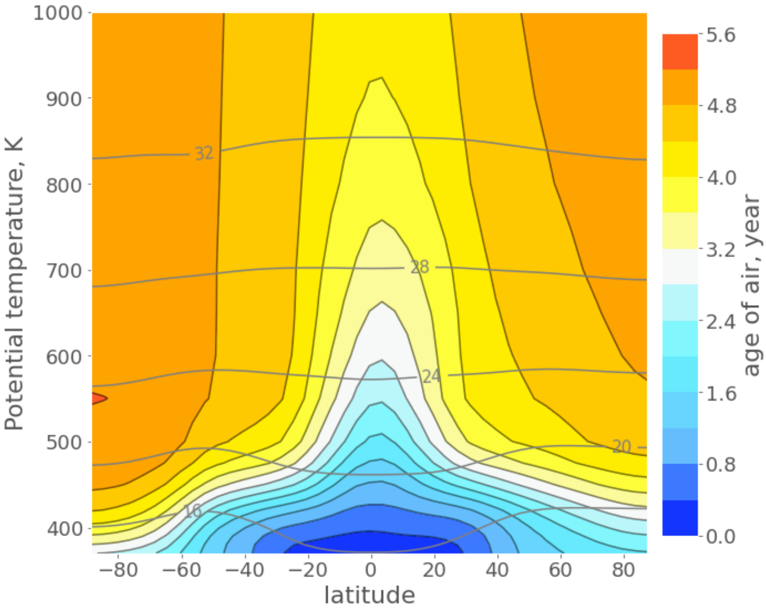

Figure 2.3: Mean age of air estimated using an idealized tracer and CLaMS with winds from ERA5 data for 1980–2017. Altitude levels are shown as gray lines.

The structure of the age-of-air distribution reflects the dominant features of the BDC. Air tends to be youngest in the tropical lower stratosphere, where it enters via slow ascent. It becomes progressively older with altitude and latitude due to poleward transport and longer residence times (Birner and Bönisch, 2011). However, age of air is not solely determined by the residual mean circulation; it is also shaped by two-way mixing processes (Ploeger et al., 2015; Garny et al., 2014). These mixing processes modify the gradients in the age distribution, making it challenging to interpret age-of-air distributions solely in terms of the mean flow. The observed and modeled distributions of age of air provide critical constraints on the net effects of both advective and mixing processes in the stratosphere. The choice of atmospheric model and reanalysis has a notable impact on the climatological mean age-of-air estimates (Ploeger et al., 2019, 2021; Fujiwara et al., 2022). Therefore, in this work, datasets from four reanalyses are utilized, and the comparison of the reanalyses provides valuable insight into the robustness of the results.

Chapter 3

Data and methods

This chapter provides a comprehensive overview of the analytical tools and models employed in this study. It begins by introducing four major atmospheric reanalysis products: ERA5, ERA-Interim, JRA55, and MERRA2, with a discussion of their respective resolutions. Following this, the advantages of Lagrangian chemical climate models are outlined, including a brief introduction to the specific model used in this research, CLaMS.

The theoretical framework for analyzing atmospheric dynamics is then established through the presentation of the TEM formalism and the components of the residual circulation. A key element of this framework, the divergence of the Eliassen–Palm (EP) flux, is introduced as the driving force in the zonal momentum balance. To understand the contribution of different wave scales, the EP flux is decomposed by wavenumber using Fourier analysis of the eddy components of relevant meteorological fields. This allows for the computation of covariances as functions of wavenumber, ultimately enabling the derivation of a wave-resolved EP flux. Finally, the chapter discusses the Downward Control Principle (DWCP), which establishes the crucial link between wave dissipation, represented by EP flux divergence, and the residual circulation. In this context, the Charney–Drazin filtering criterion is also presented to explain how it helps identify which waves can propagate deeper into the stratosphere.

3.1 Reanalyses

Atmospheric reanalysis is a method of reconstructing past atmospheric conditions by assimilating historical observational data into a consistent numerical weather prediction (NWP) model framework. It provides a comprehensive, gridded dataset of atmospheric variables over extended time periods. Reanalysis emerged in the 1990s as a response to the need for long-term, homogeneous datasets for climate research and model validation. Before reanalyses, inconsistencies in weather models and changing observational networks over time limited the usability of historical weather data for climate studies.

Hence, reanalyses provide the most complete data on past climate. The NWP model, its version, set of incorporated observations, and data assimilation methods depend on the producer of the reanalysis and the version of the analysis. In this work, we use data from four global reanalyses: the Modern-Era Retrospective analysis for Research and Applications, Version 2 (MERRA2) from the National Aeronautics and Space Administration (NASA) (Gelaro et al., 2017), the Japanese 55-year Reanalysis (JRA55) from the Japan Meteorological Agency (JMA) (Kobayashi et al., 2015), the ERA-Interim (Dee et al., 2011) and ERA5 (Hersbach et al., 2020) reanalyses from the European Centre for Medium-Range Weather Forecasts (ECMWF). ERA5 (European Centre for Medium-Range Weather Forecasts Reanalysis v5) is the fifth-generation ECMWF atmospheric reanalysis, covering the period from 1940 to the present. The reanalysis has 137 vertical levels extending from the surface to 0.01 hPa. In ERA5, the stratosphere is represented by approximately 45 levels. In all four reanalyses, vertical resolution gets gradually coarser with altitude; in ERA5, the resolution is about 350 m in the lowermost stratosphere and 1500 m in the uppermost stratosphere. The ERA5 high-resolution data are produced as spectral coefficients with a triangular truncation of T639, which roughly corresponds to a horizontal resolution of 0.28°; the data are available at hourly intervals.

ERA-Interim (Interim European Centre for Medium-Range Weather Forecasts Reanalysis) is a predecessor of ERA5; it was discontinued in 2019 and covers the period from January 1, 1979, to August 31, 2019. ERA-Interim has 60 vertical levels spanning from the surface to 0.1 hPa. Approximately 20 of these levels are in the stratosphere, with a vertical resolution of about 1000 m in the lowest part of the stratosphere and roughly 3000 m at the top of the stratosphere. The spectral resolution of the reanalysis is T255, corresponding to a horizontal resolution of approximately 0.70°; the data are available at 6-hour intervals.

JRA55 data are available from 1958 and were discontinued at the end of January 2024. The topmost level of JRA55 is 0.1 hPa; it also has 60 vertical levels, about 20 of which are in the stratosphere. Vertical resolution in the stratosphere is similar to ERA-Interim. With a spectral resolution of T319, the horizontal resolution of JRA55 is approximately twice as coarse as ERA5, at about 0.56°; the temporal resolution of the archived data is 6 hours.

The MERRA2 reanalysis covers the period from 1980 to the present. It has 72 levels spanning from the surface to 0.01 hPa, about 25 of which are in the stratosphere. The vertical resolution in the lowermost stratosphere is close to 1000 m and about 2000 m at the top of the stratosphere. The native horizontal resolution of MERRA2 is 0.5° latitude × 0.625° longitude. Three-dimensional products are available at 3-hourly intervals.

The main focus is on ERA5, which is the most recent reanalysis among these four. The enhanced horizontal and vertical resolution of ERA5 compared to the other reanalyses is expected to result in an improved ability to resolve smaller-scale waves (Watanabe et al., 2015; Müller et al., 2018). The other reanalyses are used primarily for comparison and to assess the robustness of the results.

To retain consistency of spatial and temporal resolution in the inter-comparison, all reanalyses used were resampled on a 1°× 1° latitude-longitude grid, interpolated vertically to the same 88 pressure levels, and resampled in time to 6 hours (00, 06, 12, 18 UTC). The comparison between different reanalyses has been performed over the common 38-year period from 1980–2017. The effect of resampling on ERA5 data is further explored in Sect. 4.3.

The pattern of the residual circulation in the stratosphere is shown in Fig. 4.1 based on ERA5 reanalysis (purple arrows in left panel). The figure shows evidence for the two main branches of the overturning circulation: the deep branch transfers mass from the tropical tropopause to the middle and upper stratosphere and towards the winter pole, while the shallow branch, acting in the lower part of the stratosphere, creates poleward mass flux in both hemispheres.

3.2 Lagrangian chemistry transport model CLaMS

Lagrangian chemistry-climate models represent a class of atmospheric models that simulate the chemical and dynamical evolution of trace gases by following air parcels along their trajectories, rather than solving equations on a fixed grid as in Eulerian models. This approach offers several distinct advantages, particularly in regions where the transport of tracers is highly anisotropic or where fine-scale structures play an important role, such as in the stratosphere. Lagrangian models naturally conserve mass and tracer integrity along trajectories, making them especially effective at capturing filamentary structures, steep gradients, and mixing barriers. These models are also well-suited for diagnosing transport processes, including irreversible mixing and age-of-air diagnostics, as they allow for precise tracking of individual air parcel histories. Furthermore, Lagrangian frameworks can minimize numerical diffusion, which is a common issue in Eulerian models and can lead to unrealistic smoothing of tracer distributions, leading to overestimation of tracer transport through transport barriers.

The Chemical Lagrangian Model of the Stratosphere (CLaMS) combines a trajectory-based transport scheme with a detailed chemical module to simulate the evolution of stratospheric trace gases under realistic meteorological conditions. The model uses a hybrid approach that incorporates isentropic advection driven by reanalysis winds, combined with parameterized cross-isentropic (diabatic) motion and a physically based representation of mixing processes. One of CLaMS's key innovations is its treatment of mixing as a diffusive process that is only activated under strong flow deformation, allowing for more realistic simulation of transport barriers and mixing efficiency. This makes CLaMS especially powerful in studying phenomena such as the polar vortex, stratospheric intrusions, and the distribution of long-lived tracers like ozone and nitrous oxide (Konopka et al., 2004). In this study, CLaMS is used to estimate the AoA and N_2O distribution, and to evaluate isentropic mixing associated with different waves in the regions corresponding to the shallow and deep branches of the BDC.

3.3 Overturning circulation diagnosis

In the stratosphere, the zonal mean flow is strongly influenced by wave-mean flow interactions, and conventional zonal-mean diagnostics can obscure the true nature of mass and momentum transport because of the presence of eddies and wave-induced motions. The TEM formalism addresses this by incorporating the effects of eddies into a residual circulation, which more accurately represents the net mass transport. This makes the TEM approach particularly useful for studying the BDC, as it enables the quantification of wave forcing via the EP flux divergence and the corresponding mean meridional and vertical motions. The analyses in this thesis are based on the TEM framework (Andrews et al., 1987) utilizing the two independent estimates to diagnose and investigate the overturning circulation: (1) the "direct" residual circulation definition $\bar{v}^*, \bar{w}^*$ and (2) an "indirect" momentum balance-based estimate of the residual circulation $\bar{v}^*_D, \bar{w}^*_D$, where the upwelling velocity is calculated from the wave drag based on the DWCP (e.g. Haynes et al., 1991). Although both approaches are based on the TEM framework, the direct estimate of the residual circulation will be referred as the "TEM" approach from here on and the indirect momentum balance estimate as the "DWCP" approach, in the following. On the one hand, the direct TEM approach is conceptually simpler and more frequently used in studies of the stratospheric circulation. On the other hand, the DWCP approach allows to relate the residual circulation to the wave drag and in particular to estimate the relative contributions of individual waves to the driving of the residual circulation. Uncertainties and limitations such as those arising from numerical approximations, data assimilation procedures, and the lack of strict mass conservation in reanalyses affect both estimates in distinct ways. Therefore, their comparison provides valuable insight into the robustness of our results.

Equations in this section use log-pressure altitude as vertical coordinate; it is defined as in (Andrews et al., 1987)

$$z = -H\ ln(p/p_s) \tag{3.1}$$

where p_s is a surface pressure (here, taken as 1000 hPa), and H is a mean scale height (here taken as 7 km). From here on, throughout the text and in all figures, the term 'altitude' refers to log-pressure altitude, unless specified otherwise.

The vertical and horizontal components of the TEM residual circulation in log-pressure coordinates are therefore defined through

$$\begin{aligned} \bar{v}^* &= \bar{v} - \rho_0^{-1}(\rho_0 \overline{v'\theta'}/\bar{\theta}_z)_z \\ \bar{w}^* &= \bar{w} + (a\ \cos(\phi))^{-1}(\cos(\phi)\, \overline{v'\theta'}/\bar{\theta}_z)_\phi \end{aligned} \tag{3.2}$$

where an overbar indicates the zonal mean, a prime the deviation from the mean, subscripts denote partial derivatives, v is meridional velocity, ρ_0 is basic density, θ is potential temperature, w is vertical velocity, and a is the mean radius of the Earth.

Energy deposition from wave dissipation constitutes the driving force of the residual circulation. The wave dissipation results in eddy potential vorticity fluxes, which, in turn, are approximately equal to the EP flux (Andrews et al., 1987). The latitudinal and vertical components of the EP flux are defined by

$$\begin{aligned} F^{(\phi)} &= \rho_0 a\ \cos(\phi)\,(\bar{u}_z \overline{v'\theta'}/\bar{\theta}_z - \overline{v'u'}) \\ F^{(z)} &= \rho_0 a\ \cos(\phi)\{[f - (a\ \cos(\phi))^{-1}(\bar{u}\ \cos(\phi))_\phi]\overline{v'\theta'}/\bar{\theta}_z - \overline{w'u'}\} \end{aligned} \tag{3.3}$$

where u is zonal wind velocity, f is the Coriolis parameter defined as $2\Omega\ \sin(\phi)$, where Ω is the angular velocity of the Earth.

The divergence of the EP flux ($\nabla \cdot F$) represents the driving force in the zonal momentum balance equation

$$\frac{\partial \bar{u}}{\partial t} + \bar{v}^*(\frac{1}{a\ \cos(\phi)}\frac{\partial \bar{u}\ \cos(\phi)}{\partial \phi} - f) + \bar{w}^*\frac{\partial \bar{u}}{\partial z} = \frac{\nabla \cdot F}{\rho_0 a \cos\phi} + \bar{X}\ . \tag{3.4}$$

Here, X includes contributions from parameterized waves and will not be further considered in this thesis, which focuses on the contribution from resolved waves.

The contributions of individual waves to the EP flux can be estimated by Fourier transformation of the three-dimensional EP flux data from longitude to wavenumber-frequency domain. The thus transformed components of the EP flux are defined as

$$F^{(\phi)}(s) = \rho_0 a\, \cos(\phi)\mathrm{Re}[\bar{u}_z \hat{v}(s)\hat{\theta}^*(s)/\bar{\theta}_z - \hat{u}(s)\hat{v}^*(s)]/(n_s^2/2)$$
$$F^{(z)}(s) = \rho_0 a\, \cos(\phi)\mathrm{Re}\{[f - (a\, \cos(\phi))^{-1}(\bar{u}\, \cos(\phi))_\phi]\hat{v}(s)\hat{\theta}^*(s)/\bar{\theta}_z - \hat{u}(s)\hat{w}^*(s)\}/(n_s^2/2) \tag{3.5}$$

where Re denotes the real part of a complex number, asterisks denote complex conjugates, hats represent Fourier coefficients, s is the wavenumber index, and n_s is the sample size (number of longitudinal grid points). To compute these terms, a Fast Fourier Transform (FFT) was applied to each fluctuation component, excluding the negative frequencies. This FFT results in a N/2 long set of individual wave contributions to the EP flux. Summation over all wave components in $F(s)$ from Eq. 3.5 yields values that are almost identical to those of F in Eq. 3.3, such that numerical uncertainties in the calculation are negligible.

Here, wavenumber represents the spatial scale of the wave, the number of waves per 360 degrees of longitude, with wavenumber 1 (hereafter referred to as wave 1) being the largest possible zonal wavelength. In this work, the reanalysis data has been resampled to a 1 by 1 degree horizontal grid. The Nyquist-Shannon sampling theorem (Nyquist, 1928; Shannon, 1949) requires at least two data points per wavenumber to detect the wavenumber. Therefore we truncate the wave separation at wave 180, noting that even for this wavenumber the contribution could be underestimated (e.g. Abdalla et al., 2013; Skamarock, 2004). The effect of resampling ERA5 from 0.3°to 1°horizontal resolution on the contribution of smaller-scale waves is discussed in more detail in Sect. 4.3.

The wave dissipation given by $\nabla \cdot F$ and the residual circulation are connected through the DWCP. The DWCP states that the mass flow across a given level is related to the momentum deposition from dissipating waves above that level. We use this relation to estimate the relative contributions of different waves to the driving of the residual circulation. Based on the DWCP, the following expressions can be derived for the residual mass stream function $\bar{\psi}^*_D$ and for the components of the residual circulation $\bar{v}^*_D, \bar{w}^*_D$

$$\bar{\psi}^*_D = \int_z^\infty \frac{a\,\cos(\phi)\nabla\cdot F}{\left[a\,\cos(\phi)(\bar{u}+a\,\cos(\phi)\,\Omega)\right]_\phi}dz \tag{3.6a}$$

$$\bar{v}^*_D = \frac{1}{\rho_0\,\cos(\phi)}\frac{\partial\bar{\psi}^*_D}{\partial z} \tag{3.6b}$$

$$\bar{w}^*_D = \frac{1}{a\rho_0\,\cos(\phi)}\frac{\partial\bar{\psi}^*_D}{\partial\phi} \tag{3.6c}$$

Strictly speaking, the integration in Eq. 3.6a should be performed along isolines of constant angular momentum. However, since outside the tropics the isolines of constant angular momentum are approximately lines of constant latitude, we perform the integration along constant latitudes (cf. Abalos et al., 2015). Therefore, we estimate the mean residual circulation upwelling between 20°S and 20°N by integration of Eq. 3.6c

$$\bar{w}^{*\pm}_D = \frac{\bar{\psi}^{*-}_D - \bar{\psi}^{*+}_D}{-a\rho_0 S^\pm} \tag{3.7}$$

where the superscript $\pm$ denotes that the quantity is evaluated at the latitudes 20°N and 20°S, respectively. Hence, $S^\pm$ is the normalized area fraction of the latitude band between these latitudes and $\bar{w}^{*\pm}_D$ is the mean DWCP vertical velocity averaged over this region.

The turn-around latitudes (TAL) separate the region of upward residual velocity in the tropical stratosphere from the region of downward velocity in the extratropics (e.g. Abalos et al., 2015). In this work, tropical upwelling is defined as the total mass flow between the TAL carried by $\bar{w}^*$, and tropical outflow is defined as the poleward mass flow across the TAL. The outflow at a given level represents the result of "gyroscopic pumping" (Holton et al., 1995), indicating the amount of air mass being pulled from the tropics to middle and high latitudes by the wave drag at that level. The tropical upwelling, on the other hand, represents the integrated effect of the wave drag at all levels above, as described by the downward control principle (see above). Hence, the total tropical upwelling is given by

$$W = 2\pi a^2\rho_0\int_{\phi_-}^{\phi_+}\bar{w}^*\,\cos(\phi)d\phi\;, \tag{3.8}$$

and the outflow out of the tropics at a given level is the vertical derivative (top to bottom) of the upwelling by

$$V = -\frac{\partial W}{\partial z} \; . \tag{3.9}$$

The two major wave types that drive the overturning circulation are Rossby and gravity waves. Planetary and synoptic-scale Rossby waves are large-scale, and are related to the horizontal gradient of potential vorticity. These waves are influenced by the Earth's rotation, the latitudinal gradient of the Coriolis parameter, and the mean zonal flow. Gravity waves are of smaller scale, less dependent on the Earth's rotation and primarily result from the restoring force due to stable background stratification. The upward propagation of Rossby waves is controlled by the Charney-Drazin condition (Vallis, 2006), which for stationary waves is

$$0 < \bar{u} < \frac{f_\phi}{k^2 + l^2 + (f_0/2NH)^2} \; . \tag{3.10}$$

Here, k and l are zonal and meridional wavenumbers, f_0 is a reference value of the Coriolis parameter, and N is the buoyancy frequency. This condition implies that Rossby waves may propagate upwards into the stratosphere if the zonal flow is eastward and weaker than a critical value. This critical value is higher for larger-scale waves (smaller k, l) such that these waves may propagate deeper into the stratosphere compared to smaller-scale waves.

A common approach in BDC studies is a separation of wave-driving based on the zonal wavenumber of the involved atmospheric waves (e.g. Randel et al., 2008; Kim and Alexander, 2015; Abalos et al., 2024). In this study, the following scale distinction is adopted: waves 1 to 3 are categorized as planetary, waves 4 to 20 as synoptic-scale, and resolved waves with wavenumbers greater than 20 are classified as mesoscale waves. A combination of synoptic- and mesoscale waves will be referred to as smaller-scale waves. Accordingly, planetary waves are Rossby waves, synoptic-scale waves are dominated by Rossby waves with increasing secondary contributions from gravity waves at higher wavenumbers, and mesoscale waves can be interpreted as gravity waves (Strube et al., 2020; Žagar et al., 2018). Furthermore, planetary waves are typically forced by large-scale stationary features of the Earth's surface, such as orography and land-sea contrasts, and therefore at the altitude range of interest are expected to be stationary or quasi-stationary (Ghinassi et al., 2022). This interpretation is further supported by the consistency between panel b of Fig. 4.1 and the amplitudes of geopotential height variations associated with zonal wavenumber 1 in Koval et al. (2023). In particular, the slowest normal mode with a 16-day period analyzed by Koval et al. (2023) most closely resembles the structure of the Eliassen–Palm flux shown in panel b.

Chapter 4

A dynamics-based separation of the residual circulation branches

In this chapter, the structure of the stratospheric residual circulation is examined, with particular focus on the occurrence of different circulation branches. The contributions of planetary, synoptic-scale, and resolved mesoscale waves to the driving of the circulation, and the different branches, are evaluated. To determine how different waves influence the circulation at various altitudes, vertical profiles of the wave-induced circulations are constructed using DWCP and analyzed with statistical and mechanistic approaches. The aim of this chapter is to investigate whether the deep and shallow branches of the stratospheric residual circulation are driven by distinct wave regimes, and whether these can be identified consistently across four reanalyses. Another key objective is to define the separation level between the shallow and deep circulation branches. Finally, the chapter analyzes the variability and long-term trends of the components of the residual circulation driven by planetary and smaller-scale waves, as well as the total residual circulation.

4.1 Wave forcing of the Stratospheric residual circulation branches and separation level between them

4.1.1 General structure of the circulation

Figure 4.1 shows the climatology of the residual mean mass circulation for the period 1980–2017 together with the resolved wave drag quantified in terms of $\nabla \cdot F$, which constitutes the circulation's driving force (see Eq. 3.4). Note that $\nabla \cdot F$ has been scaled by $(a\rho_0 \cos\phi)^{-1}$ and 86400 s/day to obtain the wave drag in m s^{-1} day^{-1}. The well-known characteristics of the stratospheric residual circulation, with upwelling in the tropics, poleward motion and downwelling in the extratropics, and a stronger circulation cell in the winter hemisphere, are all evident in Fig. 4.1 (colors represent dissipation or "wave drag" by resolved waves).

The reduced wave drag in the middle and upper stratosphere in the summer hemisphere is related to the presence of westward winds which prohibit Rossby waves from propagating upward, known as the Charney-Drazin criterion (Charney and Drazin, 1961). The wave filtering resulting from this criterion prohibits the propagation of waves through a medium with an eastward wind speed above a certain threshold or any westward wind (see Eq. 3.10). Consequently, as illustrated in the second and third columns of the figure, large-scale Rossby waves are more likely to satisfy the criterion and can generally propagate deeper into the stratosphere. Furthermore, the majority of small-scale Rossby waves with wavenumbers greater than 3 dissipate in the lower part of the stratosphere. Gravity waves remain unaffected by the filtering process, allowing them to propagate deeper into the atmosphere and to drive the mesospheric circulation. The seasonality of the BDC causes seasonal movement of the TAL with significant displacement into the summer hemisphere (Fig. 4.1, dashed black lines).

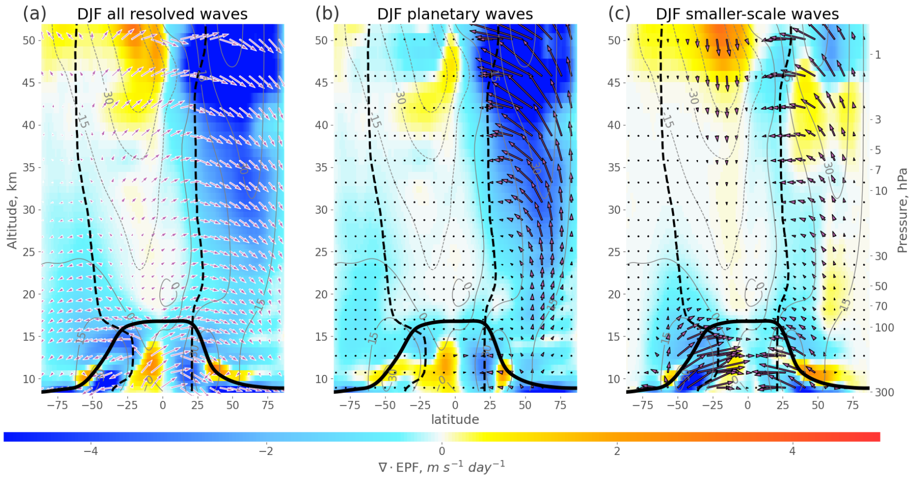

Figure 4.1: Climatological (1980–2017) distributions of resolved wave drag (estimated as $\nabla \cdot F$, color coded) together with Eliassen–Palm flux vectors (black contour arrows in panels b and c), log scaled TEM residual circulation (white contour arrows in panel a), zonal mean zonal wind (grey contours) from ERA5 reanalysis for December–February. The distributions are shown for the contribution from all resolved waves (left), from planetary waves (wavenumbers 1–3, middle) and from smaller-scale waves (wavenumbers greater than 3, right). The black dashed lines show the turn-around latitudes (where upwelling in tropics changes to downwelling in extratropics), the thick black line shows the tropopause.

The primary factor driving the tropical upwelling in the stratosphere is the wave drag near the TAL, which is ultimately responsible for the uplift in the tropics (Eluszkiewicz et al., 2000).

The northern TAL in the lower stratosphere is typically located between 20°and 40°N. Figure 4.2 presents the time series of the wave drag and the horizontal component of the residual circulation, estimated using the TEM approach and DWCP, at 70 hPa within this latitude range. The figure shows a close relation between horizontal velocity $\bar{v}^*$ and wave drag, as expected from Eq. 3.4. Overall, the net outflow velocity calculated using the TEM approach agrees well with the momentum balance estimate of the velocity derived from the drag of all resolved waves. The discrepancy in residual circulation velocity between the TEM approach (green dashed line in Fig. 4.2) and the DWCP (black dashed line) at

70 hPa is at least in part attributable to the fact that the DWCP only accounts for resolved wave drag (see Eq. 3.6a) while the full horizontal velocity based on the TEM definition is also influenced by small-scale parameterized gravity waves. Other potential contributors to the discrepancy include computational approximations and the known limitation that reanalyses do not strictly conserve mass. An effect of parameterized gravity wave drag on upwelling similar to the discrepancy between the approaches has been shown by Butchart et al. (2011). As a result, the DWCP estimate of the residual circulation driven by the drag of all resolved waves is weaker than the one obtained by also taking into account the additional wave drag related to parameterizations, using the TEM approach. This deficit is shown in Fig. A.2 and discussed in more detail in Sect. 4.3.

As might be expected, the wave drag at the considered level $\nabla \cdot F$ (solid lines in Fig. 4.2), and the horizontal component of the residual circulation estimated from the wave drag above using the DWCP $\bar{v}^*_D$ (dashed lines in the figure) are consistent and have similar variability. The wave driving at 70 hPa in Fig. 4.2 shows that about three-quarters of the circulation at that level is driven by smaller-scale waves. However, despite driving only one-quarter of the circulation, the planetary waves influence the variability of the circulation almost as much as the smaller-scale waves. The variability of the circulation velocities and their relation to wave drag is discussed in more detail in Sect. 4.2.1. The wave filtering due to the Charney-Drazin criterion related to the pattern of zonal wind (Fig. 4.1) limits the propagation of smaller-scale Rossby waves into the middle and upper stratosphere. As a result, the smaller-scale waves that do reach the stratosphere are expected to break and deposit their momentum at lower levels. Thus, smaller-scale waves are expected to drive the shallow branch and planetary waves to drive the deep branch of the residual circulation (Plumb, 2002).

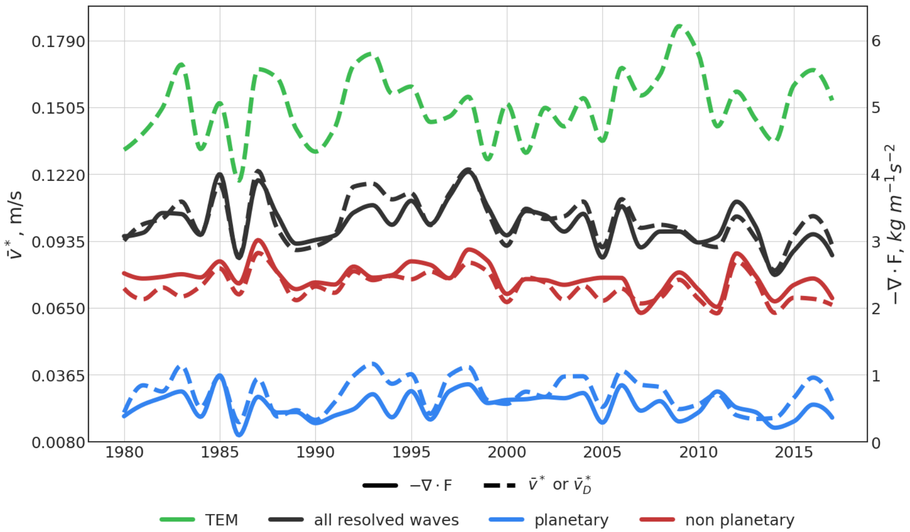

Figure 4.2: Annual mean time series at 70 hPa (mean 20N-40N) of horizontal component of the residual circulation (dashed lines), and EP flux divergence $\nabla \cdot F$ (solid lines). Residual velocity from TEM approach (green), $\nabla \cdot F$ and residual velocities from DWCP for total (black), planetary (blue) and other than planetary (red) waves. The figure is based on 1980–2017 ERA5 data

Analysis of the resolved wave drag demonstrates that the large-scale waves (planetary and synoptic-scale) generate most of the upwelling in the tropical lower stratosphere (Fig. 4.3 (a)). The separation of horizontal outflow into contributions from different waves in Fig. 4.3 (b) further shows that at upper levels planetary waves dominate while at lower levels (below about 22km) synoptic-scale waves dominate. This indicates that the deep branch is mainly driven by planetary wave drag, while the shallow branch is mostly driven by synoptic-scale waves. Furthermore, drag due to mesoscale waves almost exclusively contributes to the shallow branch. This drag induced by the breaking of mesoscale waves is significantly stronger in ERA5 than in the other three reanalyses (not shown).

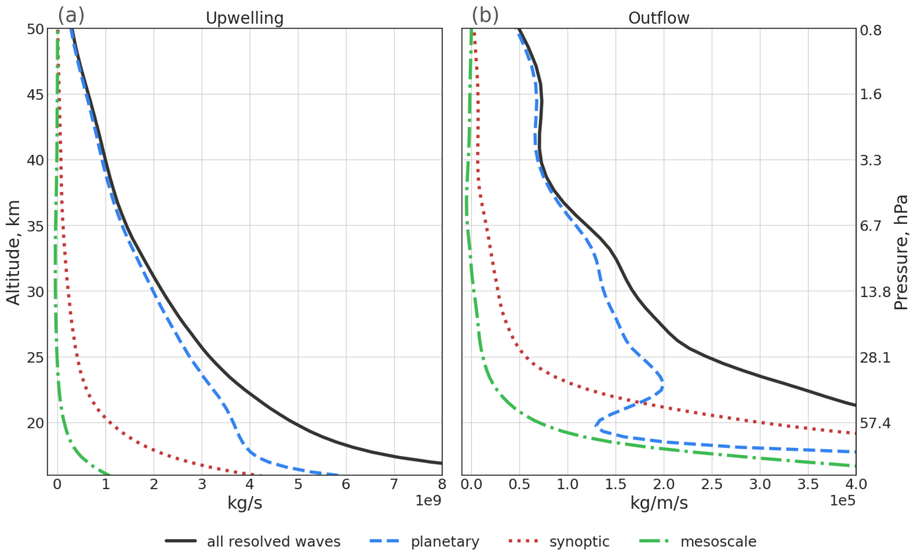

Figure 4.3: (a) Vertical profiles of mean (1980–2017) upwelling estimated with DWCP and driven by all resolved wave drag (black solid line), planetary wave drag (blue dashed line), synoptic-scale wave drag (red dotted line), and mesoscale wave drag (green dash-dotted line). (b) equivalent to (a) with vertical profiles of mean outflow. The figure is based on ERA5 data

4.1.2 Separation of the deep and shallow branches by wave forcing based on climatological data

We conduct a more detailed analysis of the specific wave driving of the deep and shallow circulation branches based on both a mechanistic and a statistical analysis. The mechanistic analysis is based on the DWCP and separates upwelling and outflow velocities into contributions from different waves. Since planetary and synoptic-scale waves account for the majority of the resolved wave drag, the contributions of the individual wavenumbers from 1 to 6 are separated in Fig. 4.4a. The vertical profiles of outflow presented in the figure clearly indicate that waves 1 and 2 drive the deep branch of the circulation at levels above about 22 km. On the other hand, wave 4 and smaller-scale waves dominate the outflow below that level. The role of waves 3 and 4 is somewhat intermediate, with these waves driving a significant portion of the circulation at all levels. The other three reanalyses considered in this study exhibit similar vertical distributions of wave drag for the wavenumbers 1 to 6 (not shown). Regarding the relative outflow in Fig. 4.4b, waves with wavenumbers larger than 3 produce outflow maxima which are well-confined below about 25km, while the outflow due to larger-scale planetary waves maximizes over broad regions above. The vertical location of the maxima of relative outflow indicates that wave 3 plays a more prominent role in driving the deep branch, while wave 4 is more strongly driving the shallow branch. The individual outflow induced by a single wavenumber up to wave 59 can be seen in Fig. A.1, which shows that resolved waves with wavenumbers larger than 6 almost exclusively drive the shallow branch of the stratospheric circulation.

The statistical analysis examines the correlation near the TAL between the outflow velocity and the $\nabla \cdot F$ associated with different wave bands. Here, the outflow velocity is estimated as the horizontal component of the residual circulation from the TEM framework ($\bar{v}^*$) (multiplied with minus sign in the northern hemisphere, such that a positive correlation results for increased poleward flow related to more negative $\nabla \cdot F$ values). The correlation coefficient between the TEM outflow velocity and the $\nabla \cdot F$ derived from the total resolved wave drag, is approximately 0.8 to 0.9 except in regions below 20 km altitude, where the correlation weakens (not shown).

To further investigate whether waves 3 and 4 primarily drive the shallow or deep branch, the correlations of both large-scale wave drag with outflow velocity and that of smaller-scale wave drag with outflow velocity are calculated for the three cases of defining large-scale waves as 1–2, 1–3, and 1–4. Then the difference between the correlations for large-scale waves and for smaller-scale waves are calculated and profiles of these differences are shown in Fig. 4.4c, d. We expect the largest-scale waves to exhibit a stronger positive correlation within the deep branch region, while smaller-scale waves are anticipated to show a stronger positive correlation in the shallow branch region. Hence, the correlation difference profiles should be positive in the deep branch and negative in the shallow branch region, respectively. Including wave 4 into the large-scale waves results in a stronger correlation of the outflow velocity in the shallow branch region of the Southern Hemisphere with the large-scale waves compared to the smaller-scale waves (blue line in Fig. 4.4d). Additionally, incorporating wave 3 into the smaller-scale waves enhances the correlation between outflow velocity and smaller-scale wave drag at certain levels in the middle stratosphere, surpassing the correlation observed for the large-scale waves (red lines in Fig. 4.4c, d).

Taking all these aspects into account, we conclude that the clearest separation between different circulation branches at upper and lower levels in terms of wave drag occurs between waves 3 and 4. Hence, we define the deep circulation branch of the stratospheric BDC to be driven by planetary waves 1–3 and the shallow circulation branch to be driven by smaller-scale waves (wavenumbers larger than 3). The following analyses of BDC structure, variability and trends, support our choice in separating the wave driving into these two classes of waves as separated by scale.

Vertical profiles of upwelling and outflow generated by planetary and smaller-scale waves were constructed for the different reanalyses and are presented in Fig. 4.5. Regardless of the reanalysis, planetary waves generate the majority of the outflow in the middle stratosphere and nearly all of the outflow in the upper stratosphere. Smaller-scale waves, on the other hand, are responsible for most of the outflow in the lower stratosphere. Compared to the other three reanalyses, ERA5 indicates a notably higher total outflow in the lower stratosphere between about 20-25km. This difference is likely related to the effects of small-scale waves and the outflow they generate. Specifically, better spatial and temporal resolution of ERA5 allows for better representation of mesoscale (gravity) waves in ERA5 than in the other reanalyses (e.g. Hoffmann et al., 2019). The drag caused by planetary waves is very similar between all four reanalyses. Hence, ERA5 is able to resolve more mesoscale waves and has a stronger related wave drag than other reanalyses. Consequently, in ERA5 these waves contribute significantly more strongly to the shallow branch.

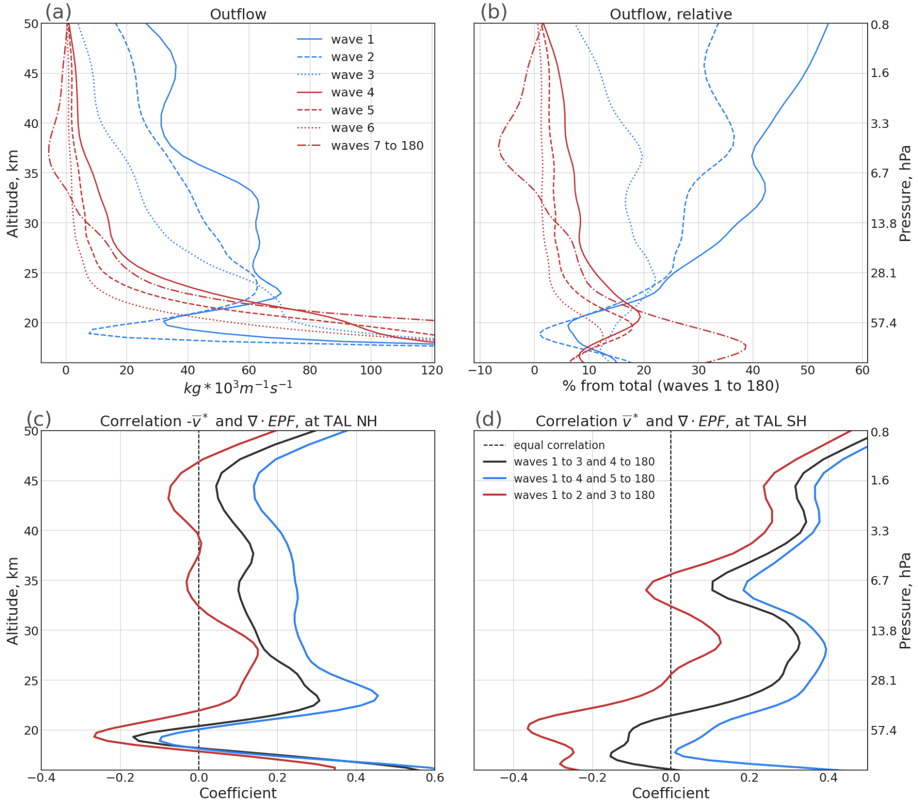

Figure 4.4: (a) Tropical outflow from the area between TAL into the extratropics calculated from Downward Control principle for different waves (colors and line styles). (b) Equivalent to (a) but in relative units as percentage of the total outflow of all resolved waves. (c) Difference between the correlations of outflow velocity from the TEM approach with wave drag generated by large-scale and smaller-scale waves (computed as correlation with large-scale minus correlation with smaller-scale), evaluated at turn-around latitudes in the Northern Hemisphere. Colors represent different wave bands for the large- and smaller-scale wave categories. (d) Same as (c) but for the southern hemisphere. Deseasonalized monthly mean data is used for calculation of the correlations presented in panels (c) and (d). The lines presented in this figure were smoothed with a Gaussian filter for better readability. The figure is constructed from monthly mean ERA5 data for 1980–2017.

Figure 4.5 further shows that the level which separates the two dynamical regimes with outflow mainly generated by planetary waves above and mainly by smaller-scale waves below emerges similarly for the different reanalyses. Therefore, this level represents a natural separation in terms of dynamical characteristics, i.e. wave driving, between the shallow and deep branches of the stratospheric circulation and is largely consistent across the different datasets considered.

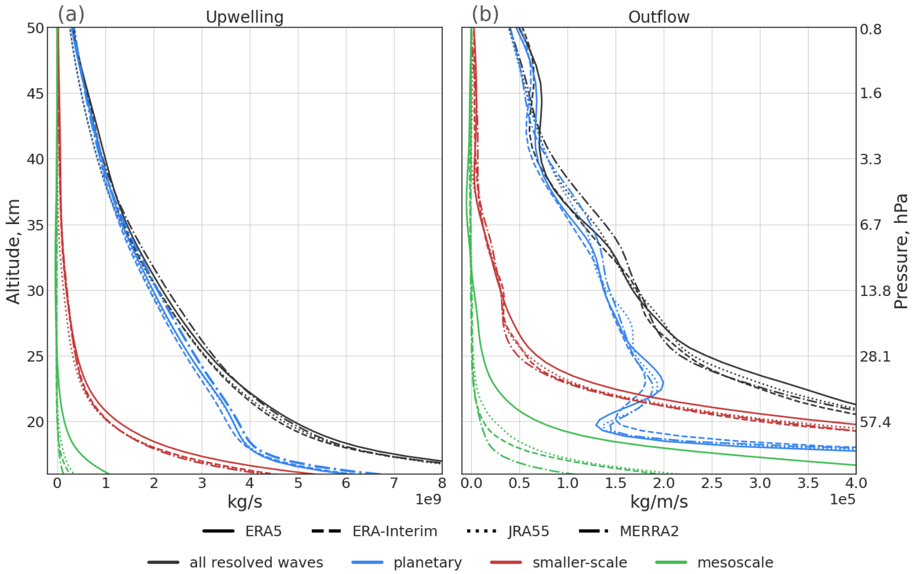

Figure 4.5: (a) Mean profiles of upwelling calculated from DWCP, induced by all resolved waves (black lines), planetary waves (blue lines), smaller-scale waves including mesoscale (red lines), and mesoscale waves (green lines) from ERA5 (solid), ERA-Interim (dashed), JRA55 (dotted), and MERRA2 (dash-dotted) reanalyses for 1980–2017. (b) Corresponding profiles of outflow. The lines presented in this figure were smoothed with a Gaussian filter for better readability.

4.1.3 Level of the separation between shallow and deep branches

The clear difference between the contributions of planetary and smaller-scale waves to the stratospheric residual circulation at upper and lower levels allows the robust definition of a separation level between a deep and shallow circulation branch in terms of wave drag. We define the separation level between the deep and shallow branches as the lowest altitude at which the contribution to outflow from planetary waves is equal to the contribution from smaller-scale waves. To eliminate sharp spikes of outflow in monthly mean data, which can cause unexpected variations in the separation level height, a rolling mean over five vertical levels is applied to the outflow profiles before determining the separation level. In cases where the monthly mean data shows equal contributions to the outflow from planetary and smaller-scale waves at multiple altitudes, we consider the separation level too vague for accurate estimation and exclude these months.

The seasonal variation of the separation level is shown in Fig. 4.6. The separation level shows a weak seasonal cycle with a somewhat lower separation level height in boreal summer months, similarly across all four reanalyses considered. The separation level height depends on the relative contributions of planetary waves and smaller-scale waves to tropical outflow. A stronger contribution from planetary waves raises the separation level, whereas a stronger contribution from smaller-scale waves lowers the separation level (Fig. 4.5 b). Therefore, the seasonal cycle of the separation level is likely linked to the annual cycle of wave drag. In particular, the weaker planetary wave activity during boreal summer is likely important for pushing the separation level downward.

The large variability of the separation level (standard deviation, shown by the whiskers in Fig. 4.6) indicates a large inter-annual variation of the separation level height, which is of similar magnitude as the seasonal variation.

Furthermore, during most months, the separation level is located at higher altitudes for ERA5 compared to other reanalyses (Fig. 4.6). This difference is likely related to the ability of ERA5 to better resolve smaller-scale waves, which shifts the separation level to higher altitudes compared to the other reanalyses. Given its higher resolution and ability to resolve larger parts of the mesoscale wave spectrum, we consider the estimate of the separation level height from ERA5 to be more accurate than those from the other reanalyses.

The focus of this study is on the effects of resolved waves, but we notice that contributions from smaller-scale, unresolved waves could modify our results. Since smaller-scale waves are responsible for driving the shallow branch and since the upwelling deficit increases at lower levels in the shallow branch region (Fig. A.2), it is likely that the parameterized wave drag also contributes significantly to the shallow branch. Therefore, we expect the separation level to be located at somewhat higher altitudes for higher-resolution data with a greater portion of the smaller-scale wave spectrum resolved or with parameterized wave drag included in the analysis.

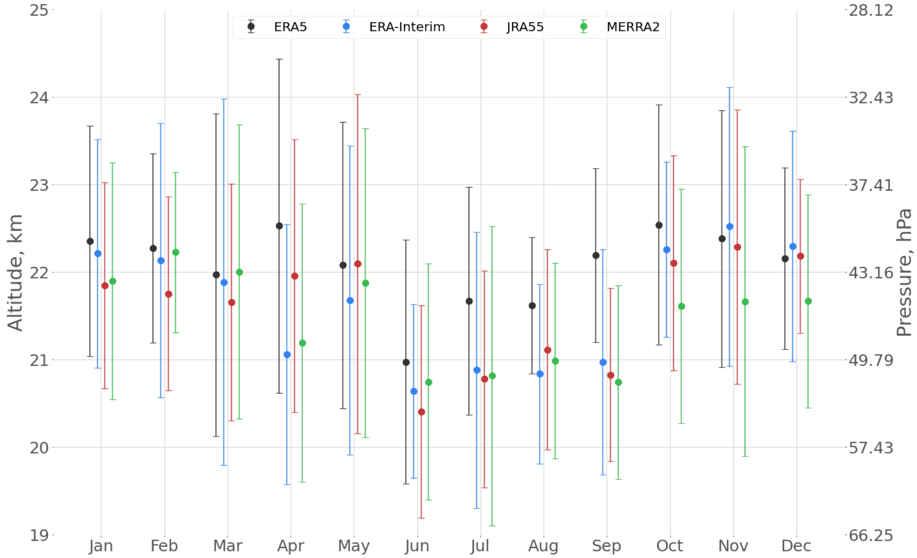

Figure 4.6: Seasonal cycle of the level separating the deep and shallow branches of the stratospheric circulation. Dots show the mean altitude of the level for each month, with the corresponding standard deviation as error bars. The colors represent different reanalyses: ERA5 (black), ERA-Interim (blue), JRA55 (red), and MERRA2 (green). The level is estimated from 1980–2017 monthly mean data.

4.2 Variability and trends in circulation structure

4.2.1 Variability of the circulation

Figure 4.7 shows the upwelling at 100 hPa, which is close to the tropopause, at 43 hPa, which is approximately the separation level between the shallow and deep branches, and the difference between upwelling at 100 hPa and 43 hPa. The upwelling at the tropopause represents the total mass flux into the stratosphere within the BDC and is related to the outflow at all levels above in the stratosphere (with a small portion of it even related to outflow at levels above the stratopause). Therefore, changes in upwelling at this level reflect changes in the overall overturning circulation. The annual mean upwelling at 100 hPa, generated by all resolved waves and estimated using the DWCP, is approximately 9.9×10^9 kg/s in ERA5. In comparison, MERRA2 and ERA-Interim exhibit slightly weaker upwelling rates of about 9.5×10^9 kg/s, while JRA55 shows the weakest upwelling at this level, about 9.2×10^9 kg/s. The upwelling variability at this level is substantial, with the standard deviations estimated from deseasonalized monthly mean upwelling ranging from 1.2×10^9 kg/s to 1.4×10^9 kg/s across the reanalyses (Tab. 4.1). At 100 hPa, the planetary waves and resolved smaller-scale waves contribute comparably to the annual mean upwelling, with approximately 53% attributed to planetary waves and 47% to smaller-scale waves. In contrast, the other reanalyses exhibit a slightly greater contribution from planetary waves ranging from 58% for ERA-Interim to 61% for MERRA2. The upwelling at 100 hPa caused by planetary wave drag has a standard deviation comparable to that caused by smaller-scale waves (Tab. 4.1). Therefore, both planetary and smaller-scale waves contribute comparably to the forcing and variability of the whole overturning circulation.

Lin et al. (2013) divided the stratospheric circulation into a deep branch (above 30 hPa), a shallow branch (between 70 hPa and 30 hPa), and a transitional branch (between 100 hPa and 70 hPa). Although the lowest layer (100-70 hPa) is still influenced by tropospheric processes, our results show no clear indication of differences in wave driving for this layer compared to the layers above. Therefore, in the present study we aim at a dynamical separation of only the shallow and deep branches based on the circulation's wave driving.

The total outflow of the shallow branch can be estimated by subtracting the upwelling at the separation level (43 hPa) from the upwelling at the bottom of the stratosphere (100 hPa), as shown in Fig. 4.7b. In this 100-43 hPa layer, dissipation of the resolved waves generates an annual mean total outflow ranging from approximately 5.3×10^9 kg/s to 5.8×10^9 kg/s depending on the reanalysis. Roughly two-thirds of this outflow can

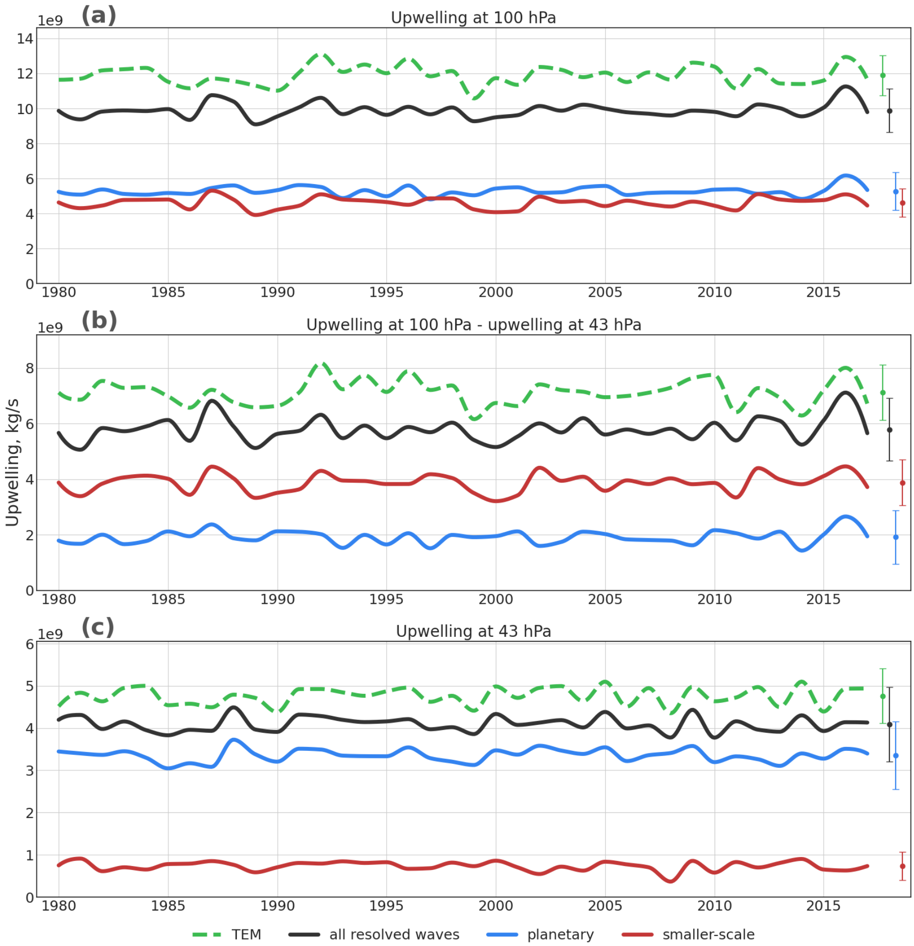

Figure 4.7: (a) Annual mean time series (1980–2017) of upwelling at 100 hPa based on ERA5 data. Shown are estimates from the TEM approach (green), total resolved wave drag (black), planetary wave drag (blue), and smaller-scale wave drag (red). Dots indicate mean values over the entire period, and error bars represent the standard deviation of monthly mean values, consistent with Tab. 4.1. (b) Difference in upwelling between 100 hPa and 43 hPa, using the same color scheme as in panel (a). (c) Upwelling at 43 hPa, again using the same legend as in panel (a).

Table 4.1: Climatological mean upwelling and standard deviation of deseasonalized monthly upwelling in 10^9 kg/s. All values are based on ERA5 1980-2017 data.

	total		planetary		smaller-scale	
level	W	σ	W	σ	W	σ
ERA5						
43 hPa	4.09	0.88	3.35	0.80	0.73	0.33
100 hPa - 43 hPa	5.79	1.14	1.91	0.97	3.88	0.82
100 hPa	9.88	1.24	5.27	1.07	4.61	0.80
ERA-Interim						
43 hPa	3.87	0.88	3.22	0.78	0.64	0.32
100 hPa - 43 hPa	5.58	1.17	2.23	0.97	3.35	0.79
100 hPa	9.45	1.27	5.45	1.1	4.00	0.76
JRA55						
43 hPa	3.92	0.92	3.33	0.83	0.60	0.31
100 hPa - 43 hPa	5.29	1.16	2.04	0.98	3.24	0.79
100 hPa	9.21	1.23	5.37	1.06	3.84	0.74
MERRA2						
43 hPa	4.05	0.90	3.43	0.82	0.62	0.33
100 hPa - 43 hPa	5.50	1.36	2.41	1.21	3.09	0.83
100 hPa	9.55	1.42	5.84	1.23	3.71	0.83

be attributed to smaller-scale waves, while only about one-third is attributed to planetary waves. However, the monthly mean standard deviations of the total outflow driven by planetary waves and smaller-scale waves indicate that both wave types contribute comparably to the variability of the total outflow in this layer, and hence to the variability of the shallow circulation branch.

The upwelling across the mean separation level is a result of the wave drag in the deep branch region above that level. The annual mean of this upwelling across the separation level is ranging from 3.9×10^9 kg/s to 4.1×10^9 kg/s depending on the reanalysis, the majority of which is caused by planetary waves and less than 20% by smaller-scale waves. The variability of the monthly mean upwelling across the separation level (43 hPa) is mostly controlled by planetary waves (see Fig. 4.7). This is indicated by the fact that variability (here measured in terms of standard deviation) of upwelling induced by planetary waves is more than two times larger compared to the variability of upwelling induced by smaller-scale waves (Tab. 4.1). Therefore, despite the clear separation in wave driving concerning the climatological mean circulation, both wave types contribute significantly to the circulation variability of the shallow branch, while the variability of the deep branch is mostly controlled by the planetary waves.

To further investigate the roles of planetary and smaller-scale waves in driving circulation variability, vertical profiles of standard deviation of tropical outflow attributed to planetary and smaller-scale waves were constructed, as well as vertical profiles of the correlation coefficients between the total outflow and the contributions by planetary or smaller-scale waves (Fig. 4.8). Planetary waves are relevant to the variability of the circulation throughout the stratosphere and generally contribute more to the overall variability of the circulation compared to smaller-scale waves. In the middle and upper stratosphere these large-scale waves clearly dominate the circulation variability, consistent with a particularly high standard deviation of upwelling (Tab. 4.1). At levels below about 25km, the contribution of planetary waves to the variability of the circulation weakens, while the contribution of smaller-scale waves increases, such that both wave types contribute comparably (Fig. 4.8). The generally higher impact of planetary waves on the variability of the circulation is possibly related to the fact that the standard deviation of the upwelling at 100 hPa takes into account changes in the wave drag from that level and all levels above (see Sect. 3.3). Filtering by the background wind according to the Charney-Drazin criterion (Eq. 3.10) more strongly affects the smaller-scale waves, hinders their upward propagation and therefore dampens their contribution to circulation forcing at upper levels. Hence, the wave drag of the planetary waves is distributed over a larger altitude range in the stratosphere compared to the wave drag of the smaller-scale waves. In summary, planetary waves significantly contribute to the variability of the circulation at all levels while smaller-scale waves only affect the circulation variability in the shallow branch region.

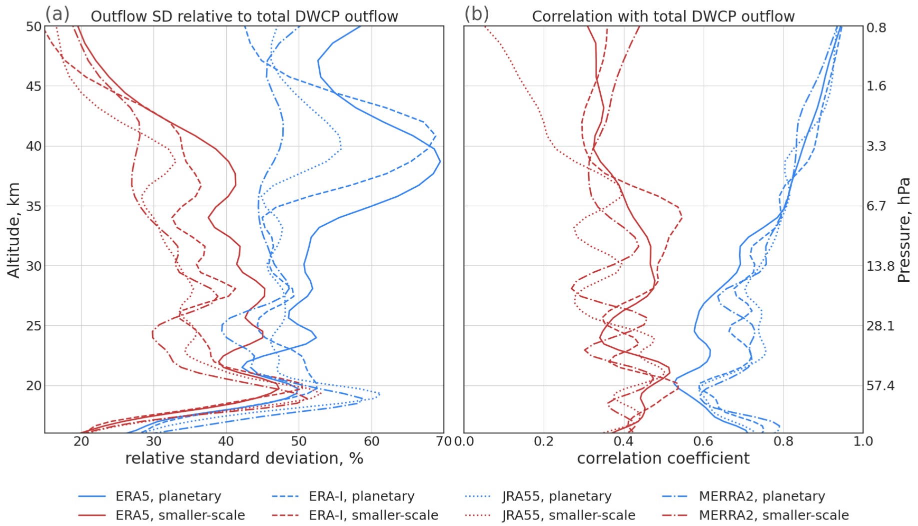

Figure 4.8: (a) Vertical profiles of tropical outflow variability, quantified by the standard deviation of DWCP outflow (blue lines driven by planetary wave drag, red lines by smaller-scale wave drag) relative to DWCP outflow driven by total resolved wave drag. (b) Vertical profiles of correlation coefficients between DWCP outflow driven by all waves and the outflow driven by only planetary (blue) and smaller-scale waves (red). Profiles have been constructed from 1980-2017 deseasonalized monthly mean data. The lines were smoothed with a Gaussian filter for better readability.

4.2.2 Trends

Multi-decadal trends in the upwelling over the period 1980–2017 are presented in Fig. 4.9. Given the relatively short period for trend calculation, upwelling trends are mostly not statistically significant at the 95% confidence level. It is known that BDC trends before and after about the year 2000 are affected by the opposite effects of ozone depletion and ozone recovery (e.g. Polvani et al., 2018; Abalos et al., 2019; Fu et al., 2019). Ozone depletion contributes to a BDC strengthening before 2000, strongest in the SH, while ozone recovery contributes to BDC weakening. However, dividing the analysis into the two sub-periods 1980-2000 and 2000-2017 did not enhance the significance of trends (not shown).

The trends of upwelling estimated from the TEM residual circulation velocity (black dotted lines in Fig. 4.9) and from the DWCP (black solid lines in Fig. 4.9) can differ significantly at different levels. While this work mostly focuses on the effects of resolved wave drag, most previous studies have concentrated on total upwelling derived from the TEM velocities (e.g. Fujiwara et al., 2022). Although the upwelling trends differ strongly between different altitude ranges, several consistent patterns in the trend profiles emerge for the different reanalyses. Above 25 km, the upwelling trend estimated from the total wave drag is positive and S-shaped for all four reanalyses with a local trend maximum around 35km. Strongest differences to the other reanalyses are found for MERRA2. In particular, at lower levels the shallow branch trend is mostly weakly positive for MERRA2, but negative for the other three reanalyses. For ERA5, ERA-Interim and JRA55 the deep branch trend is largely driven by planetary waves while for MERRA2 smaller-scale waves also contribute comparably to the trend. Furthermore, MERRA2 shows a generally more positive trend of upwelling driven by smaller-scale waves than that driven by planetary waves below about 30km, which is opposite to the other three reanalyses. For most reanalyses and levels the agreement between trends of upwelling estimated from the total resolved wave drag and from the TEM approach is poor. Only for ERA5 the trend from resolved wave drag matches the total TEM velocity-based trend well between about 23-35km. Also, ERA5 is the only reanalysis where the trend in the shallow branch is almost exclusively controlled by the smaller-scale waves, and which shows a significant contribution of resolved mesoscale waves to the overall trend of the shallow branch.

The robust difference in the contributions of planetary and smaller-scale waves to dominate the upwelling trends above and below about 22km (Fig. 4.9) corroborates our wave drag-based estimate of the separation level between the shallow and deep branch layers. In particular, different trends in dynamics are apparent in different altitude regions, indicating a decoupling of the two circulation branches regarding their long-term evolution. These differences in trends between the shallow and deep branch are consistent, at least qualitatively, for the different reanalyses.

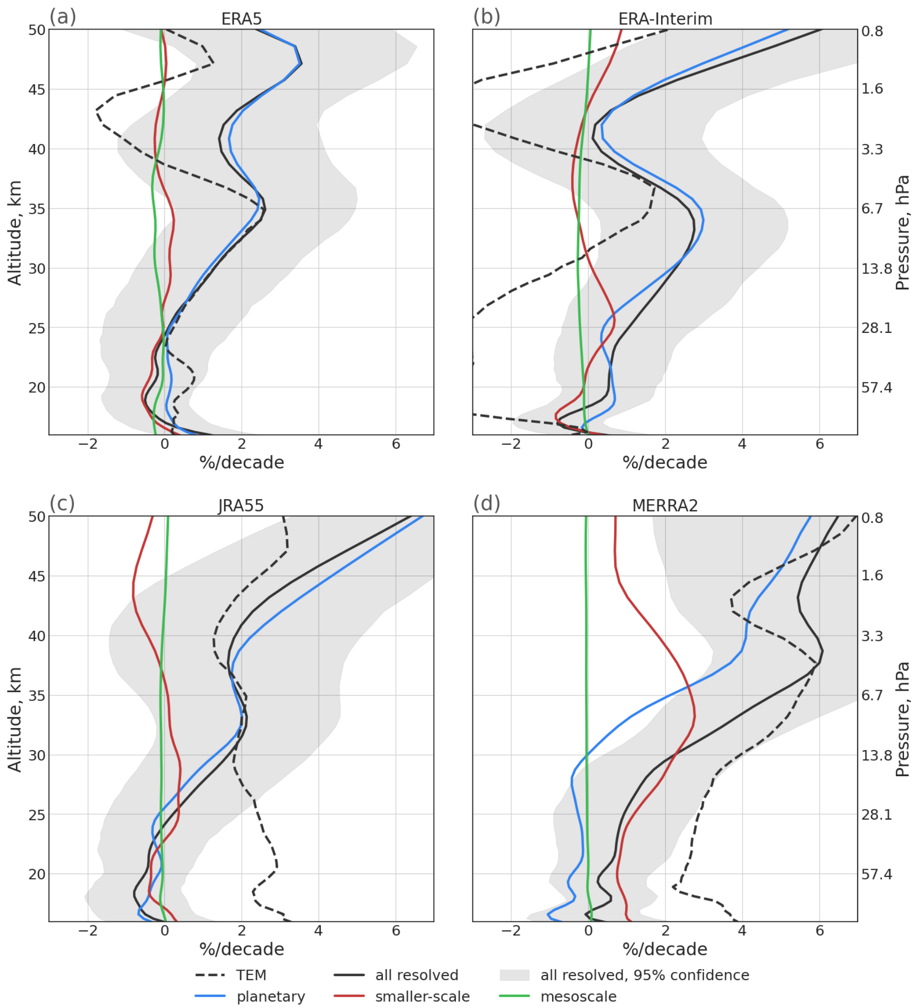

Figure 4.9: Vertical profiles of upwelling trend derived using TEM (dotted black line) or DWCP from total (black), planetary (blue), smaller-scale (red), and mesoscale (green) waves, gray shading denotes 95 percent confidence interval for total waves. The profiles were constructed from annual mean data for ERA5 (a), ERA-Interim (b), JRA55 (c), and MERRA2 (d). The lines were smoothed with a Gaussian filter.

The upwelling at a given level is driven by the wave drag at the level and all levels above it and hence the upwelling trend at a given level is not related unambiguously to wave drag changes only at that level. A clearer relation to wave drag changes at a given level holds for changes in meridional outflow at that level. Trend profiles for outflow are presented in Fig. 4.10 for the four different reanalyses and separated into contributions from smaller-scale and planetary waves. Given the relation to upwelling in Eq. 3.9, trends in outflow are directly related to the vertical derivative of the trends in upwelling. Therefore, the outflow trends are positive in a shallow layer above the tropical tropopause. Above, outflow shows generally negative trends throughout a broad layer between about 18-35km (somewhat depending on the reanalysis considered), and indicating weakening of transport out of the tropics in that altitude region. Above about 35km, outflow increases throughout an about 5km thick layer, consistent with the negative vertical gradient in upwelling trends in Fig. 4.9. Whereas most of the reanalysis-based trends are statistically insignificant, we hypothesize that the robust vertical pattern, with outflow weakening below and strengthening above about 35km, could be indicative of an upward shift of the deep branch of the stratospheric circulation. Another robust vertical pattern is the strengthening of outflow in the lower part of the shallow branch and weakening above, which could be indicative of a downward shift of the shallow branch of the stratospheric circulation. Overall, longer time-series are needed to deduce significant long-term trends of the stratospheric circulation from reanalysis data.

Given the limited period of the analyzed data and large inter-annual variability of the separation level height, the trend of the separation level for any of the reanalyses is not significantly different from zero. However, three out of four reanalyses show negative trends of the separation level height, while only JRA55 has a slightly positive trend (Fig. 4.11). The negative trend of the separation level can also be estimated from Fig. 4.10, which shows that the trend of large scale waves is generally more positive than the trend of small scale waves around the separation level. Hence the contribution of planetary waves around the separation level increases over time compared to the contribution of smaller-scale waves, and consequently pushes the separation level slightly downwards.

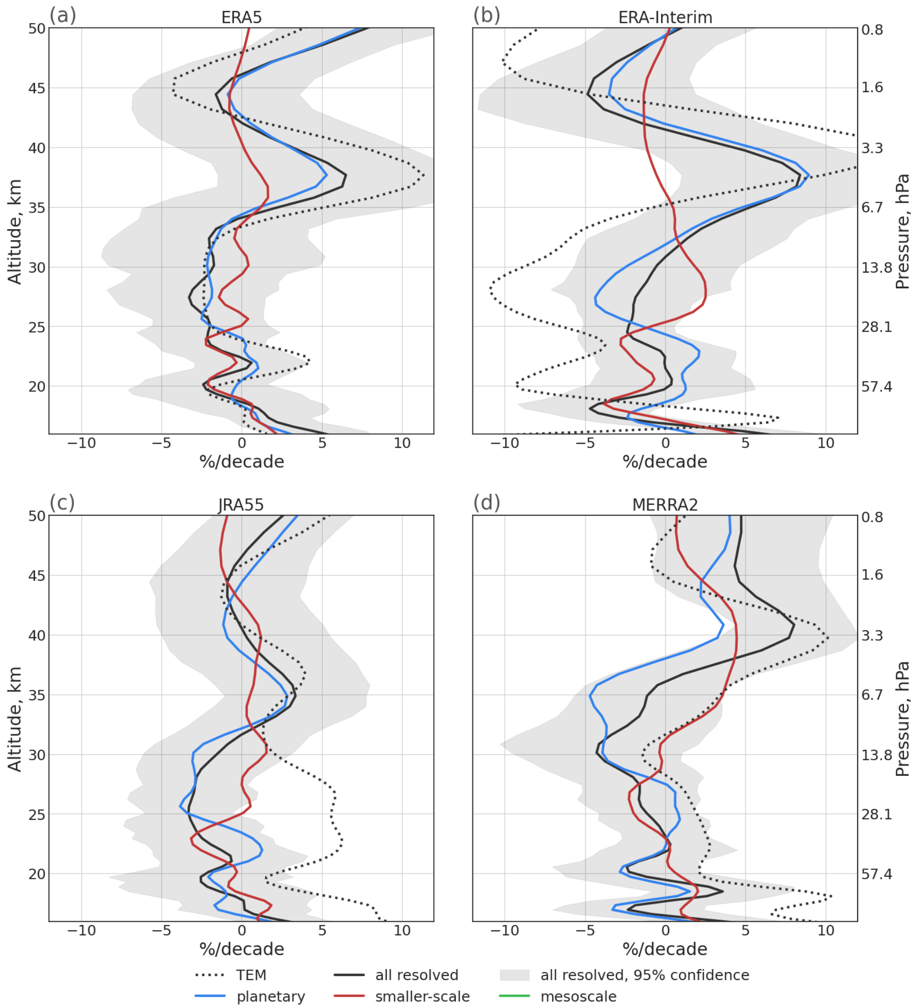

Figure 4.10: Vertical profiles of tropical outflow trend derived using TEM (dotted black line) or DC from total (black), planetary (blue), and smaller-scale (red) waves; the gray shading denotes the 95% confidence interval for total waves. The profiles were constructed from annual mean data of ERA5 (a), ERA-Interim (b), JRA55 (c), and MERRA2 (d). The lines were smoothed with a Gaussian filter.

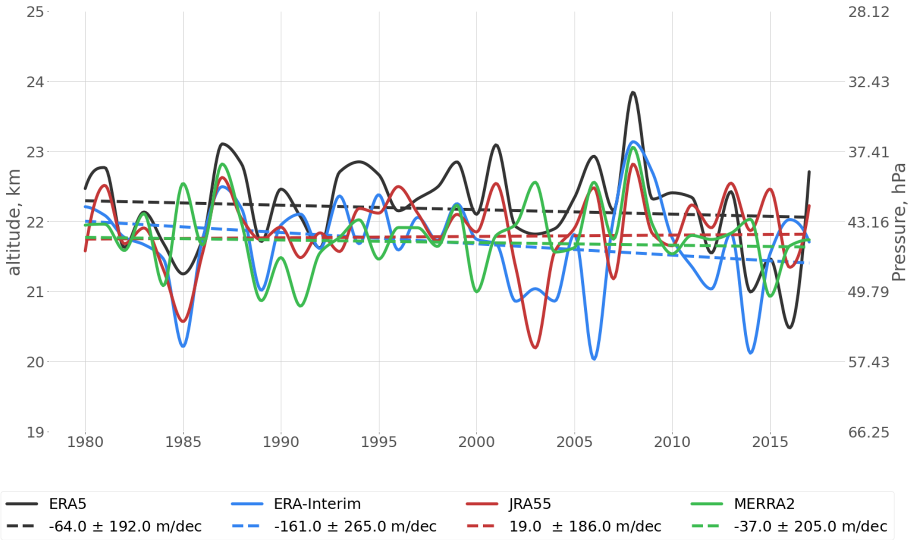

Figure 4.11: The variability and trend of the separation level between shallow and deep stratospheric circulation branches over the period 1980–2017 from ERA5 (black), ERA-Interim (blue), JRA55 (red), and MERRA2 (green). Solid lines represent the annual mean separation level and dashed lines show the linear trend based on the annual mean level. Decadal trend values ±2 standard error are given in the legend.

4.3 Discussion and summary

Past research has shown that the stratospheric circulation can be separated into a deep and a shallow branch (e.g. Birner and Bönisch, 2011; Plumb, 2002). However, different metrics have been used in past studies to separate these circulation branches. Some studies applied a separation by selecting a boundary pressure level which splits the upwelling mass flux approximately into a specific ratio between the deep and shallow branch, e.g. $\sim$50 hPa (Ball et al., 2016) or 30 hPa (Lin et al., 2013; Diallo et al., 2019). Since vertical velocities in the stratosphere are much weaker than horizontal ones, transit times from the stratospheric entry point at the tropical tropopause to the downwelling region in the extratropical lowermost stratosphere along the shallow branch are significantly lower than along the deep branch. Based on this difference in transit time, a separation between deep and shallow circulation branches has also been proposed based on transit times along residual circulation trajectories (Birner and Bönisch, 2011). Furthermore, the transport of air masses from the so-called "tropically controlled transition region" with an upper boundary at about 450K (approximately 70 hPa) into the extratropics is likely related to the shallow branch (Rosenlof et al., 1997; Bönisch et al., 2009; Bönisch et al., 2011). In view of such diversity in proposed separation between the shallow and the deep stratospheric circulation branch, here we aim for a dynamical separation based on differences in the circulation's wave driving as inferred from reanalysis data. The robustness of our results is estimated from comparison of four different reanalyses.

It is well established that the deep branch of the BDC is primarily driven by planetary waves which break in the subtropical middle and upper stratosphere, while the shallow branch is more strongly driven by synoptic waves which break in the subtropical lower stratosphere (e.g. Plumb, 2002). Our statistical and mechanistic analyses show that in current global reanalyses the outflow in the deep branch is indeed largely driven by planetary waves with wavenumbers 1–3. The shallow branch is mainly driven by synoptic-scale waves (wavenumbers 4 to 20) and to a lesser extent by mesoscale waves (wavenumbers larger than 20). It should be noted that, due to the coarse resolution of the current-generation reanalyses, the contribution of mesoscale, mainly gravity, waves in our study is likely underestimated, consistent with a significant DWCP upwelling deficit (Fig. A.2) and also with results by Butchart et al. (2011). For the resolved waves considered here, however, the wave drag-based separation of the deep and the shallow branch is robust across all four reanalyses used.

Based on the present study, the mean level separating the deep and the shallow branch of the residual circulation is located between 43 and 47 hPa depending on the reanalysis. Hence, despite using different arguments the separation level found in this work is close to the levels estimated in past studies. Moreover, this separation level between the two circulation branches was found to have an annual cycle, with lowest separation level during boreal summer, which is similar in all reanalyses used in this work. Both the inter-annual and seasonal variability of the separation level have an amplitude which is larger than the differences between the reanalyses.

Most of the residual circulation trends estimated in this work are within two standard errors of zero and therefore are not statistically significant. Yet there are patterns that robustly emerge in all reanalyses used, such as an acceleration of upwelling above 28 hPa, and mostly negative trends of outflow between 60 and 15 hPa. Remarkably, also the planetary wave contribution to the trends varies considerably between reanalyses, indicating that even large-scale waves are not sufficiently constrained in reanalyses with respect to trends. It should be noted that this study focuses solely on the resolved wave drag. Depending on the reanalysis, inclusion of the parameterized wave drag could significantly influence the results by increasing the contribution of smaller-scale waves to the circulation, which would likely shift the separation level upward.

The reanalysis data used here were down-sampled to 1°x 1°horizontal resolution and 6-hour temporal resolution. Figure 4.12 presents upwelling and outflow estimated using both fine resolution (0.3°x 0.3°x 1 hr) and coarse resolution (1°x 1°, 6 hr) ERA5 data for the year 2010. The overall structure of the vertical profiles of upwelling remains largely unaffected by the down-sampling of the reanalysis data. The most notable effect of down-sampling is found for waves with wavenumbers greater than 180, for which all information is lost. For the original, high-resolution data, these very small-scale waves add a significant contribution to the driving of the shallow BDC branch in the lower stratosphere. Upwelling near the tropopause associated with waves 21 to 180 is reduced by about 20%, and consequently the total upwelling at that level decreased by about 1.5%. Similarly, outflow near the separation level generated by waves 21 to 180 is reduced by about 5%, with a corresponding total outflow reduction of around 1.3%. The separation level height has decreased by about 0.2 km or 1 hPa.

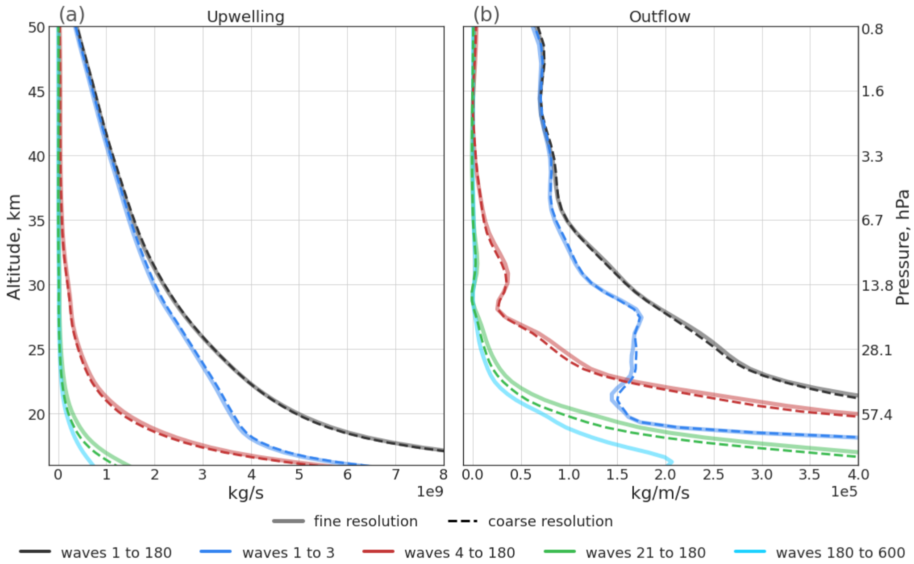

Figure 4.12: (a) Vertical profiles of mean upwelling estimated with DWCP from fine (solid lines, 0.3°, 1hr) and coarse (dashed lines, 1°, 6hr) resolution ERA5 data for year 2010 and driven by all resolved wave drag (black lines), planetary wave drag (blue lines), smaller-scale wave drag (red lines), mesoscale wave drag (green lines), and small-scale mesoscale wave drag (cyan line). (b) equivalent to (a) with vertical profiles of mean outflow. As in the other figures, the TAL are estimated from coarse resolution data. The lines presented in this figure were smoothed with a Gaussian filter.

Overall, the down-sampling to coarser spatial resolution did not significantly affect the large-scale features of the residual circulation considered here (see Fig. A.4 and Fig. A.5). As also shown by Seviour et al. (2011), from a climatological monthly-mean perspective the 6-hourly data is sufficient to take tidal effects into account. Furthermore, for 6-hourly temporal resolution some distortions remain in monthly mean data for $\bar{w}^*$ (Fig. A.5), while few to no distortions remain for $\nabla \cdot F$ (Fig. A.4). Regarding daily mean data for specific dates, reducing the temporal resolution from 1 to 6 hours has a significant impact on the representation of the residual circulation. Therefore, in order to investigate short-term and smaller-scale features of the circulation it seems important to use higher temporal resolution than 6 hours. Nevertheless, the overall characteristics of the circulation on the monthly timescale are affected by the down-sampling only to a limited and acceptable extent.

Vertical profiles of upwelling estimated using the TEM approach for all four reanalyses are shown in Fig. A.2 together with the difference to the DWCP upwelling estimate ($(W - W_D)/W * 100\%$ denoted relative "upwelling deficit" in the following), which is used to estimate the contribution of parameterized wave drag to the upwelling. For all four reanalyses, the vertical profile of the upwelling deficit shows a C-shape, with a higher deficit in both the lowest and upper parts of the stratosphere. This C-shape of the deficit indicates that the parameterized wave drag in the reanalyses mostly affects the lowest and highest parts of the stratosphere. This effect is likely related to the contribution of unresolved gravity wave drag to both the mesospheric circulation and to the shallow branch of the stratospheric circulation (e.g. Diallo et al., 2019; Eichinger et al., 2020), which is not fully resolved in the reanalysis data. Due to its higher resolution and greater ability to resolve mesoscale gravity waves, ERA5 shows significantly stronger mesoscale wave drag (cf. Fig. 4.5 and Sect. 4.1). Thus, ERA5 has the smallest upwelling deficit in the lower and upper stratosphere. In the middle stratosphere the difference between ERA5, MERRA2 and ERA-Interim is small, likely related to the small contribution of mesoscale waves at these levels. Throughout the stratosphere, JRA55 shows the largest deficit among all four reanalyses considered.

Furthermore, ERA5 shows the strongest total resolved upwelling and outflow at the bottom of the stratosphere (see Fig. A.3b). This indicates that the total resolved wave drag is about 5 to 10% greater in ERA5 than in the other reanalyses. The total TEM-based upwelling at the same altitude, including effects from parameterized waves, is significantly weaker in ERA5 than in ERA-Interim or JRA55, therefore the results are consistent with Ploeger et al. (2021). At the top of the stratosphere, the TEM upwelling in ERA5 is 20 to 30% weaker than in the other reanalyses (see Fig. A.3a).

In general, the upwelling based on the different reanalyses is more similar when estimated from resolved waves only (Fig. A.3a, b). When considering the upwelling deficit, the difference between the full TEM–based and the DWCP–based upwelling, differences between the reanalyses may indicate differences in the gravity wave parameterization. In particular, ERA5 has generally stronger upwelling estimated from the resolved wave drag and weaker TEM upwelling in the regions where the effect of small-scale gravity wave drag on the circulation is expected to be strongest. Therefore, the smaller upwelling deficit in ERA5 is likely due to a better ability to resolve the waves and also from weaker parameterized wave drag.

Finally, it should be noted that throughout this work, we have used a scale-based separation of atmospheric waves. An additional important question would be a separation of the waves into physical wave classes like Rossby and gravity waves. Although the scale separation does not necessarily represent a physical classification, it provides some insights into the physical types of waves. Planetary waves 1–3, as found here to constitute the driving force of the deep circulation branch, are large-scale Rossby waves. Comparison of $\nabla \cdot F$ with studies based on physical wave models (e.g. Koval et al., 2023) shows that these large-scale Rossby waves in the lower to middle stratosphere are mostly stationary or quasi-stationary. Furthermore, the mesoscale waves with wavenumbers 20–180, as found here to drive mainly the shallow branch, are likely associated with gravity waves. Since in the lower stratosphere Kelvin waves are confined to the tropics and typically do not extend to the vicinity of the TAL where the main driving of tropical upwelling occurs, they are likely of limited relevance for the present study (Ern and Preusse, 2009; Yang et al., 2003; Smith et al., 2002). At higher altitudes above the stratopause, a broader range of physical wave types becomes increasingly important (cf. Koval et al., 2023; Yasui et al., 2021). Since reanalyses data do not inherently distinguish between wave modes, a precise quantification of contributions from different physical wave types is beyond the scope of this study. However, incorporating a more physically based separation of wave types, in particular of the intermediate waves (here wavenumbers 3 and 4), would be a valuable direction for future research.

Based on the results of this chapter, we propose a dynamical separation between the deep and shallow branches of the stratospheric residual circulation. The deep branch of the BDC is primarily driven by planetary waves with wavenumbers 1 to 3, while the shallow branch is driven by smaller-scale waves with wavenumbers greater than 3. The mean altitude of the level separating these branches is approximately 22 km (43 hPa), with notable inter-annual and seasonal variability. Although the circulation trends were not found to be statistically significant, common features emerged robustly across the four reanalyses. These common features are: (i) a strengthening of the tropical outflow at altitudes around 35–40 km and (ii) a weakening below, which together potentially indicate an upward shift of the deep circulation branch.

Chapter 5

Isentropic mixing related to deep and shallow circulation branches

Different dynamical regimes associated with the deep residual circulation branch in the middle and upper stratosphere and with the shallow branch in the lower stratosphere were shown in the previous chapter to be related to distinct wave bands. Similarly to the residual circulation, isentropic mixing is an essential component of the BDC, and is also related to stirring by atmospheric waves. Isentropic mixing acts to weaken gradients of trace gases, thereby significantly influencing their distribution and the composition of the stratosphere. In this chapter, we aim to investigate whether and how the occurrence of the deep and shallow BDC branches imprints on the characteristics of isentropic mixing.

5.1 Tracer transport

A key control factor for tracer transport in the stratosphere is the large-scale residual circulation that transports air upward in the tropics and downward in the extratropics. Superimposed on this mean flow are eddy-driven processes, particularly isentropic mixing, which acts quasi-horizontally along surfaces of constant potential temperature and contributes significantly to the redistribution of trace gases. While the residual circulation predominantly shapes the meridional and vertical gradients of tracers, such as ozone, water vapor, and long-lived species, two-way mixing processes gradually dissolve gradients. Hence, these processes play an important role for shaping the boundaries that separate distinct air masses near the transport barriers in the subtropical lowermost stratosphere, around the polar vortex and at the edges of the tropical pipe. This interplay between mean circulation and mixing is essential for understanding stratospheric composition, radiative forcing, and the stratosphere-troposphere exchange of trace constituents.

The method for separation of residual circulation and mixing effects on tracer transport used here generally follows **?**or that purpose, the tracer transport equation is used to investigate the effects of eddy mixing, in relation to the residual circulation. The formulation of the mean tracer transport equation in log-pressure coordinates within the TEM framework is given by Andrews et al. (see 1987, Eq. 9.4.13)

$$\partial_t\overline{\chi} = \overline{S} - \bar{v}^*\,\partial_\phi\overline{\chi} - \bar{w}^*\,\partial_z\overline{\chi} + \rho_0^{-1}\nabla\cdot M \tag{5.1}$$

where χ is the tracer gas mixing ratio, S represents chemical sources and sinks, $\nabla\cdot$ denotes the divergence operator, and M is the eddy flux vector. Horizontal and vertical components of the eddy flux vector in log-pressure coordinates are

$$M^{(\phi)} = -\rho_0(\overline{v'\chi'} - \overline{v'\theta'}\,\partial_z\overline{\chi}/\partial_z\overline{\theta})\,, \tag{5.2a}$$

$$M^{(z)} = -\rho_0(\overline{w'\chi'} + \overline{v'\theta'}\,\partial_\phi\overline{\chi}/\partial_z\overline{\theta}) \tag{5.2b}$$

The second term on the right-hand side of Eq. 5.1 contains the effect of horizontal advective transport by the residual circulation, while the third term contains the effect of vertical advective transport. The last term contains effects of vertical and horizontal transport by eddy mixing.

In a stably stratified atmosphere, the surfaces of constant potential temperature (isentropes) approximate the direction of minimal resistance to motion. Therefore, eddy mixing occurs mostly horizontally along isentropes and is frequently called isentropic mixing. Hence, the eddy mixing is more appropriately analyzed using potential temperature θ as the vertical coordinate. For that reason, most of the analysis in this chapter (besides Fig. 5.1) has been carried out in isentropic coordinates.

The diabatic mean circulation in isentropic coordinates, the analogue to the residual mean circulation in log-pressure coordinates, takes the following form:

$$\bar{v}^* = \overline{\sigma v}/\overline{\sigma}\,, \tag{5.3a}$$

$$\overline{Q}^* = \overline{\sigma Q}/\overline{\sigma}\,, \tag{5.3b}$$

where $\sigma = -g^{-1}\partial_\theta p$ represents the density in isentropic coordinates, with g denoting the acceleration due to gravity, v is the meridional wind on isentropic surfaces and Q the cross-isentropic vertical velocity. Hence, $\bar{v}^*$ is the meridional component of the diabatic mean circulation in isentropic coordinates, $\overline{Q}^*$ its vertical component. The density term in Eq. 5.3 serves to ensure mass-weighting which is essential for accurately representing the distribution of air mass on isentropic surfaces.

The transport equation for trace gas mixing ratio in isentropic coordinates is (see Andrews et al., 1987, Eq. 9.4.21)

$$\partial_t \bar{\chi} = \bar{S} - \frac{\bar{v}^*}{a}\partial_\phi \bar{\chi} - \overline{Q}^* \partial_\theta \bar{\chi} + \frac{1}{\bar{\sigma}}[\nabla \cdot M - \partial_t(\overline{\sigma' \chi'})]\,. \tag{5.4}$$

Similarly to Eq. 5.1, the second and third terms on the right-hand side of Eq. 5.4 contain the effects of horizontal and vertical advective transport by the residual circulation. The last term contains the effect of eddy mixing, with the horizontal and vertical components of the eddy flux vector M given by

$$M^{(\phi)} = -\overline{(\sigma v)'\chi'}\,, \tag{5.5a}$$

$$M^{(\theta)} = -\overline{(\sigma Q)'\chi'}\,. \tag{5.5b}$$

As air ages homogeneously throughout the stratosphere at a constant rate of 1, Eq.

5.4 for Γ takes the following form

$$\partial_t \bar{\Gamma} = [1 - \frac{\bar{v}^*}{a} \partial_\phi \bar{\Gamma} - \overline{Q}^* \partial_\theta \bar{\Gamma}] + \frac{1}{\bar{\sigma}} [\nabla \cdot M^\Gamma - \partial_t (\overline{\sigma' \Gamma'})] \,. \tag{5.6}$$

The transient term $\partial_t (\overline{\sigma' \Gamma'})$ was found to be negligibly small and is therefore neglected in all results presented in this thesis. Hence, horizontal ($\mu^{(\phi)}$) and vertical ($\mu^{(\theta)}$) AoA mixing tendencies are defined as

$$\mu^{(\phi)} = \bar{\sigma}^{-1} \, \nabla \cdot M^{\Gamma(\phi)} = -\bar{\sigma}^{-1} \partial_\phi [\overline{(\sigma v)' \Gamma'}] \, / \, (\bar{\sigma} \, a \, \cos(\phi)) \,, \tag{5.7a}$$

$$\mu^{(\theta)} = \bar{\sigma}^{-1} \, \nabla \cdot M^{\Gamma(\theta)} = -\bar{\sigma}^{-1} \partial_\theta [\overline{(\sigma Q)' \Gamma'}] \, / \, \bar{\sigma} \,. \tag{5.7b}$$

Similarly to the decomposition of the EP flux by wavenumber, contributions of different waves to the mixing tendencies are estimated by applying a Fourier transform to the eddy components of the relevant meteorological fields. Covariances are then calculated as functions of wavenumber, from which the wave-resolved mixing tendencies are subsequently derived

$$\mu^{(\phi)}(s) = -2 \, \mathrm{Re} \; \partial_\phi [\widehat{(\sigma v)}(s) \hat{\Gamma}^*(s)] \, / \, (\bar{\sigma} \, a \, \cos(\phi) \, n_s^2) \,, \tag{5.8a}$$

$$\mu^{(\theta)}(s) = -2 \, \mathrm{Re} \; \partial_\theta [\widehat{(\sigma Q)}(s) \hat{\Gamma}^*(s)] \, / \, (\bar{\sigma} \, n_s^2) \; . \tag{5.8b}$$

Here Re denotes the real part of a complex number, asterisks denote complex conjugates, hats represent Fourier coefficients, s is the wavenumber index, and n_s is the sample size (number of longitudinal grid points). Note that summation over all wave components in the $\mu(s)$ from Eq. 5.8 yields values that are almost identical to those of μ in Eq. 5.7, such that numerical uncertainties in the calculation are negligible.

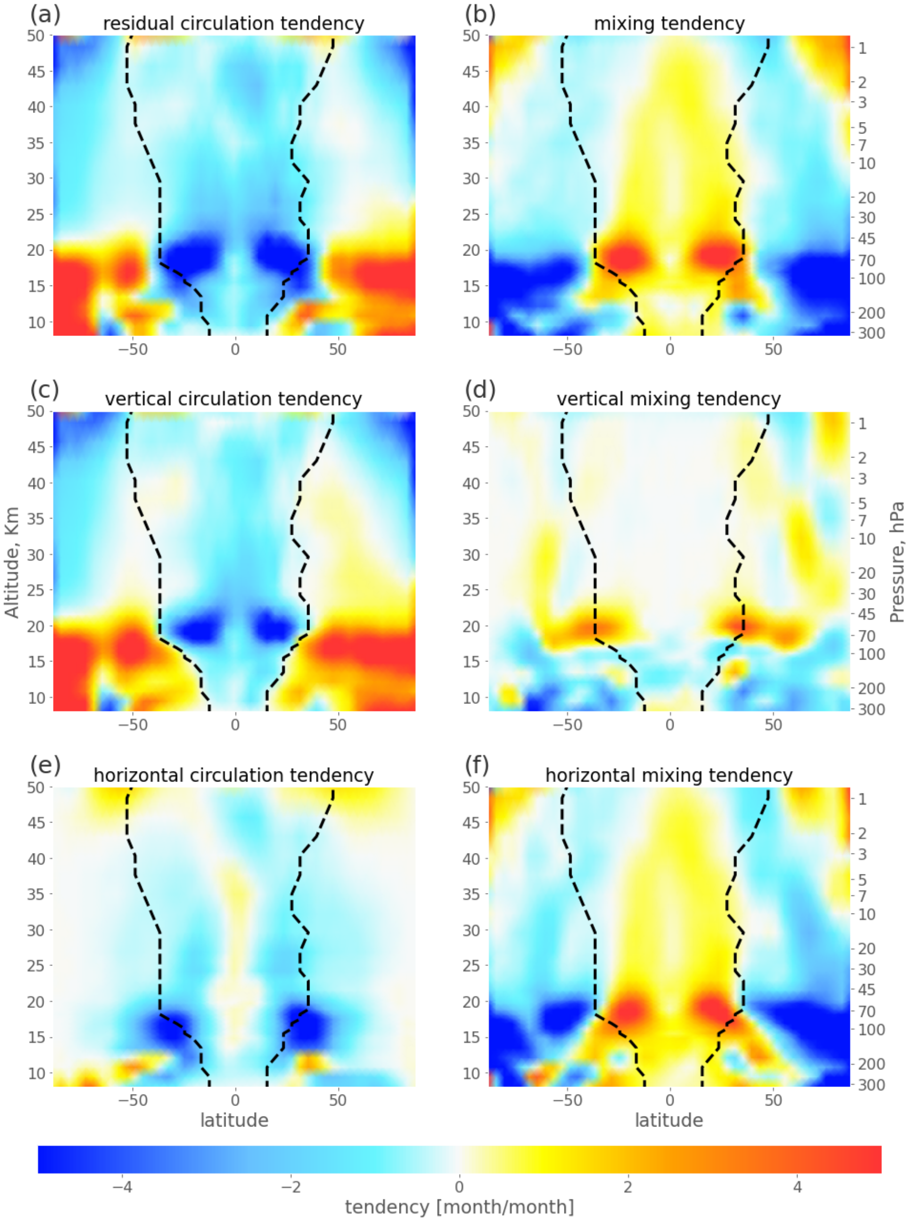

Figure 5.1: Contributions of residual circulation (left) and eddy mixing (right) to the mean age tendency budget derived from log-pressure AoA transport equation Eq. 5.1. The (a, b) full tendencies, (c, d) their vertical components, and (e, f) their horizontal components. The black dashed lines represent TAL. The figure is based on mean 1980–2017 ERA5 driven CLaMS data.

In general, effects of chemistry complicate the interpretation of trace gas changes in terms of transport. Therefore, in this and the following two sections, AoA is used as an idealized tracer for investigating tracer transport, which is influenced solely by transport and not by chemistry. The climatological mean distributions of vertical and horizontal tendencies of the residual circulation and eddy mixing for AoA in log-pressure coordinates are illustrated in Fig. 5.1. The figure shows that the tendencies associated with residual circulation and eddy mixing frequently exert opposing effects. The residual circulation transports young, tropospheric air into the tropical lower stratosphere and further upwards through the so-called tropical pipe, hence causing negative tendencies in that region. In the extratropical lower stratosphere, residual circulation downwelling of relatively old air masses from above causes positive tendencies, hence increases in age. In most regions of the stratosphere, vertical residual circulation transport effects dominate over horizontal residual circulation transport effects, except in the subtropical lower stratosphere.

Eddy mixing, on the other hand, causes stronger transport in the horizontal than vertical direction (Fig. 5.1). Hence, mixing mainly exchanges air masses between low and high latitudes, for instance transporting air across the TAL. This process mixes younger tropical air with older extratropical air, thereby increasing the age of air in the tropics and decreasing age in the extratropics.

The tendencies of both the residual circulation and eddy mixing are strongest in the lower stratosphere, corresponding to the shallow branch region below approximately 45 hPa. These tendencies become significantly weaker in the middle stratosphere (above approximately 45 hPa and extending up to the upper boundary of the tropical pipe or about 10 hPa). In the upper stratosphere above the tropical pipe (above about 10 hPa), these tendencies weaken even further.

As mixing processes mostly occur along surfaces of constant potential temperature, isentropic coordinates are advantageous to study mixing tendencies. Transport tendencies in isentropic coordinates are calculated from the isentropic transport equation for AoA (Eq. 5.6), and are presented in Fig. 5.2. This figure presents the total transport tendencies due to residual circulation and eddy mixing, along with their respective hor-

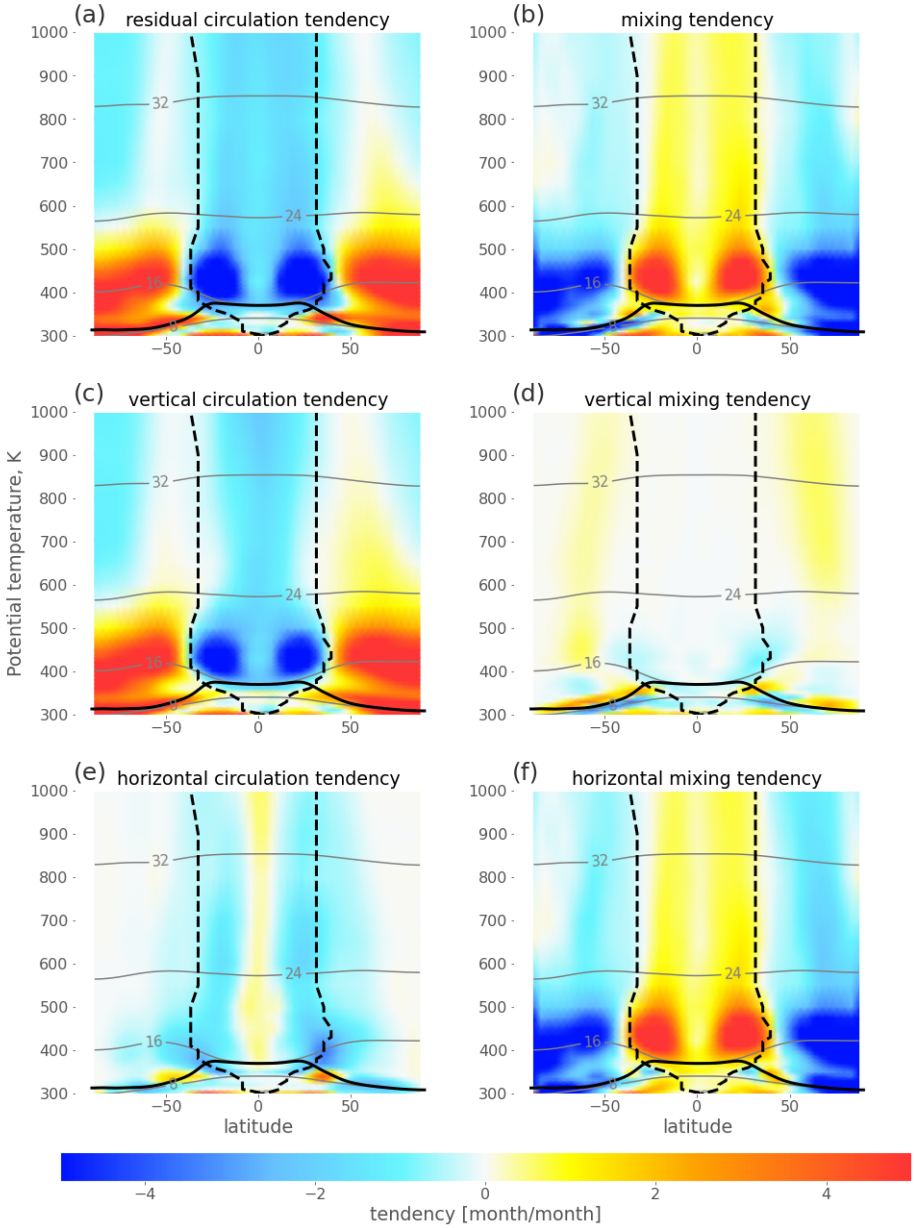

Figure 5.2: Contributions of residual circulation (left) and eddy mixing (right) to the mean age tendency budget derived from AoA transport equation Eq. 5.6. The (a, b) full tendencies, (c, d) their vertical components, and (e, f) their horizontal components. Altitude levels are shown as gray lines, TAL are shown as black dashed lines. The figure is based on mean 1980–2017 ERA5 driven CLaMS output.

izontal and vertical components. It is particularly evident in isentropic coordinates that the residual circulation tendency is primarily governed by its vertical component, while the mixing tendency is largely dominated by its horizontal component. A comparison between log-pressure coordinates (Fig. 5.1) and isentropic coordinates (Fig. 5.2) shows that the climatological tendency fields become significantly smoother when expressed in isentropic coordinates. Both the vertical mixing tendency and the horizontal component of the residual circulation tendency are considerably weaker in isentropic coordinates. Especially the vertical mixing tendency becomes almost negligible compared to its horizontal counterpart. Hence, for the analysis in this chapter, the horizontal eddy mixing tendency is used as a diagnostic of isentropic mixing within the BDC. Additionally, in isentropic coordinates the climatological TAL become more continuous and their positions shift such that the climatological TAL closely aligns with the climatological boundary between regions of positive and negative mixing tendencies.

5.2 Climatology of isentropic mixing

A separation of the contributions of different waves to the mixing tendency can be achieved by applying a Fourier transformation with respect to zonal wavenumber to the relevant meteorological fields, following Eq. 5.8. The climatological annual mean distributions of the respective mixing tendencies for AoA related to different waves are presented in Fig. 5.3. The figure shows that smaller-scale waves are more actively driving the mixing tendencies in the region between the tropopause and approximately the 500 K level. In this altitude range, dissipation of smaller-scale waves results in negative mixing tendencies in the middle latitudes, while dissipation of planetary waves leads to negative mixing tendencies in the polar and adjacent regions. Additionally, in the same region, planetary waves generate positive mixing tendencies poleward of the TAL in the middle latitudes. Interestingly, at levels above 500 K, where mixing is predominantly driven by planetary waves, positive mixing tendencies in the middle latitudes are instead generated by smaller-scale waves. Overall, Fig. 5.3 suggests a potential separation similar to that identified for the residual circulation (see Sect. 4.1.2), in which planetary waves more actively drive mixing in the middle and upper stratosphere, while smaller-scale waves contribute predominantly to mixing in the lower stratosphere.

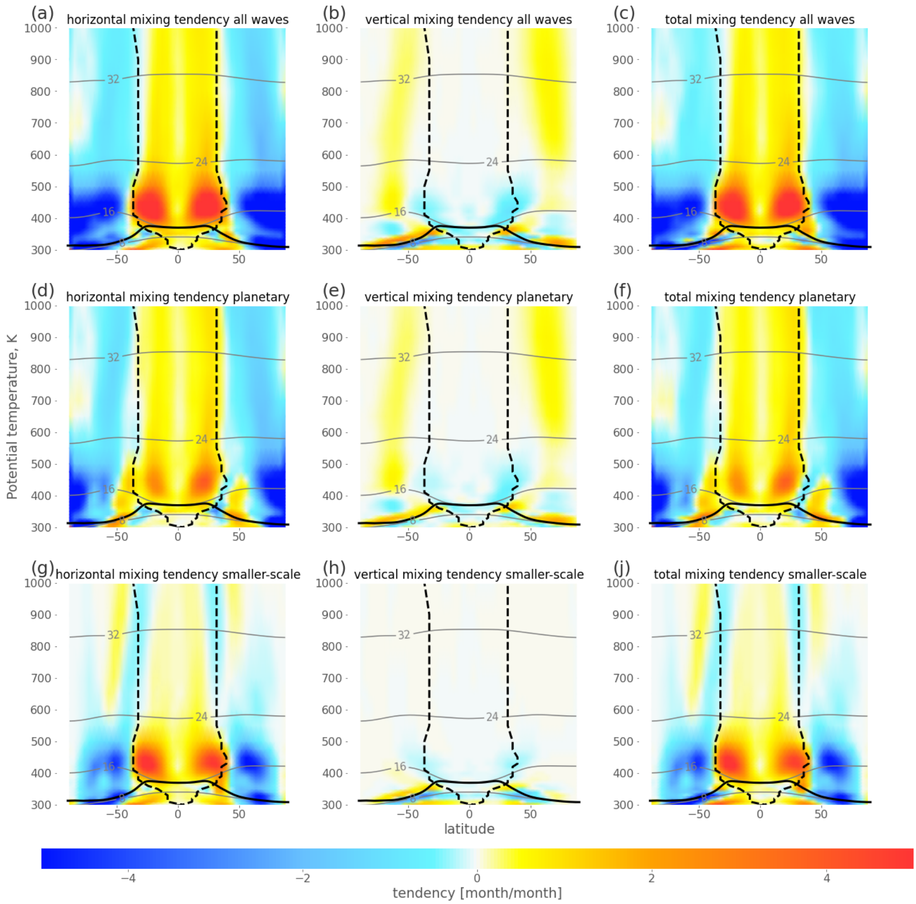

Figure 5.3: Total contribution of eddy mixing to the mean age tendency budget (right), its horizontal component (left), and its vertical component (center). From all resolved waves (a, b, c), planetary waves (g, h, j), and smaller-scale waves (d, e, f). Altitude levels are shown as gray lines, TAL are shown as black dashed lines. The figure is based on mean 1980–2017 ERA5 driven CLaMS data.

To assess the robustness of the results, the subsequent analysis in this and following sections is conducted using four different reanalyses. First, Figs. 5.4 and 5.5 present winter and summer distributions of horizontal mixing tendencies for analysis of seasonal differences. Comparison of these figures shows that the stratospheric distribution of isentropic mixing exhibits pronounced seasonality. Driven by wave dissipation, mixing strength follows the waves' dissipation rates and is consistently stronger during DJF than JJA across all four reanalyses. Furthermore, similar to effects of the overturning circulation, the isentropic mixing effects extend deeper into the stratosphere in the winter hemisphere, while being notably shallower in the summer hemisphere. Also, the strength of isentropic mixing generally decreases with altitude (see Figs. 5.4 and 5.5). In the summer hemisphere, where summertime stratospheric easterlies inhibit Rossby waves from propagating to higher altitudes, related mixing effects cease around 22km, while they reach much higher in the winter hemisphere. Interestingly, at lower levels below about 22km, negative mixing tendencies appear to be somewhat more pronounced in summer than winter. Another interesting feature is poleward mixing of older air at altitudes above 600 K in the polar vortex.

To derive vertical profiles of mixing tendencies, regions in the tropics with positive mixing values are isolated and the tendencies are integrated over the latitude–longitude extent of the isolated regions (between the dash-dotted lines in Figs. 5.4 and 5.5). The profiles of isentropic mixing tendencies driven by different waves are presented in panel (a) of Fig. 5.6, for ERA5 reanalysis. These profiles reflect the vertical distribution of horizontal AoA gradients (see Fig. 2.3), which are significantly stronger in the lower stratosphere than at higher altitudes. Consequently, the mixing tendency profiles exhibit a pronounced peak in the lower stratosphere.

Panel (b) of Fig. 5.6 presents the profiles of relative mixing tendencies, representing the fractional contribution of each wave type to the total mixing. These relative profiles are less influenced by the vertical structure of the tracer gradients and therefore provide a clearer basis for distinguishing the contributions of different wave types to the isentropic mixing. The relative contribution of waves 1 and 2 generally increases with altitude; to-

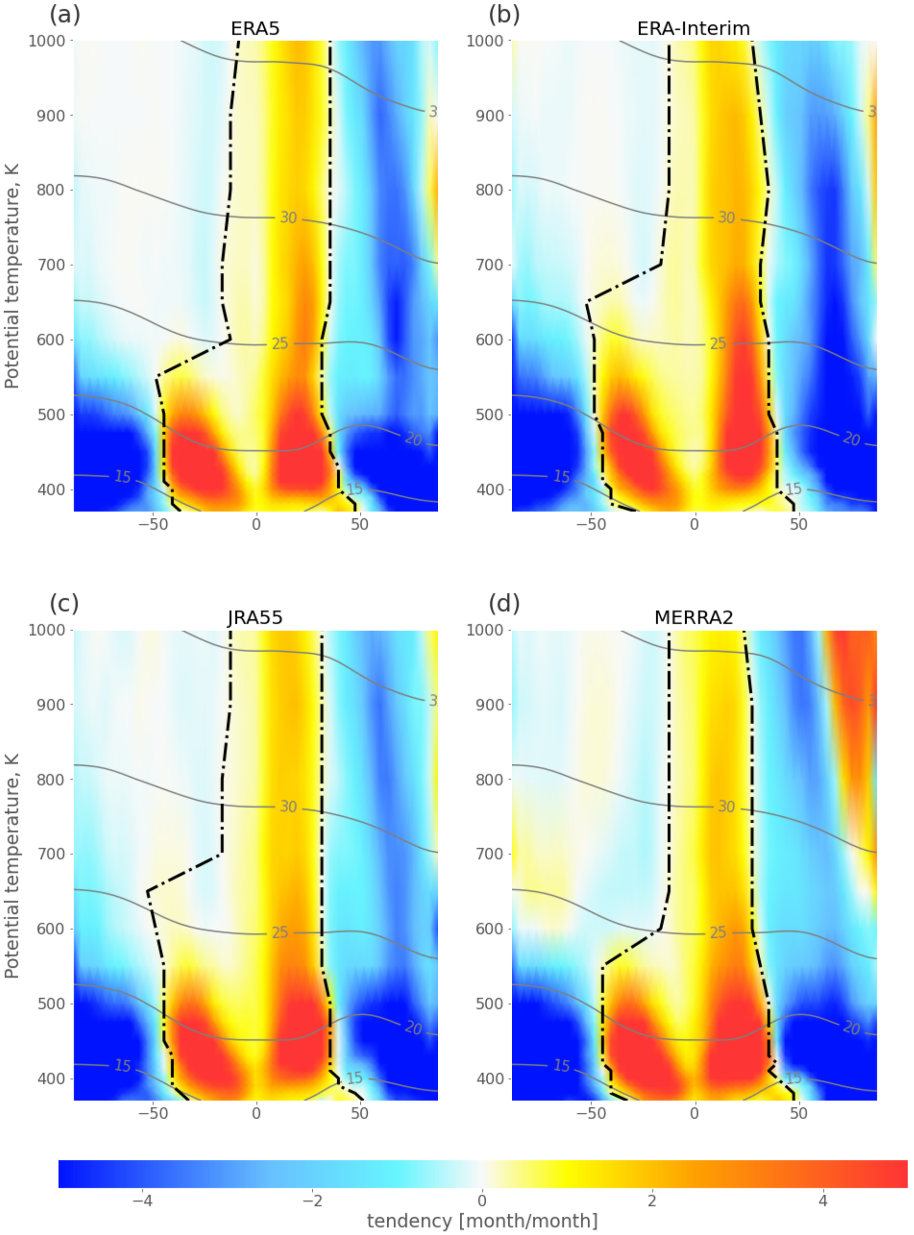

Figure 5.4: Climatological distribution of horizontal mixing tendency during DJF. Panels show CLaMS output driven by ERA5 (a), ERA-Interim (b), JRA55 (c), and MERRA2 (d). Black dash-dotted lines delineate the regions of positive tropical mixing tendency, gray lines indicate altitude levels. The figure is based on the 1980–2017 climatological mean.

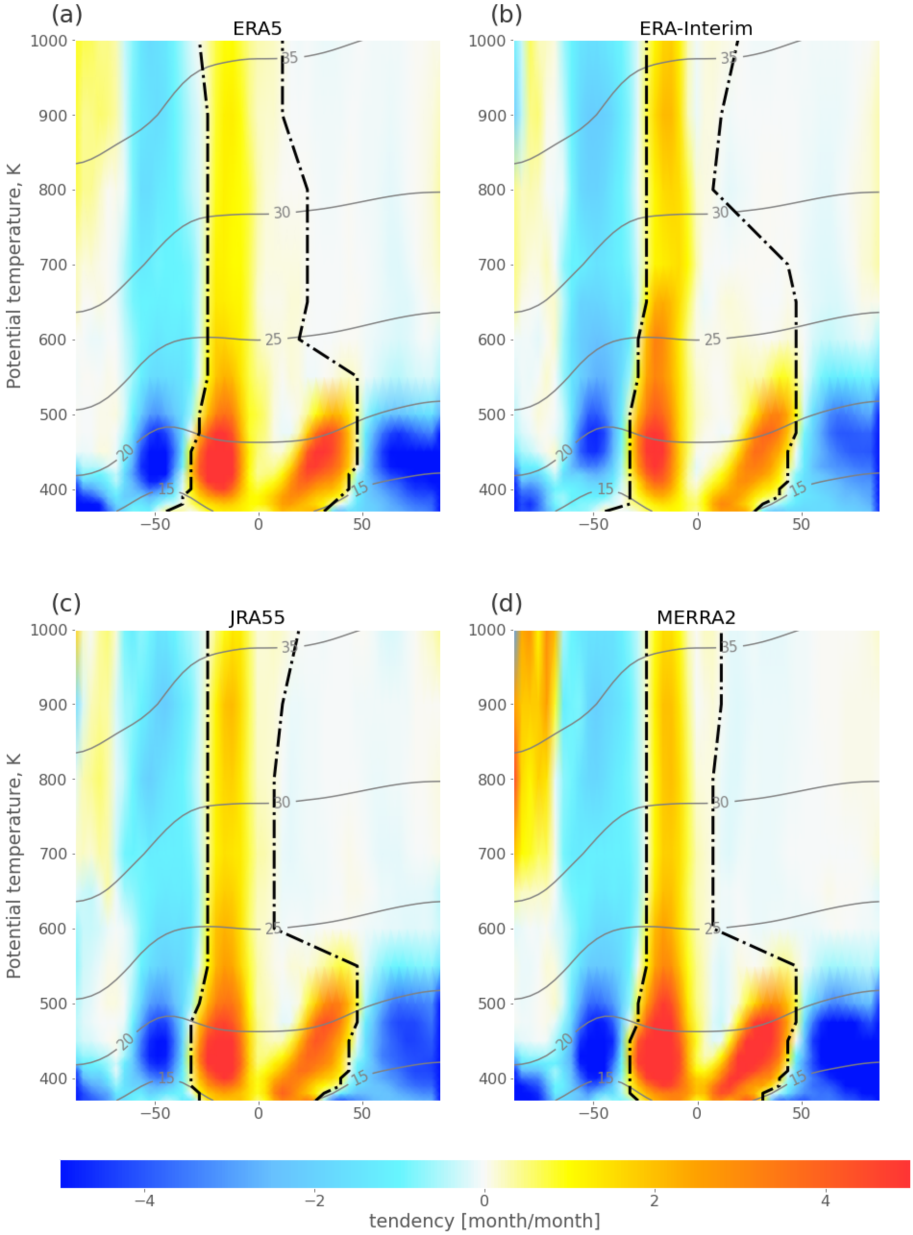

Figure 5.5: Climatological distribution of horizontal mixing tendency during JJA. Panels show CLaMS output driven by ERA5 (a), ERA-Interim (b), JRA55 (c), and MERRA2 (d). Black dash-dotted lines delineate the regions of positive tropical mixing tendency, gray lines indicate altitude levels. The figure is based on the 1980–2017 climatological mean.

gether, they account for most of the isentropic mixing in the upper stratosphere. Wave 3 contributes significantly in the lower stratosphere, yet remains active in the middle and upper stratosphere, albeit with a lower relative impact compared to waves 1 and 2. Overall, the contribution of wave 3 to isentropic mixing is still stronger in the middle and upper stratosphere than in the lower stratosphere. Wave 4 plays a significant role in the lower stratosphere, with its contribution peaking near 500 K and gradually declining with altitude. Together, waves 5 and higher-order waves dominate isentropic mixing in the lower stratosphere. However, their contribution decreases sharply in the middle stratosphere and becomes almost negligible in the upper stratosphere. Other reanalyses show similar wave contributions to the mixing (not shown). This suggests that the separation of wave driving for isentropic mixing closely mirrors the wave separation observed for the overturning circulation.

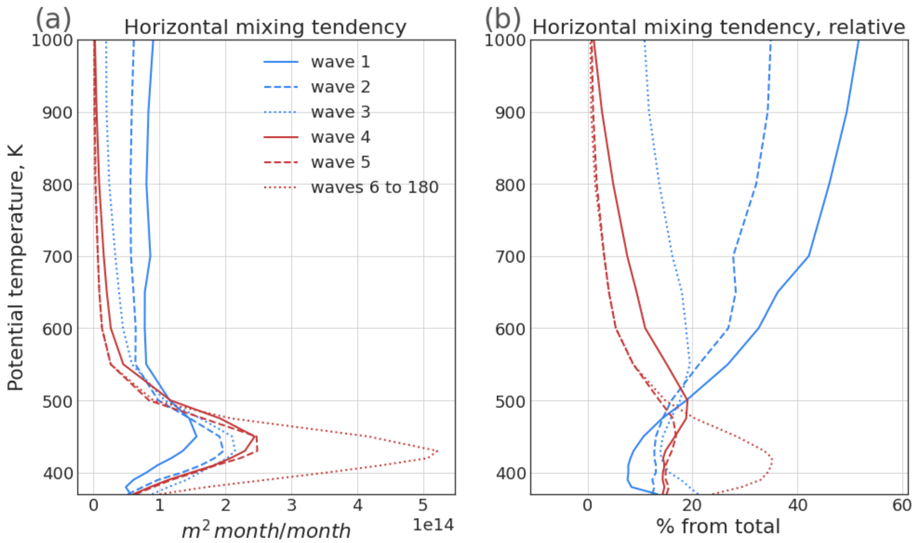

Figure 5.6: Panel (a) integrated (over lat, lon) horizontal mixing tendencies driven by different waves (colors, line styles), and panel (b) relative contribution of different waves to the horizontal mixing tendencies (colors line styles). The figure is based on mean 1980–2017 ERA5 driven CLaMS data.

Vertical profiles of the integrated mixing tendencies for different wave bands and reanalyses are presented in Fig. 5.7. The total isentropic mixing tendencies derived from different reanalyses (shown in panel (a) of the figure) exhibit substantial differences of up to about 50% between different reanalyses at some levels. However, the relative contributions of planetary and smaller-scale waves to the mixing remain remarkably consistent across datasets and are especially similar to each other in the lower stratosphere. Regardless of the reanalysis, isentropic mixing in the middle and upper stratosphere is mostly driven by planetary waves. In the lower stratosphere, on the other hand, mixing is predominantly related to smaller-scale waves.

The level separating the two dynamical regimes where isentropic mixing is primarily driven by planetary waves above and by smaller-scale waves below emerges very consistently for the different reanalyses. This consistency suggests that the level represents a natural dynamical boundary distinguishing different dynamical regimes where mixing processes are predominantly associated with planetary and smaller-scale waves, respectively. Based on this consistency, this separation level between different mixing regimes is defined as the level above which the planetary waves 1–3 dominate the isentropic mixing. At this point, the question arises as to how closely this level is related to the separation level between shallow and deep branches in the residual mean circulation.

The seasonal variation of the separation level between planetary and smaller-scale wave-driven isentropic mixing is presented in Fig. 5.8. This seasonal variability exhibits a robust semi-annual seasonal cycle. The climatological height of this separation level reaches its primary maximum between March and May, with a secondary maximum observed from August to October. Conversely, the level descends during June, July, and from November to February. This seasonal pattern is likely linked to the seasonal variations in the breaking activity of planetary and smaller-scale waves in the stratosphere. During the winter months in each hemisphere, increased Rossby wave dissipation (see eg. Hitchman and Huesmann, 2007) appears to shift the separation level downward. In contrast, during spring and autumn when planetary wave dissipation is reduced the separation level shifts upward. The maximum height observed in March to May coincides with the period of minimal planetary wave dissipation and elevated contributions from smaller-scale waves.

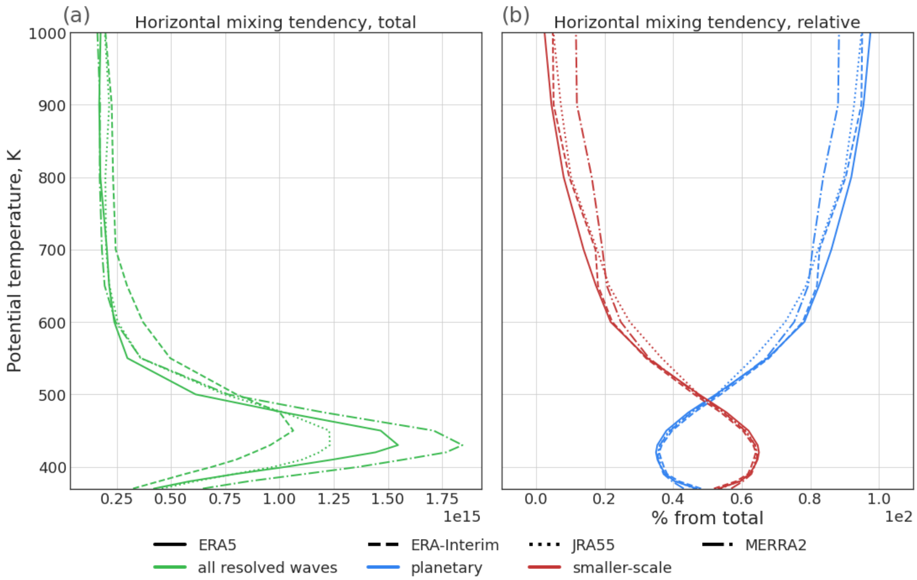

Figure 5.7: Panel (a) integrated (over lat, lon) horizontal mixing tendencies driven by different reanalyses (line styles), and panel (b) relative contribution of planetary and smaller-scale waves to the horizontal mixing tendencies for different reanalyses (colors line styles). The figure is based on mean 1980–2017 reanalyses driven CLaMS data.

It should be noted that the altitude given on the right side of Fig. 5.8 is an approximation of log-pressure altitude, derived from the mean pressure at each isentropic level. As such, it does not precisely represent physical or exact log-pressure altitude and is provided solely to offer a qualitative reference, particularly to aid approximate comparison with the separation level of the overturning circulation. The climatological mean values of the separation level vary slightly across reanalyses: 499 K for ERA5, 494 K for ERA-Interim, 502 K for JRA55, and 497 K for MERRA2. Interestingly, in contrast to the separation level associated with the overturning circulation, the separation level based on isentropic mixing is significantly more consistent across the reanalyses, and the seasonal cycle is significantly more pronounced.

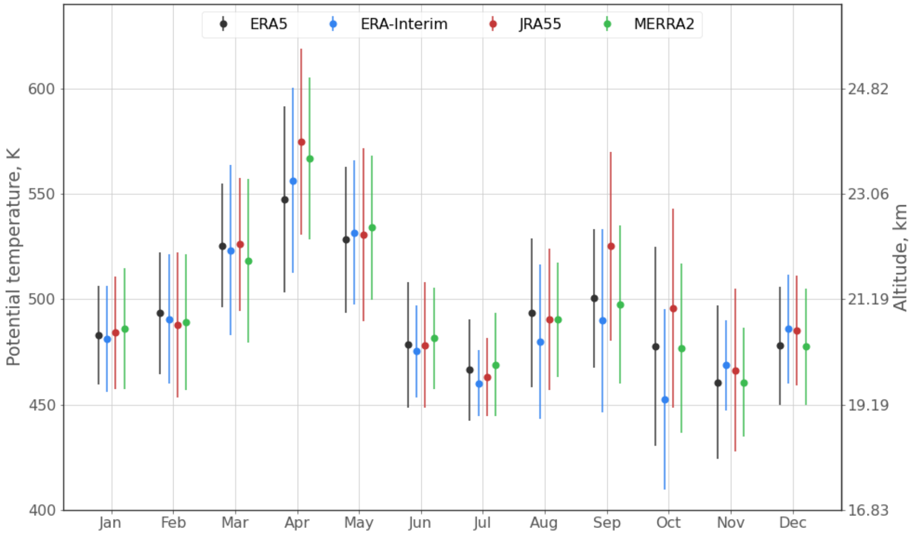

Figure 5.8: Climatological seasonality of isentropic mixing based separation level for different reanalyses (colors). Dots represent median value and lines show standard deviation. The figure is based on mean 1980–2017 reanalyses driven CLaMS data.

5.3 Trends and variability

Vertical profiles of the mean amplitudes of the seasonal cycle and inter-annual variability of the isentropic mixing tendency derived from AoA are presented in Fig. 5.9. These variability profiles are primarily shaped by smaller-scale waves in the lower stratosphere and by planetary waves in the middle and upper stratosphere. Hence, also mixing variability on different time scales (here seasonal and inter-annual) reflects the fact that mixing is related to different dynamical regimes: smaller-scale waves at lower levels below about 500K, planetary waves above.

These variability profiles are affected by the vertical distribution of horizontal AoA gradients (see Fig. 2.3). As a result, the profiles in all four reanalyses exhibit a pronounced peak in the lower stratosphere. The pronounced peak is a common feature in both the inter-annual variability and the mean amplitude of the seasonal cycle of the isentropic mixing. This peak is particularly strong in the MERRA2 reanalysis; ERA5 exhibits a slightly weaker peak, while ERA-Interim and JRA55 show the weakest peak magnitude. Interestingly, there appears to be an inverse relationship between the strength of the peak and the variability above it: reanalyses with a stronger peak in the lower stratosphere tend to exhibit reduced variability in the middle and upper stratosphere. This may indicate dissimilar representations of wave dissipation and horizontal AoA gradients across the reanalyses.

Figure 5.10 shows multi-decadal trends of the isentropic mixing strength, measured as the isentropic mixing tendency for mean age. These trends are markedly stronger and more statistically significant than those observed for upwelling and outflow associated with the residual circulation (cf. Figs. 4.9 and 4.10). Across all four reanalyses, isentropic mixing trends in the lower stratosphere are predominantly influenced by smaller-scale waves, while planetary waves dominate the trends in the middle and upper stratosphere.

In all four reanalyses (although somewhat less pronounced in JRA55) the trends become increasingly positive with altitude in the range between approximately 430 K and 600 K, crossing zero near the 500 K separation level. This shift in trends with altitude is characterized by predominantly negative trends below the separation level, which are mainly influenced by smaller-scale waves. Above the separation level, the trends become mostly positive, driven primarily by planetary wave–induced mixing, further supporting the concept of distinct dynamical regimes operating below and above the 500 K level.

At upper levels, above approximately 800 K, the uncertainties between reanalyses become substantial. The two ECMWF reanalyses exhibit negative mixing trends above this level, whereas the two reanalyses from other centers show mostly positive trends. Interestingly, the trends in mixing driven by smaller-scale waves show better agreement across reanalyses than those associated with planetary waves.

In some cases, e.g. for ERA-Interim around 600K, the trends reach 15% per decade, implying a change in the strength of isentropic mixing by approximately 50% over the period from 1980 to 2017. Whether such a substantial shift in isentropic mixing is related to decadal variability or just an artifact of the respective reanalysis lies beyond the scope of this study, but clearly highlights the need for deeper investigations in the future.

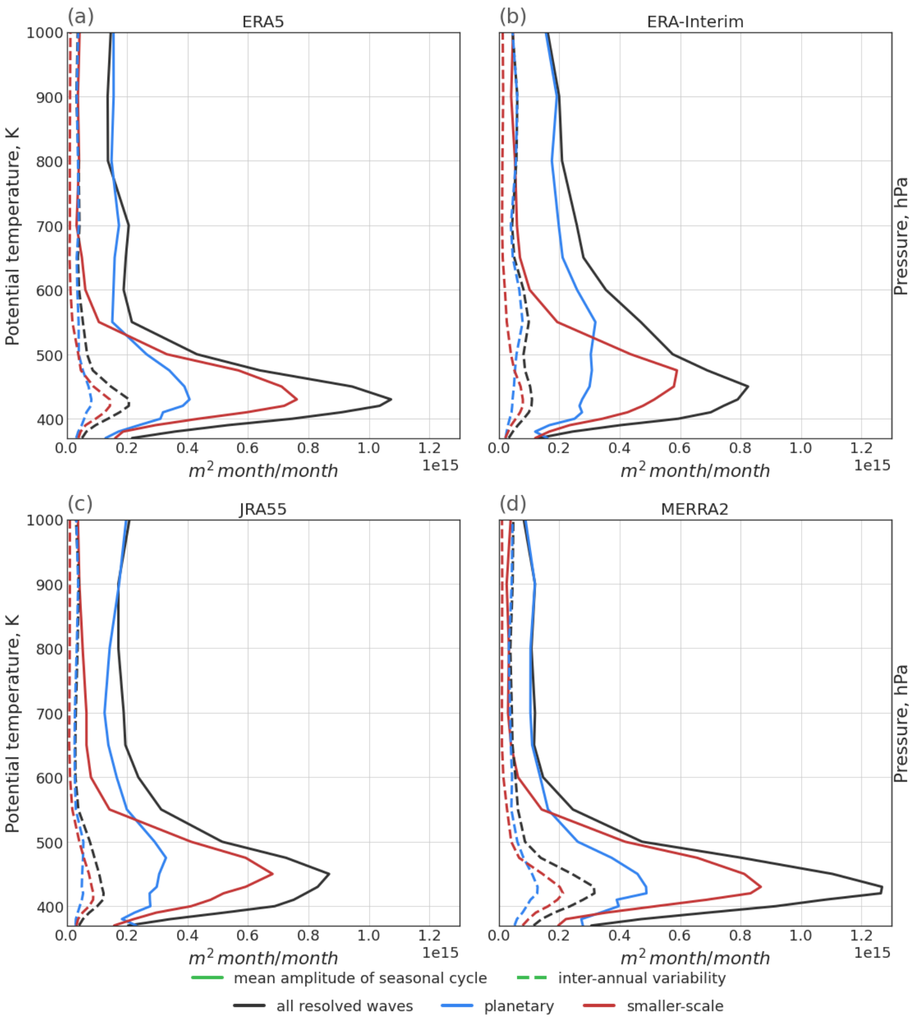

Figure 5.9: Vertical profiles of variability of the isentropic mixing integrated over the tropics (see text for details) and driven by all resolved waves (black), planetary (blue), and smaller-scale (red) waves. Solid lines represent mean amplitude of seasonal cycle and dashed lines represent inter-annual variability. The profiles were constructed from 1980–2017 annual mean data of ERA5 (a), ERA-Interim (b), JRA55 (c), and MERRA2 (d).

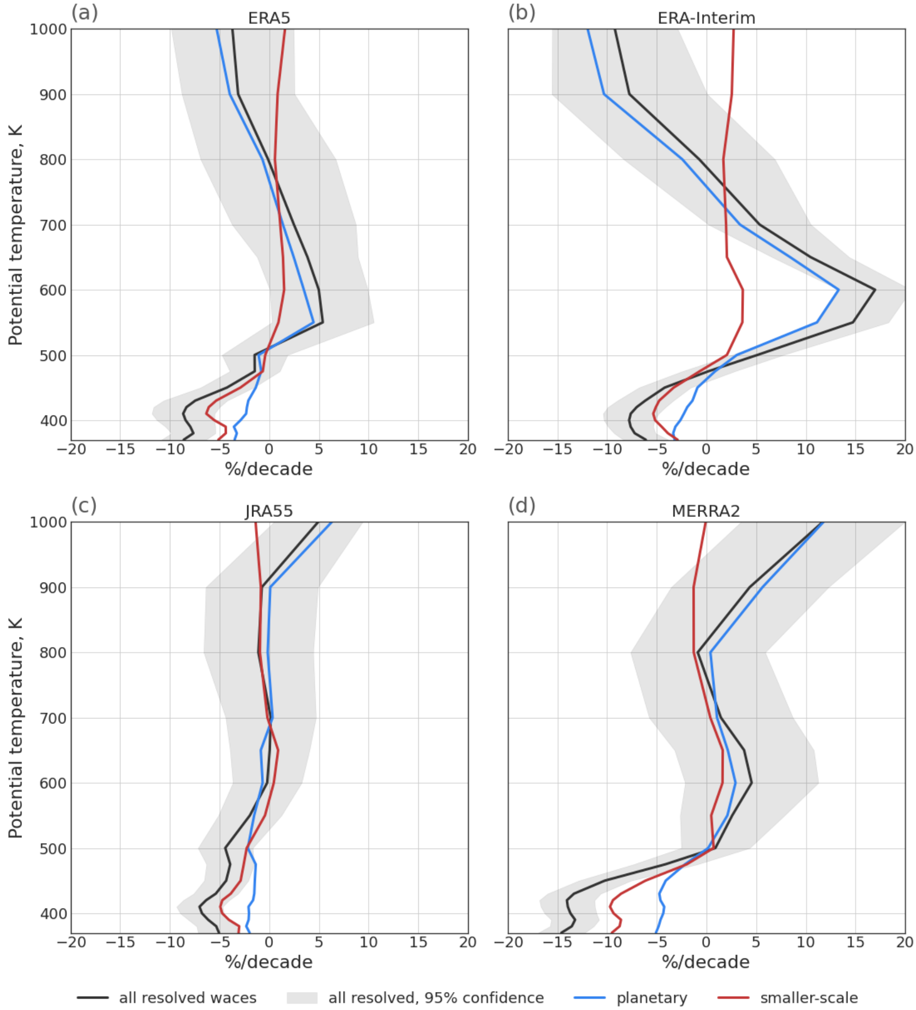

Figure 5.10: Vertical profiles of isentropic mixing trends driven by all resolved waves (black), planetary (blue), and smaller-scale (red) waves, gray shading denotes 95 percent confidence interval for all resolved waves. The profiles were constructed from CLaMS results driven by 1980–2017 annual mean data of ERA5 (a), ERA-Interim (b), JRA55 (c), and MERRA2 (d).

5.4 Tracer sensitivity

By definition, isentropic eddy mixing is influenced by the respective tracer gradients (see Eq. 5.4). To assess the tracer sensitivity of the isentropic mixing results, additional calculations were performed using nitrous oxide (N_2O) as an alternative tracer compared to mean age. Nitrous oxide is a long-lived tracer with atmospheric lifetime close to 115 years (Prather et al., 2015). However, unlike AoA, N_2O is affected by chemical processes in the stratosphere. The CLaMS setup to calculate the distribution of N_2O is similar to the one described in (Pommrich et al., 2014). In this setup chemical sinks of N_2O in the stratosphere are the parameterized reactions with oxygen and photolysis.

$$\mathrm{N_2O + O(^1D)} \longrightarrow \mathrm{products} \tag{5.9}$$

$$\mathrm{N_2O} + hv \longrightarrow \mathrm{products} \tag{5.10}$$

The reaction with oxygen uses updated rate constant recommended by the Jet Propulsion Laboratory (JPL) (Burkholder et al., 2020). The photolysis rate is calculated as described by Becker et al. (2000).

Boundary conditions of N_2O are set as mixing ratios in the lowest (surface) and highest ($\theta = 2500$ K) model levels. The in-situ measurements from NOAA operated CATS (chromatograph for atmospheric trace species) instruments (NOAA, 2025) are used at the lower boundary. The climatology from NASA's HALOE (Halogen Occultation Experiment) instrument (Russell et al., 1993) is used at the upper boundary. CLaMS simulations based on this setup have shown very good agreement between simulated N_2O anomaly patterns and MLS observations (see Pommrich et al., 2014).

In contrast to AoA, which increases with altitude and latitude, N_2O exhibits an inverse distribution, with maximum concentrations at the surface and a minimum in the extratropical upper stratosphere (see Fig. 5.11). Moreover, the vertical and horizontal gradients of N_2O are more uniformly distributed throughout the stratosphere, offering a useful contrast for evaluating the robustness of the diagnosed mixing tendencies, when compared to age of air.

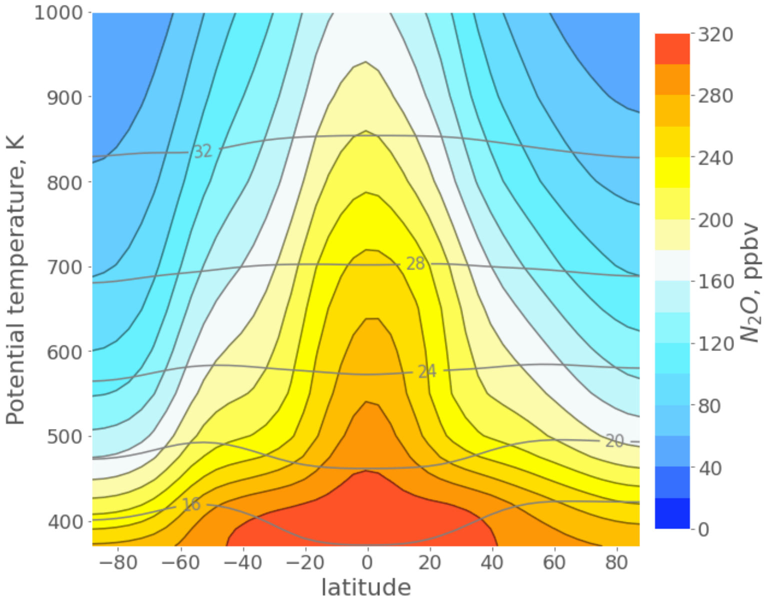

Figure 5.11: Climatological distribution of N_2O in stratosphere. The figure is based on mean 1980–2017 ERA5 driven CLaMS output.

Figure 5.12 presents the contributions of the residual circulation and eddy mixing tendencies to the N_2O tendency budget. Interestingly, the turnaround latitudes do not align as well with the sign reversal of N_2O mixing tendencies as they do with those of AoA. While there is still evidence for enhanced mixing in the lower stratosphere, the mixing tendencies no longer exhibit a clear weakening with altitude as found for age of air. This is likely due to the more uniform vertical distribution of the horizontal N_2O gradient, which stays more pronounced at upper levels compared to that of AoA. Similar to the AoA budget, the residual circulation and mixing tendencies largely oppose each other. However, due to the inverse distribution of N_2O, the mixing tendency now exhibits a negative sign in the tropics, while the circulation tendency is predominantly positive in the tropics. Therefore, to derive the vertical profiles of isentropic mixing for N_2O, the integration is done over regions in the tropics with negative mixing tendencies instead of positive ones.

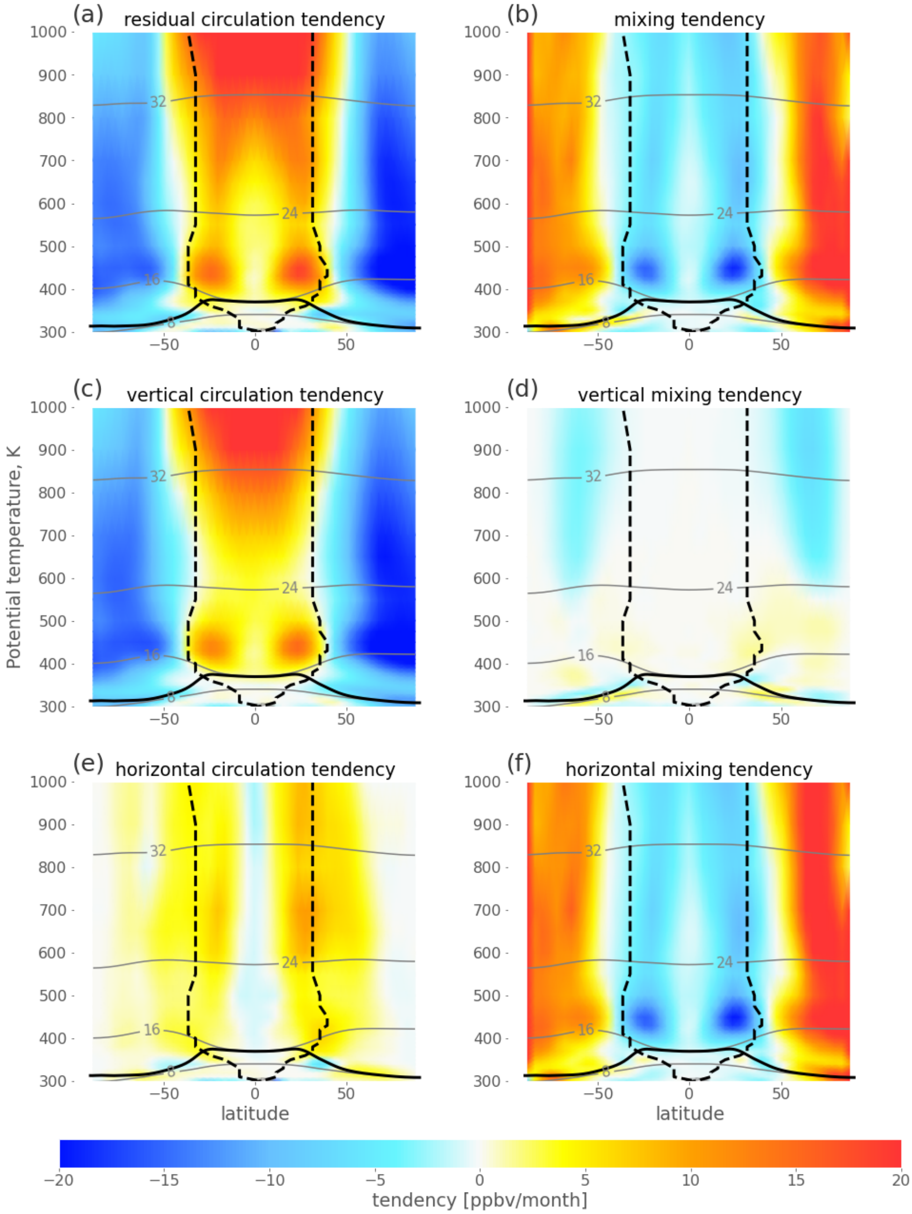

Figure 5.12: Contributions of residual circulation (left) and eddy mixing (right) to the N_2O tendency budget derived from transport equation Eq. 5.4 and using N_2O as a tracer. The (a, b) full tendencies, (c, d) their vertical components, and (e, f) their horizontal components, altitude levels are shown as gray lines, and TAL are represented by black dashed lines. The figure is based on mean 1980–2017 ERA5 driven CLaMS output.

While the differences between AoA and N_2O gradients cause the vertical profiles of horizontal mixing tendencies to switch sign from positive to negative, the relative contributions of each wave to the total mixing tendency remain largely unaffected by the change of tracer (see Fig. 5.13). Overall, the separation between planetary wave-dominated mixing in the middle and upper stratosphere and smaller-scale wave-dominated mixing in the lower stratosphere holds also for isentropic mixing tendencies calculated for N_2O, and with planetary waves defined as wavenumbers 1–3 and smaller-scale waves as those with wavenumbers greater than 3.

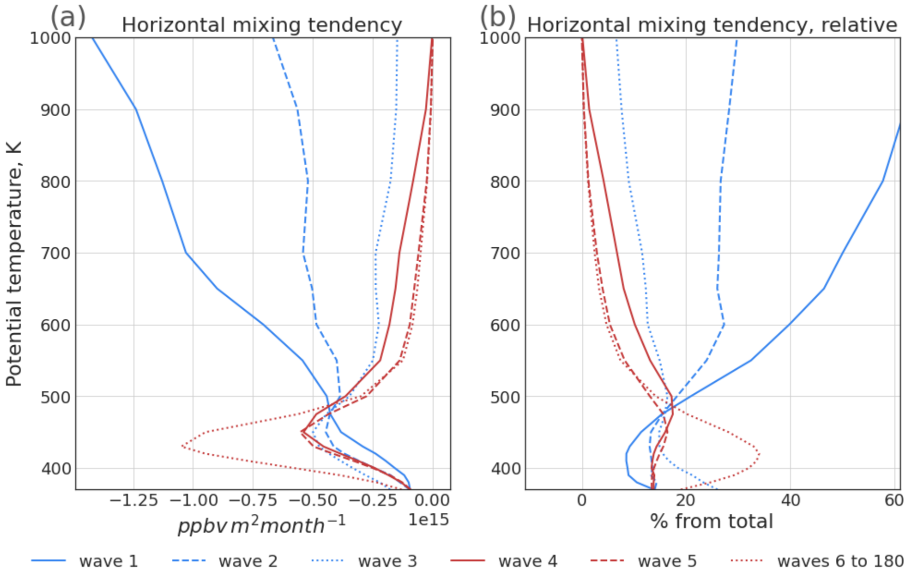

Figure 5.13: Panel (a) integrated (over lat, lon) horizontal mixing tendencies driven by different waves (colors, line styles), and panel (b) relative contribution of different waves to the horizontal mixing tendencies of N_2O (colors line styles). The figure is based on mean 1980–2017 ERA5 driven CLaMS data.

Figure 5.14 presents vertical profiles of the N_2O isentropic mixing tendency integrated over the tropics (latitudes of negative mixing tendencies) for different wave bands and all four reanalyses. Overall, the N_2O–based mixing tendency profiles are very similar to the age of air–based profiles, in particular regarding the relative contributions from planetary and smaller-scale waves to the mixing tendency. Compared to age, for N_2O the agreement between reanalyses becomes slightly weaker in the lower stratosphere. However, the separation level above which isentropic mixing is primarily driven by planetary waves and below which it is dominated by smaller-scale waves is largely unaffected by the change of tracer and emerges consistently across all four reanalyses.

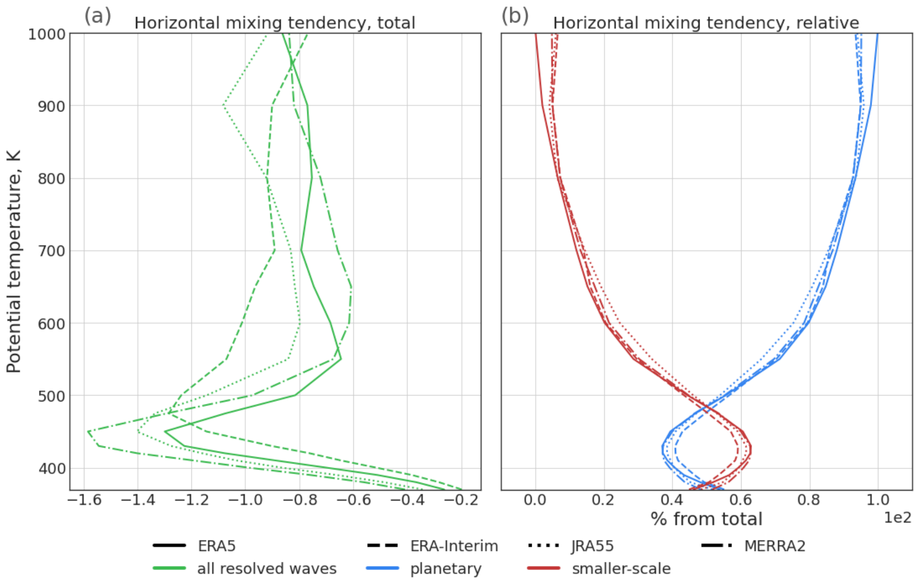

Figure 5.14: Panel (a) integrated (over lat, lon) horizontal mixing tendencies of N_2O driven by different reanalyses (line styles), and panel (b) relative contribution of planetary and smaller-scale waves to the horizontal mixing tendencies for different reanalyses (colors line styles). The figure is based on mean 1980–2017 reanalyses driven CLaMS data.

Furthermore, the seasonal cycle of the N_2O–based isentropic mixing separation level (Fig. 5.15) closely mirrors that obtained using AoA as the tracer (compare Fig. 5.8). This similarity is robust across all four reanalyses. As further shown in Fig. 5.15, the two peaks in the separation level height coincide with periods of minimal planetary wave dissipation in the stratosphere. Conversely, the minima in the separation level height occur during winter in either hemisphere, aligning with enhanced planetary wave dissipation. Changing the tracer from AoA to N_2O for calculating mixing tendencies results in a slightly lower height of the climatological mean separation level: 493 K for ERA5, 486 K for ERA-Interim, 498 K for JRA55, and 493 K for MERRA2.

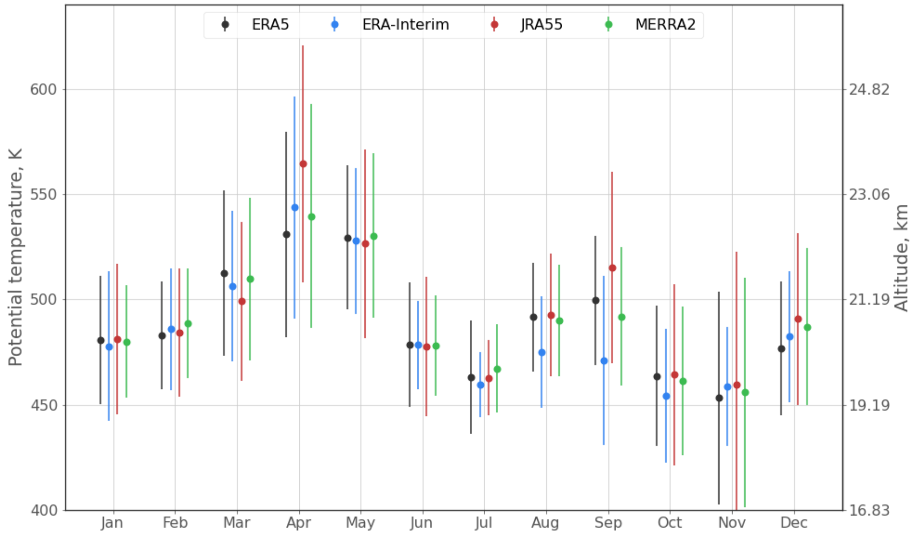

Figure 5.15: Climatological seasonality of N_2O isentropic mixing based separation level for different reanalyses (colors). Dots represent median value and lines show standard deviation. The figure is based on mean 1980–2017 reanalyses driven CLaMS data.

Vertical profiles of the mean amplitude of the seasonal cycle and inter-annual variability of isentropic mixing, derived using N_2O as a tracer, are shown in Fig. 5.16. Again, these profiles are primarily influenced by smaller-scale waves in the lower stratosphere and planetary waves in the middle and upper stratosphere. However, the vertical distribution of horizontal N_2O gradients is much more uniform with altitude compared to that of AoA. As a result, the pronounced peak in the lower stratosphere remains only for the smaller-scale waves.

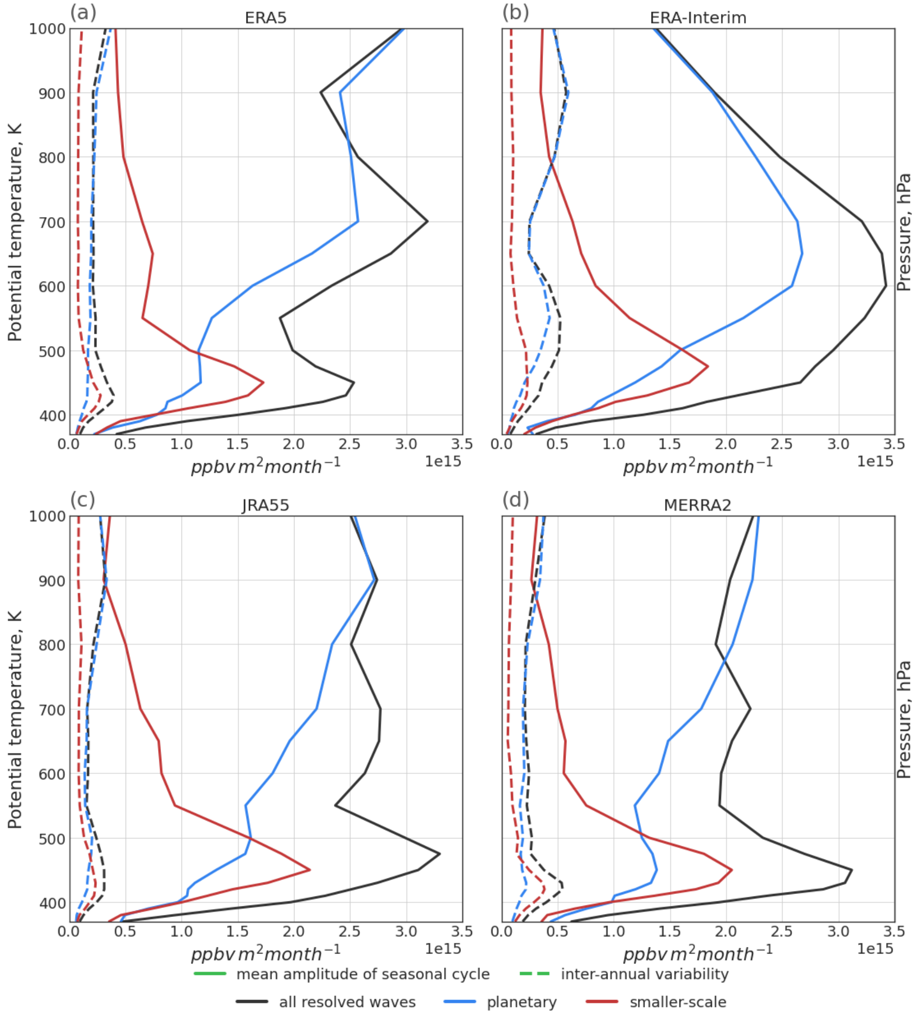

Figure 5.16: Vertical profiles of N_2O variability of the isentropic mixing integrated over the tropics (see text for details) and driven by all resolved waves (black), planetary (blue), and smaller-scale (red) waves, solid lines represent mean amplitude of seasonal cycle and dashed lines represent inter-annual variability. The profiles were constructed from 1980–2017 annual mean data of ERA5 (a), ERA-Interim (b), JRA55 (c), and MERRA2 (d).

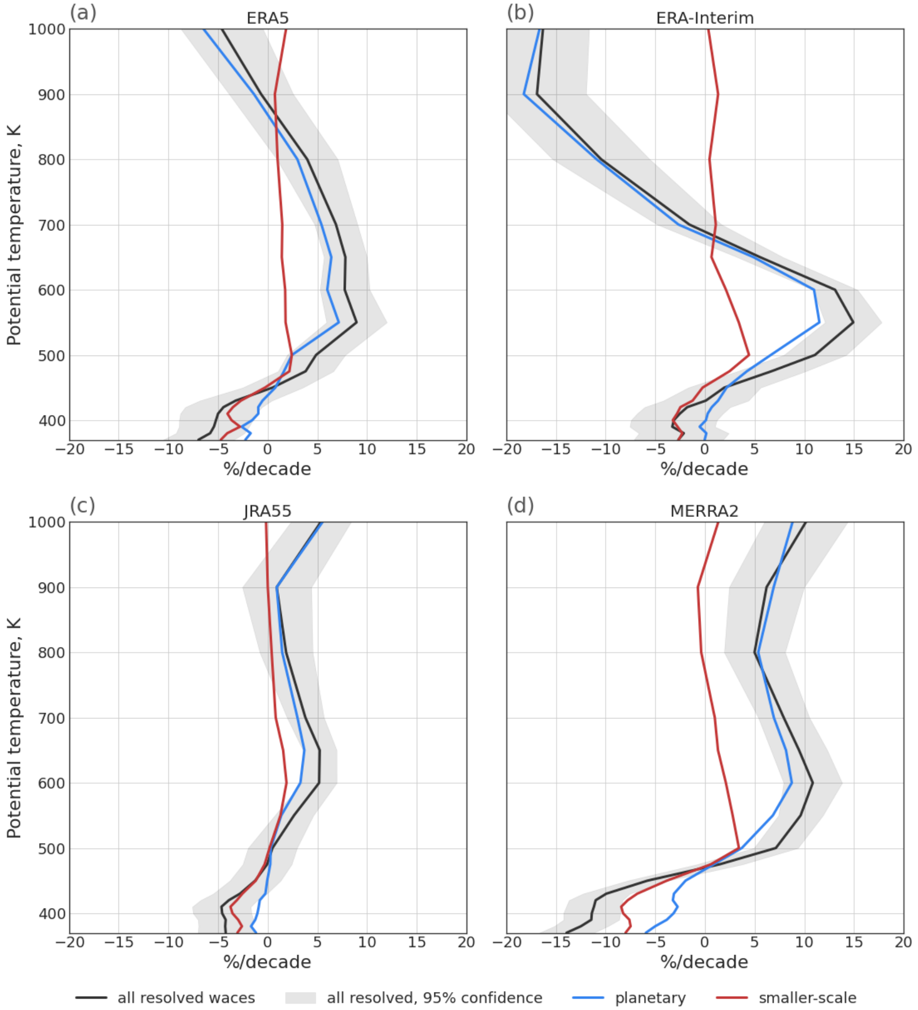

Figure 5.17: Vertical profiles of N_2O isentropic mixing trends driven by all resolved waves (black), planetary waves (blue), and smaller-scale waves (red). Gray shading indicates the 95% confidence interval for the total (all resolved waves) trend. The signs of the profiles have been reversed so that positive values indicate a strengthening of isentropic mixing. The profiles are based on annual mean CLaMS data for 1980–2017 driven by ERA5 (a), ERA-Interim (b), JRA55 (c), and MERRA2 (d).

Figure 5.17 presents the multi-decadal trends of isentropic mixing estimated from N_2O mixing tendencies. These trends are similar to those derived based on AoA. Across all four reanalyses, mixing trends in the lower stratosphere are again primarily influenced by smaller-scale waves, while planetary waves dominate the trends in the middle and upper stratosphere. Note that the signs for N_2O-based mixing trends have been flipped to ensure direct comparability with age of air–based trends. Weakening mixing trends in the lower stratosphere are still evident and are statistically significant in all reanalyses except ERA-Interim. A notable new feature is the emergence of statistically significant positive trends around the 600 K isentropic level, consistently observed across all four reanalyses. These positive trends suggest a strengthening of isentropic mixing within the tropical pipe region of the stratosphere.

In summary, the comparison between age of air and N_2O–based mixing tendencies shows that most of the key findings, such as the wave-based separation and the seasonality of the separation level, are found to be largely independent of the choice of tracer. The observed differences are likely related to the different spatial gradients of N_2O and AoA.

5.5 Discussion and summary

The concept of stratospheric tracer transport consisting of net transport along the residual circulation and modifications by isentropic mixing is commonly used in stratospheric research (e.g. Rosenlof et al., 1997; Plumb, 2002). It was also shown that acceleration of the residual circulation and changes in the aging by mixing (first and second terms on the right-hand side of Eq. 2.2, respectively) contribute almost equally to the simulated decrease of AoA in chemistry climate models (Garny et al., 2014). Here, horizontal mixing tendency is used as a straightforward estimate of isentropic mixing. The mixing tendency was calculated for two tracers with winds from four global reanalyses using the Lagrangian chemistry transport model CLaMS. Furthermore, the wave forcing of the mixing is investigated in terms of wave scale.

Using Fourier decomposition, it was established in the previous chapter that the deep branch of the BDC is primarily driven by planetary waves (wavenumbers 1 to 3) which break in the middle and upper stratosphere, while the shallow branch is more strongly driven by smaller-scale waves (wavenumbers greater than 3) which break in the lower stratosphere. Analysis of the resolved wave drag in this chapter has shown that the characteristics of isentropic mixing are similarly related to differences in the dynamical regimes. In the deep branch region, the mixing is largely driven by planetary waves with wavenumbers 1–3. In the shallow branch region, the isentropic mixing is mainly driven by smaller-scale waves (wavenumbers greater than 3). The wave drag-based separation of the isentropic mixing is robust across both tracers considered (mean age, N_2O) and all four reanalyses used in this study.

In all evaluated cases (two tracers, four reanalyses) the mean level separating the mixing primarily driven by planetary waves and that mainly driven by smaller-scale waves is close to 500 K (about 50 hPa). Interestingly, this separation level was found to have more pronounced seasonality and to be more consistent across the reanalyses than the separation level between the deep and shallow branch of the residual circulation. The seasonality seems to follow the seasonality of planetary wave dissipation in the stratosphere and, to a lesser extent, the seasonality of the smaller-scale waves.

Trends in the isentropic mixing estimated in this chapter are generally stronger and more statistically significant than trends of the overturning circulation. In some cases, trends in isentropic mixing reach 15% per decade. These strong trends are likely influenced by the fact that isentropic mixing, as evaluated in this work, reflects both diffusivity and the horizontal gradients of the tracer. To assess the role of tracer gradients, the calculations were repeated using a second tracer with a distinct spatial distribution. Switching from AoA, which exhibits strong horizontal gradients in the lower stratosphere and weaker ones above, to N_2O, which has a more vertically uniform distribution of horizontal gradients, results in weaker negative trends in the lower stratosphere and stronger positive trends at altitudes around 600 K. This difference suggests that changes in tracer gradients significantly contribute to the observed trends in isentropic mixing. Isolating the effects of changes in diffusivity remains an important direction for future research. The most persistent feature found here is a negative trend in the lower stratosphere, below approximately 500 K. A similar negative trend in this region was previously reported for effective diffusivity in ERA-Interim data for the period 1980–2002 (Abalos et al., 2016).

It should also be noted that, here, like in the previous chapter, a scale-based separation of atmospheric waves is used. An additional incorporation of a more physically based separation of wave types, in particular of the intermediate waves (here wavenumbers 3 and 4), would be a valuable direction for future research.

Chapter 6

Summary and conclusions

Based on both a statistical and a mechanistic analysis, we propose here a dynamical separation of the deep and shallow branches in terms of the dynamical characteristics of the stratospheric circulation. The deep branch of the BDC is mainly driven by large-scale planetary waves with wavenumbers 1 to 3, while the shallow branch is driven by smaller-scale waves with wavenumbers greater than 3. The mean altitude of the level separating the deep and shallow branch is at about 22 km (45 hPa) with significant inter-annual and seasonal variations. In particular, the separation level height shows a weak semi-annual cycle in all four reanalyses used in this work. The dynamical separation criterion found in this work is observed to be robust across all four reanalyses.

At the tropical tropopause, both wave types (planetary and smaller-scale) contribute comparably to the upwelling and both branches of the overturning circulation move a similar amount of mass. ERA5 reanalysis shows the strongest contribution from smaller-scale waves to the driving of the BDC while for the other three reanalyses the contribution from smaller-scale waves is somewhat weaker. While the variability of the deep branch is mostly controlled by planetary waves, both planetary and smaller-scale waves affect the variability of the shallow branch to a similar extent.

The circulation trends over the period 1980–2017 estimated here for the different reanalyses were found to be statistically insignificant. Furthermore, dividing the period into ozone depletion and ozone recovery phases did not notably enhance the statistical significance of the trends. However, some of the trend features similarly emerged for all four reanalyses considered. The robust features concern a strengthening of the circulation's tropical outflow at altitudes of about 35–40 km and a weakening below, potentially indicating an upward shift of the deep circulation branch. At lower levels just above the tropical tropopause, a strengthening of tropical outflow related to the shallow branch emerged robustly for the different reanalyses.

Similarly to the stratospheric residual circulation, stratospheric isentropic mixing can also be vertically separated into two regimes. In the upper regime, located deeper in the stratosphere, mixing is predominantly driven by planetary waves (wavenumbers 1 to 3), while the lower stratospheric regime is mainly influenced by smaller-scale waves (with wavenumbers higher than 3). Importantly, this separation criterion is found to be robust across all four reanalyses. The mean altitude of this isentropic mixing separation level is close to 500 K (50 hPa), exhibiting notable inter-annual and seasonal variability. In particular, the height of the separation level follows a semi-annual cycle, reaching maximum altitudes during periods of reduced planetary wave dissipation.

Compared to the overturning circulation, the trends in isentropic mixing over the 1980–2017 period are substantially stronger and more statistically significant. Those significant trends have opposite signs below and slightly above the separation level, indicating a major shift in the strength of stratospheric mixing. A consistent feature across all reanalyses is the weakening of isentropic mixing in the lower stratosphere.

Although changing the tracer from AoA to N_2O significantly affected the vertical distribution of isentropic mixing strength, the core conclusions of the analysis remained robust. Specifically, the separation between the dominant wave regimes of the lower stratosphere and above it was preserved. Furthermore, while the separation level calculated with N_2O is slightly lower, its seasonal cycle remains highly comparable. Notably, using N_2O as the tracer also revealed an additional robust trend: a strengthening of isentropic mixing within the tropical pipe region.

Given the differences between reanalyses regarding the climatological height, variability, and trends of the separation level, a precise identification of this level is needed for detailed investigations of the stratospheric circulation. In particular, calculating the specific separation level for a given reanalysis or model dataset, such as by using the wave drag approach proposed in this study, appears to be advantageous for model inter-comparisons. Otherwise, we recommend using the separation level calculated here from ERA5, given the ability of that reanalysis to better represent effects of small-scale waves compared to the older reanalyses.

It should also be noted that the 70 hPa level, which is often used as a reference level for model inter-comparisons of stratospheric tropical upwelling, is not unambiguously related to a distinct circulation branch but is indeed affected by both the deep and the shallow branch. As shown here, the separation level between these circulation branches may significantly differ between different models, and so may the effects of the deep and shallow branch on upwelling across 70 hPa. Using the appropriate separation levels for distinguishing the deep and shallow branch in model and reanalysis inter-comparisons could reduce the spread between models regarding climatology and trends in the stratospheric circulation.

Appendix A

Auxiliary figures

This appendix contains auxiliary figures that provide more information about the contribution of individual zonal wavenumbers (Fig. A.1), upwelling deficit and comparison between different reanalyses with ERA5 as a reference (Figs. A.2, A.3), and a comparison between full resolution ERA5 data and ERA5 data downsampled to resolutions of 1°spatially and 6 hours in time (Figs. A.4, A.5).

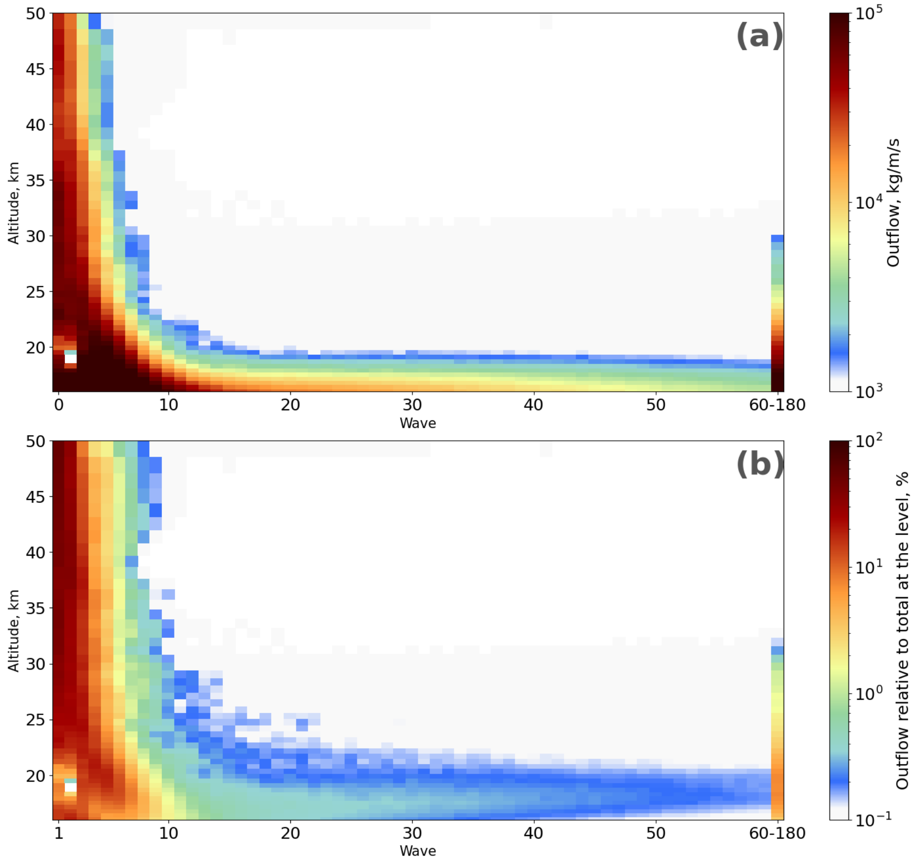

Figure A.1: (a) 1980–2017 mean vertical profiles of DWCP outflow estimated for different waves from $\nabla \cdot F$ calculations based on ERA5 data. (b) As in (a) but showing the relative contribution (%) of each wave component to the total DWCP outflow at each vertical level.

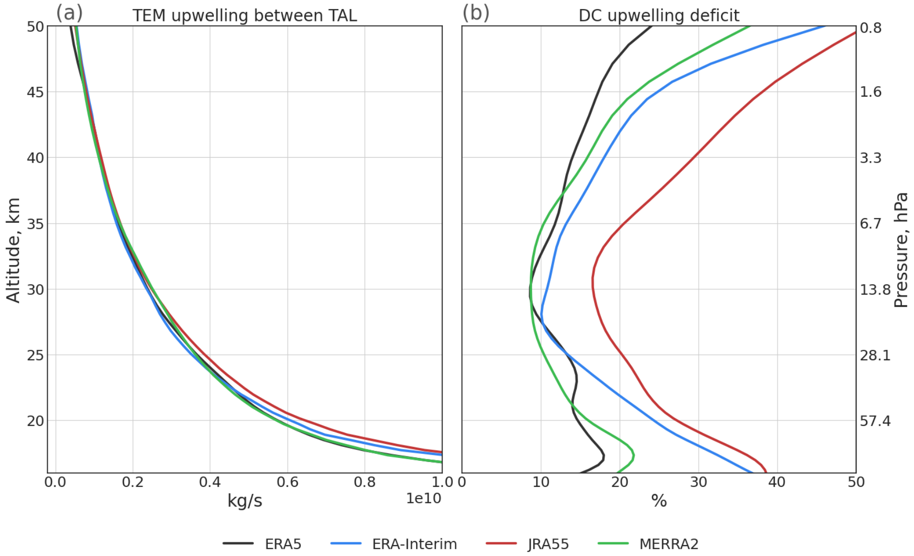

Figure A.2: (a) 1980–2017 mean profiles of TEM upwelling from ERA5 (black), ERA-Interim (blue), JRA55 (red), and MERRA2 (green) reanalyses. (b) The mean upwelling deficit in the downward control calculation (in percent), estimated as the relative difference between TEM and downward control upwelling. This upwelling deficit corresponds to the missing wave drag in the downward calculation (see text). The deficit lines were smoothed with a Gaussian filter. The black line for ERA5 upwelling in (a) in the lower stratosphere mostly overlaps with the green MERRA2 line.

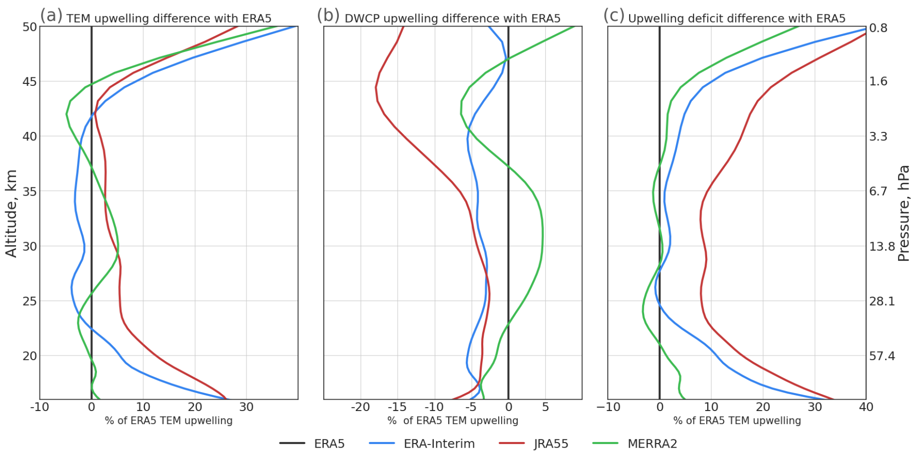

Figure A.3: Reanalyses upwelling inter-comparison with ERA5 as base, for TEM upwelling (a), DWCP upwelling (b), and upwelling deficit (c)

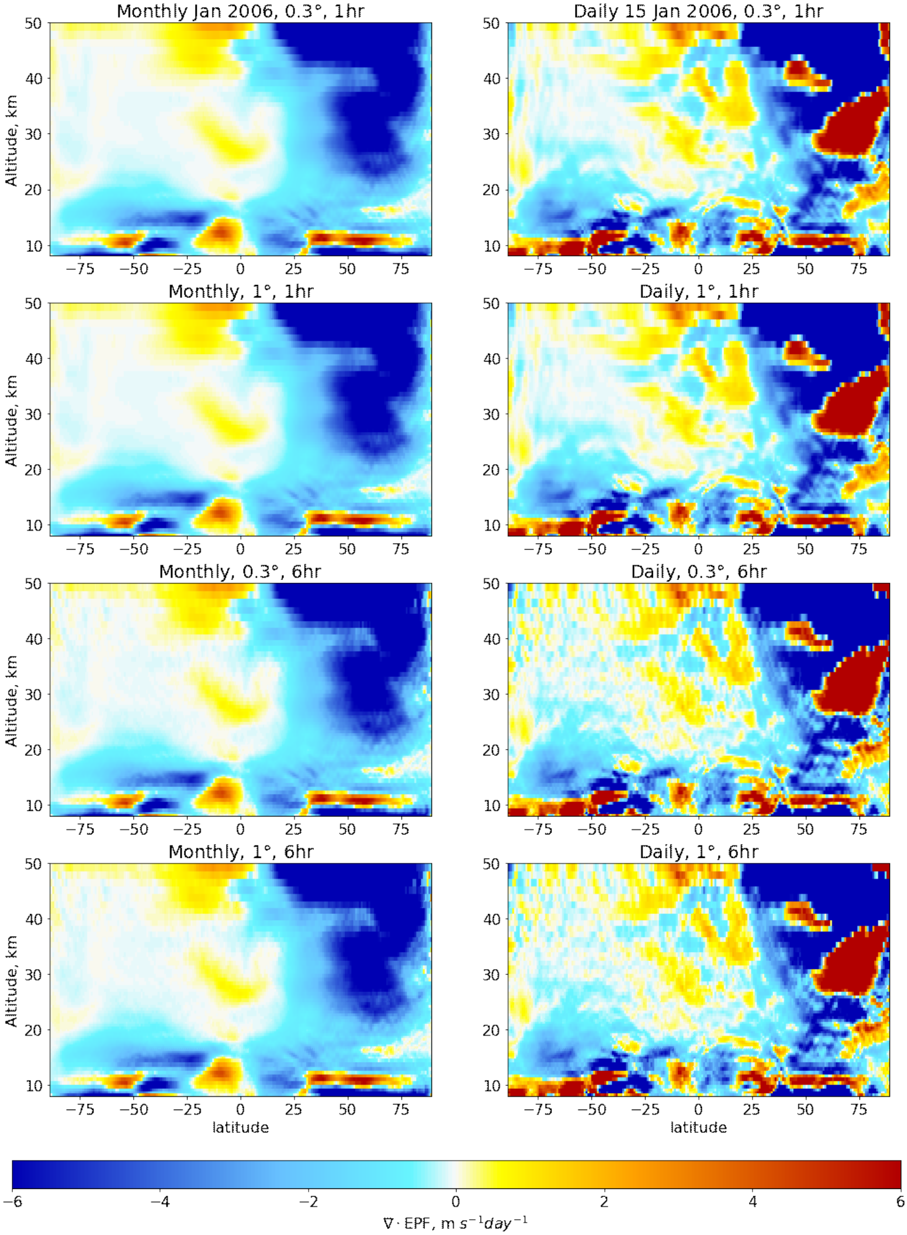

Figure A.4: Effect of reduction of spatial (from 0.3° to 1°) and temporal (from 1 to 6 hours) resolution on $\nabla\cdot$*EPF calculations*

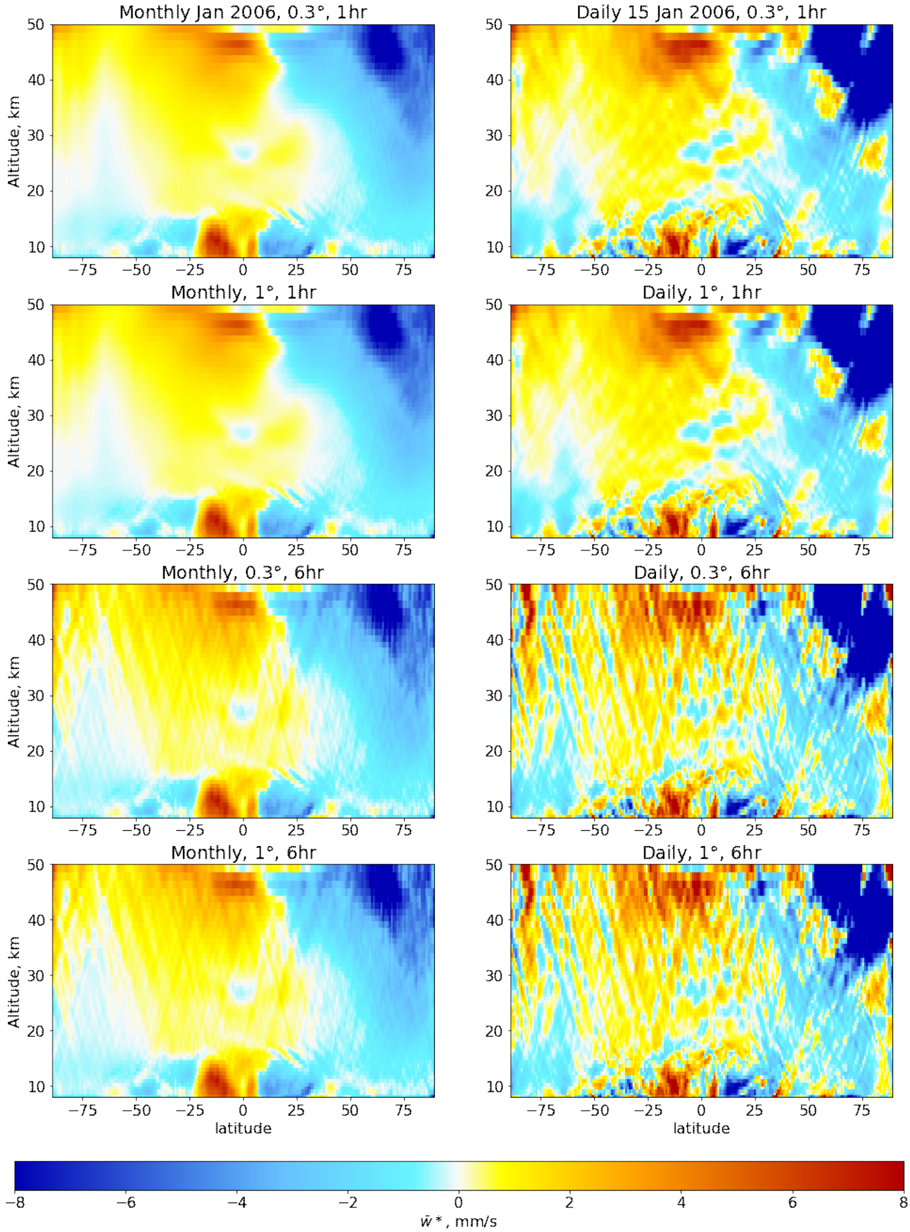

Figure A.5: Effect of reduction of spatial (from 0.3° to 1°) and temporal (from 1 to 6 hours) resolution on $\bar{w}^*$ calculations

Appendix B

Overview of the software package

The scripts used for the upwelling and outflow calculations presented in Chapter 4 and for the isentropic mixing calculations presented in Chapter 5 are available at: `https://github.com/RasulBaikhadzhaev/transformed-eulerian-mean`

The Python script for calculating residual circulation is a command-line tool designed specifically for computing TEM diagnostics from meteorological data. The primary goal is to analyze the interaction between atmospheric waves and the mean flow, which is a fundamental concept in understanding atmospheric circulation. The script is built to be robust and efficient, featuring parallel processing to handle large datasets, flexible configuration options, and the ability to work with various data formats.

The script's main workflow can be broken down into the following steps:

- Configuration: It reads settings from a `config.toml` file and can override them with command-line arguments. This allows users to specify input/output directories, variable names within the data files, and various calculation parameters without modifying the code itself.

- File Handling: It collects a list of input NetCDF files from a specified directory or a text file. It can filter these files based on a date range, specific hours of the day, and can skip files that have already been processed and saved to the output directory. It cleverly extracts date and time information directly from filenames based on a user-defined pattern.

- Data Preparation: For each input file, the script reads the necessary variables (wind components, temperature). A crucial step is ensuring the data is on a consistent vertical coordinate system. It transforms the vertical coordinate to a log-pressure altitude ($z = -H \ln(p/p_0)$), interpolating the data if necessary. This standardization is essential for the TEM calculations.

- TEM Diagnostics Calculation (TEMCalcs function): This is the scientific core of the script. It calculates several key diagnostic quantities:

  - Residual Mean Meridional Circulation: It computes the "transformed" or "residual" mean circulation (VBarStar, WBarStar), which provides a more accurate picture of mass transport in the atmosphere than the standard Eulerian mean.
  - Eliassen-Palm (EP) Flux: It calculates the two-dimensional Eliassen-Palm (EP) flux vector (EPF_vert, EPF_lat). The EP flux represents the propagation of wave activity through the atmosphere.
  - EP Flux Divergence: It computes the divergence of the EP flux (`div_EPF`), which acts as a forcing term on the mean zonal flow. Regions of EP flux convergence indicate that waves are decelerating the mean flow, while divergence indicates acceleration.
  - Eddy Fluxes: It computes the zonal mean eddy fluxes of heat (vPrimeThetaPrimeBar) and momentum (vPrimeUPrimeBar, wPrimeUPrimeBar), which are the building blocks of the TEM diagnostics.

- Fourier Decomposition (Optional): If enabled, the script can perform a Fourier transform on the eddy flux terms. This allows for the decomposition of the EP flux and its divergence by wavenumber, enabling researchers to isolate the impact of different scales of atmospheric waves (e.g., planetary waves 1, 2, 3, etc.).

- Temporal Averaging (Optional): The script can group the input files by day or month and calculate a temporal average of the results before saving. This is useful for creating climatologies or analyzing monthly/daily variations.

- Parallel Processing: The script leverages the multiprocessing library to distribute the calculations across multiple CPU cores. Each core processes a chunk of input files simultaneously, significantly speeding up the analysis of large datasets.

- Output: The final results, including the calculated TEM diagnostics, are saved into new NetCDF files in the specified output directory. The output files are clearly named, often including a prefix and the date of the data.

The core of the script computes key quantities like the residual mean meridional circulation, the EP flux, and its divergence, which are fundamental for understanding how atmospheric waves influence the large-scale circulation. Featuring robust configuration through a `.toml` file and command-line arguments, it offers advanced capabilities like the Fourier decomposition of fluxes to isolate the impact of specific wavenumbers. To handle large datasets, the script is optimized for performance, utilizing parallel processing to distribute the computational workload across multiple CPU cores, making it a powerful and flexible tool for diagnostic studies of the atmosphere.

The Python script for estimating tracer transport is a comprehensive command-line tool designed to diagnose and quantify the transport of chemical tracers in the atmosphere. It calculates the various terms of the tracer transport equation in isentropic coordinates, allowing researchers to understand how a tracer's concentration changes due to large-scale circulation and smaller-scale eddy mixing. The script is highly configurable, supports parallel processing for efficiency, and can handle complex data scenarios where meteorological and tracer data are stored in separate files with different resolutions.

The script's primary purpose is to solve the tracer continuity equation on potential temperature surfaces. This involves breaking down the change in tracer concentration over time into its constituent parts:

- Advection by the Residual Circulation: It calculates how the large-scale, mass-weighted mean flow (vBarStar, qBarStar) moves the tracer horizontally and vertically.

- Eddy Mixing: It quantifies the transport caused by eddies (deviations from the zonal mean), calculating the eddy flux of the tracer and its divergence. This term represents the mixing and stirring effect of atmospheric waves.

- Sinks and Sources: It can incorporate a term for chemical production or loss of the tracer, which can be a constant value or a function of the tracer's concentration (e.g., a half-life).

The final output provides a budget analysis, showing the relative importance of each of these processes in controlling the distribution of a given tracer.

Key Features and Workflow:

- Flexible Configuration: The script is driven by a `.toml` configuration file and can be further customized with command-line arguments. This allows users to specify file paths, variable names, vertical levels, and numerous processing options without altering the source code.

- Advanced Data Handling:

  - Separate Data Sources: The script can ingest meteorological data (winds, pressure, temperature) and tracer data from different files.

  - Temporal Binning: When meteorological data has a higher frequency than the tracer data, the script can intelligently average (bin) the meteorological fields over time to match the tracer's temporal resolution, using customizable weighting schemes.

  - Spatial Interpolation and Binning: It interpolates both meteorological and tracer data onto a common grid defined by potential temperature levels (isentropic coordinates). It can also perform spatial binning (averaging) over latitude and longitude to match resolutions or reduce noise.

- Isentropic Coordinate Calculations (tracerTransport function): This is the scientific core of the script.

  - It calculates the isentropic density (sigmaDensity).

  - It computes the residual mean circulation and eddy fluxes on these isentropic surfaces.
  - It calculates all the tendency terms of the tracer transport equation: meridional and vertical advection, and the divergence of meridional and vertical eddy fluxes.

- Fourier Decomposition (Optional): If enabled, the script can perform a Fourier transform on the eddy flux terms. This allows the user to decompose the eddy transport by wavenumber, making it possible to identify the contribution of different scales of atmospheric waves (e.g., planetary waves vs. synoptic-scale waves) to the overall tracer transport.

- Parallel Processing: The script uses the multiprocessing library to process multiple time steps or files concurrently. This dramatically reduces the runtime when analyzing large datasets spanning many years.

- The script also includes a sophisticated function that matches and groups high-frequency meteorological files with lower-frequency tracer files.

In summary, this Python script is designed to handle complex real-world data scenarios, capable of ingesting meteorological and tracer data from separate files with differing temporal and spatial resolutions. The script intelligently preprocesses the data by performing temporal binning of high-frequency meteorological fields to match tracer data, and interpolates all variables onto a common isentropic and spatial grid. Its core functionality decomposes the change in tracer concentration into contributions from advection by the residual mean circulation and mixing by atmospheric eddies, with an optional capability to perform a Fourier decomposition to analyze the role of specific wave scales in the eddy transport. By leveraging parallel processing for efficiency and offering deep customization through a configuration file, the script serves as a powerful command-line tool for researchers to quantitatively analyze the budget and transport pathways of chemical constituents in the atmosphere.

List of Figures

List of Tables

Bibliography

Abalos, M., Legras, B., Ploeger, F., and Randel, W. J.: Evaluating the advective Brewer-Dobson circulation in three reanalyses for the period 1979-2012, J. Geophys. Res., 120, doi:10.1002/2015JD023 182, 2015.

Abalos, M., Shuckburgh, E., and Legras, B.: Interannual variability in effective diffusivity in the upper troposphere/lower stratosphere from reanalysis data, Q. J. R. Meteorol. Soc., 142, 1847–1861, https://doi.org/10.1002/qj.2779, 2016.

Abalos, M., Polvani, L., Calvo, N., Kinnison, D., Ploeger, F., Randel, W., and Solomon, S.: New Insights on the Impact of Ozone-Depleting Substances on the Brewer-Dobson Circulation, J. Geophys. Res., 124, 2435–2451, https://doi.org/https://doi.org/10.1029/2018JD029301, 2019.

Abalos, M., Calvo, N., Benito-Barca, S., Garny, H., Hardiman, S. C., Lin, P., Andrews, M. B., Butchart, N., Garcia, R., Orbe, C., Saint-Martin, D., Watanabe, S., and Yoshida, K.: The Brewer–Dobson circulation in CMIP6, Atmos. Chem. Phys., 21, 13 571–13 591, https://doi.org/10.5194/acp-21-13571-2021, 2021.

Abalos, M., Randel, W. J., and Garcial, R. R.: The Dominant Role of the Summer Hemisphere in Subtropical Lower Stratospheric Wave Drag Trends, Geophysical Research Letters, 51, https://doi.org/https://doi.org/10.1029/2023GL105827, 2024.

Abdalla, S., Isaksen, L., Janssen, P., and Wedi, N.: Effective spectral resolution of ECMWF atmospheric forecast models, https://doi.org/10.21957/rue4o7ac, 2013.

Andrews, D. G. and McIntyre, M. E.: Planetary waves in horizontal and vertical shear:

The generalized Eliassen-Palm relation and the mean zonal acceleration, J. Atmos. Sci., 33, 2031–2048, 1976.

Andrews, D. G. and McIntyre, M. E.: An exact theory of nonlinear waves on a Lagrangian mean flow, J. Fluid Mech., 89, 609–646, 1978a.

Andrews, D. G. and McIntyre, M. E.: On wave-action and its relatives, J. Fluid Mech., 89, 647–664, 1978b.

Andrews, D. G. and McIntyre, M. E.: Generalized Eliassen–Palm and Charney–Drazin theorems for waves on axisymmetric mean flows in compressible atmospheres, J. Atmos. Sci., 35, 175–185, 1978c.

Andrews, D. G., Holton, J. R., and Leovy, C. B.: Middle Atmosphere Dynamics, Academic Press, San Diego, USA, 1987.

Aristotle and Lee, H. D. P.: Meteorologica / by Aristotle. With an English translation by H.D.P.Lee, Harvard University Press, Cambridge, Massachusetts, USA, 1952.

Assmann, R.: Über die Existenz eines wärmeren Luftstromes in der Höhe von 10 bis 15 km. (On the existence of a warmer airflow at heights from 10 to 15 km), Sitzungsber. K. Preuss. Akad. Wiss., 24, 495–504, 1902.

Baldwin, M. and Dunkerton, T.: Stratospheric harbingers of anomalous weather regimes, Science, 244, 581–584, 2001.

Ball, W. T., Kuchař, A., Rozanov, E. V., Staehelin, J., Tummon, F., Smith, A. K., Sukhodolov, T., Stenke, A., Revell, L., Coulon, A., Schmutz, W., and Peter, T.: An upper-branch Brewer–Dobson circulation index for attribution of stratospheric variability and improved ozone and temperature trend analysis, Atmos. Chem. Phys., 16, 15 485–15 500, https://doi.org/10.5194/acp-16-15485-2016, 2016.

Becker, G., Grooß, J.-U., McKenna, D. S., and Müller, R.: Stratospheric photolysis frequencies: Impact of an improved numerical solution of the radiative transfer equation, J. Atmos. Chem., 37, 217–229, https://doi.org/10.1023/A:1006468926530, 2000.

Birner, T. and Bönisch, H.: Residual circulation trajectories and transit times into the extratropical lowermost stratosphere, Atmos. Chem. Phys., 11, 817–827, https://doi.org/10.5194/acp-11-817-2011, 2011.

Bönisch, H., Engel, A., Curtius, J., Birner, T., and Hoor, P.: Quantifying transport into the lowermost stratosphere using simultaneous in-situ measurements of SF_6 and CO_2, Atmos. Chem. Phys., 9, 5905–5919, 2009.

Bönisch, H., Engel, A., Birner, T., Hoor, P., Tarasick, D. W., and Ray, E. A.: On the structural changes in the Brewer-Dobson circulation after 2000, Atmos. Chem. Phys., 11, 3937–3948, https://doi.org/10.5194/acp-11-3937-2011, 2011.

Brasseur, G. and Solomon, S.: Aeronomy of the Middle Atmosphere: Chemistry and Physics of the Stratosphere and Mesosphere, Springer, Heidelberg, Germany, third edn., 2005.

Brewer, A. W.: Evidence for a world circulation provided by the measurements of helium and water vapour distribution in the stratosphere, Q. J. R. Meteorol. Soc., 75, 351–363, https://doi.org/10.1002/qj.49707532603, 1949.

Burkholder, J., Sander, S., Abbatt, J., Barker, J., Cappa, C., Crounse, J., Dibble, T., Huie, R., Kolb, C., Kurylo, M., Orkin, V., Percival, C., Wilmouth, D., and Wine, P.: Chemical kinetics and photochemical data for use in atmospheric studies; evaluation number 19, https://doi.org/2014/49199, 2020.

Butchart, N.: The Brewer-Dobson circulation, Rev. Geophys., 52, 157–184, https://doi.org/10.1002/2013RG000448, 2014.

Butchart, N., Charlton-Perez, A. J., Cionni, I., Hardiman, S. C., Haynes, P. H., Krueger, K., Kushner, P. J., Newman, P. A., Osprey, S. M., Perlwitz, J., Sigmond, M., Wang, L., Akiyoshi, H., Austin, J., Bekki, S., Baumgaertner, A., Braesicke, P., Bruehl, C., Chipperfield, M., Dameris, M., Dhomse, S., Eyring, V., Garcia, R., Garny, H., Joeckel, P., Lamarque, J.-F., Marchand, M., Michou, M., Morgenstern, O., Nakamura, T., Pawson, S., Plummer, D., Pyle, J., Rozanov, E., Scinocca, J., Shepherd, T. G., Shibata, K., Smale, D., Teyssedre, H., Tian, W., Waugh, D., and Yamashita, Y.: Multimodel climate and variability of the stratosphere, J. Geophys. Res. A, 116, https://doi.org/10.1029/2010JD014995, 2011.

Chabrillat, S., Vigouroux, C., Christophe, Y., Engel, A., Errera, Q., Minganti, D., Monge-Sanz, B. M., Segers, A., and Mahieu, E.: Comparison of mean age of air in five reanalyses using the BASCOE transport model, Atmospheric Chemistry and Physics, 18, 14 715–14 735, https://doi.org/10.5194/acp-18-14715-2018, 2018.

Chapman, S.: A theory of upper atmospheric ozone, Mem. Roy. Soc., 3, 103–109, 1930.

Charlesworth, E., Plöger, F., Birner, T., Baikhadzhaev, R., Abalos, M., Abraham, N. L., Akiyoshi, H., Bekki, S., Dennison, F., Jöckel, P., Keeble, J., Kinnison, D., Morgenstern, O., Plummer, D., Rozanov, E., Strode, S., Zeng, G., Egorova, T., and Riese, M.: Stratospheric water vapor affecting atmospheric circulation, Nat. Commun., 14, 3925, https://doi.org/https://doi.org/10.1038/s41467-023-39559-2, 2023.

Charney, J. G. and Drazin, P. G.: Propagation of planetary-scale disturbances from the lower into the upper atmosphere, J. Geophys. Res., 66, 83–109, https://doi.org/10.1029/JZ066i001p00083, 1961.

Crutzen, P. J.: The influence of nitrogen oxides on the atmospheric ozone content, Q. J. R. Meteorol. Soc., 96, 320–325, 1970.

de Bort, T.: Variations de la température de l'air libre, dans la zone comprise entre 8 et 15 kilomètres d'altitude, C. R. Acad. Sci., 134, 987–989, 1902.

Dee, D. P., Uppala, S. M., Simmons, A. J., Berrisford, P., Poli, P., Kobayashi, S., Andrae, U., Balmaseda, M. A., Balsamo, G., Bauer, P., Bechtold, P., Beljaars, A. C. M., van de Berg, L., Bidlot, J., Bormann, N., Delsol, C., Dragani, R., Fuentes, M., Geer, A. J., Haimberger, L., Healy, S. B., Hersbach, H., Hólm, E. V., Isaksen, L., Kållberg, P., Köhler, M., Matricardi, M., McNally, A. P., Monge-Sanz, B. M., Morcrette, J.-J., Park, B.-K., Peubey, C., de Rosnay, P., Tavolato, C., Thépaut, J.-N., and Vitart, F.: The ERA-Interim reanalysis: configuration and performance of the data assimilation system, Q. J. R. Meteorol. Soc., 137, 553–597, https://doi.org/10.1002/qj.828, 2011.

Diallo, M., Konopka, P., Santee, M. L., Müller, R., Tao, M., Walker, K. A., Legras, B., Riese, M., Ern, M., and Ploeger, F.: Structural changes in the shallow and transition branch of the Brewer–Dobson circulation induced by El Niño, Atmos. Chem. Phys., 19, 425–446, https://doi.org/10.5194/acp-19-425-2019, 2019.

Dobson, G. M. B.: Origin and distribution of polyatomic molecules in the atmosphere, Proc R Soc London A, 236, 187–193, 1956.

Dobson, G. M. B., Harrison, D. N., and Lawrence, J.: Measurements of the amount of ozone in the Earth's atmosphere and its relation to other geophysical conditions. Part III, Proc. R. Soc. London A, 122, 456–486, 1929.

Eichinger, R., Garny, H., Šácha, P., Danker, J., Dietmüller, S., and Oberländer-Hayn, S.: Effects of missing gravity waves on stratospheric dynamics; part 1: climatology, Climate Dynamics, 54, 3165–3183, https://doi.org/https://doi.org/10.1007/s00382-020-05166-w, 2020.

Eluszkiewicz, J., Hemler, R., Mahlman, J., Bruhwiler, L., and Takacs, L.: Sensitivity of age-of-air calculations to the choice of advection scheme, J. Atmos. Sci., 57, 3185–3201, 2000.

Ern, M. and Preusse, P.: Wave fluxes of equatorial Kelvin waves and QBO zonal wind forcing derived from SABER and ECMWF temperature space-time spectra, Atmospheric Chemistry and Physics, 9, 3957–3986, https://doi.org/10.5194/acp-9-3957-2009, 2009.

Forster, P. and Shine, K. P.: Stratospheric water vapour change as possible contributor to observed stratospheric cooling, Geophys. Res. Lett., 26, 3309 – 3312, https://doi.org/10.1029/1999GL010487, 1999.

Fu, Q., Solomon, S., Pahlavan, H. A., and Lin, P.: Observed changes in Brewer–Dobson circulation for 1980–2018, Environ. Res. Lett., 14, https://doi.org/10.1088/1748-9326/AB4DE7, 2019.

Fujiwara, M., Manney, G. L., Gray, L. J., and Wright, J. S., eds.: SPARC Reanalysis Intercomparison Project (S-RIP) Final Report, SPARC Report No. 10, WCRP-6/2021, https://doi.org/10.17874/800dee57d13, 2022.

Garny, H., Birner, T., Bönisch, H., and Bunzel, F.: The effects of mixing on Age of Air, J. Geophys. Res., 119, https://doi.org/10.1002/2013JD021417, 2014.

Garny, H., Ploeger, F., Abalos, M., Bönisch, H., Castillo, A. E., von Clarmann, T., Diallo, M., Engel, A., Laube, J. C., Linz, M., Neu, J. L., Podglajen, A., Ray, E., Rivoire, L., Saunders, L. N., Stiller, G., Voet, F., Wagenhäuser, T., and Walker, K. A.: Age of Stratospheric Air: Progress on Processes, Observations, and Long-Term Trends, Reviews of Geophysics, 62, e2023RG000 832, https://doi.org/https://doi.org/10.1029/2023RG000832, e2023RG000832 2023RG000832, 2024.

Gelaro, R., McCarty, W., Suárez, M. J., Todling, R., Molod, A., Takacs, L., Randles, C. A., Darmenov, A., Bosilovich, M. G., Reichle, R., Wargan, K., Coy, L., Cullather, R., Draper, C., Akella, S., Buchard, V., Conaty, A., da Silva, A. M., Gu, W., Kim, G.-K., Koster, R., Lucchesi, R., Merkova, D., Nielsen, J. E., Partyka, G., Pawson, S., Putman, W., Rienecker, M., Schubert, S. D., Sienkiewicz, M., and Zhao, B.: The Modern-Era Retrospective Analysis for Research and Applications, Version 2 (MERRA-2), jci, 30, 5419–5454, 2017.

Gerber, E. P.: Stratospheric versus Tropospheric Control of the Strength and Structure of the Brewer-Dobson Circulation, J. Atmos. Sci., 69, 2857–2877, 2012.

Ghinassi, P., Fabiano, F., and Corti, S.: How well is Rossby wave activity represented in the PRIMAVERA coupled simulations?, Weather and Climate Dynamics, 3, 209–230, https://doi.org/10.5194/wcd-3-209-2022, 2022.

Hall, T. M. and Plumb, R. A.: Age as a diagnostic of stratospheric transport, J. Geophys. Res., 99, 1059–1070, 1994.

Haynes, P. H., Marks, C. J., McIntyre, M. E., Shepherd, T. G., and Shine, K. P.: On the "downward control" of extratropical diabatic circulations by eddy-induced mean zonal forces., J. Atmos. Sci., 48, 651–678, 1991.

Hersbach, H., Bell, B., Berrisford, P., Hirahara, S., Horànyi, A., Muñoz Sabater, J., Nicolas, J., Peubey, C., Radu, R., Schepers, D., Simmons, A., Soci, C., Abdalla, S., Abellan, X., Balsamo, G., Bechtold, P., Biavati, G., Bidlot, J., Bonavita, M., De Chiara, G., Dahlgren, P., Dee, D., Diamantakis, M., Dragani, R., Flemming, J., Forbes, R., Fuentes, M., Geer, A., Haimberger, L., Healy, S., Hogan, R. J., Hólm, E., Janiskovà, M., Keeley, S., Laloyaux, P., Lopez, P., Lupu, C., Radnoti, G., de Rosnay, P., Rozum, I., Vamborg, F., Villaume, S., and Thépaut, J.-N.: The ERA5 global reanalysis, Q. J. R. Meteorol. Soc., 146, 1999–2049, https://doi.org/10.1002/qj.3803, 2020.

Hitchman, M. H. and Huesmann, A. S.: A Seasonal Climatology of Rossby Wave Breaking in the 320–2000-K Layer, Journal of the Atmospheric Sciences, 64, 1922 – 1940, https://doi.org/10.1175/JAS3927.1, 2007.

Hoffmann, L., Günther, G., Li, D., Stein, O., Wu, X., Griessbach, S., Heng, Y., Konopka, P., Müller, R., Vogel, B., and Wright, J. S.: From ERA-Interim to ERA5: the considerable impact of ECMWF's next-generation reanalysis on Lagrangian transport simulations, Atmos. Chem. Phys., 19, 3097–3124, https://doi.org/10.5194/acp-19-3097-2019, 2019.

Holton, J. R., Haynes, P., McIntyre, M. E., Douglass, A. R., Rood, R. B., and Pfister, L.: Stratosphere-troposphere exchange, Rev. Geophys., 33, 403–439, 1995.

Kim, J.-E. and Alexander, M. J.: Direct impacts of waves on tropical cold point tropopause temperature, Geophys. Res. Lett., 42, 1584–1592, https://doi.org/10.1002/2014GL062737, 2015.

Kobayashi, S., Ota, Y., Harada, Y., Ebita, A., Moriya, M., Onoda, H., Onogi, K., Kamahori, H., Kobayashi, C., Endo, H., Miyaoka, K., and Takahashi, K.: The JRA–55 Reanalysis: General specifications and basic characteristics, J. Meteorol. Soc. Jpn., 93, 5–48, 2015.

Konopka, P., Steinhorst, H.-M., Grooß, J.-U., Günther, G., Müller, R., Elkins, J. W., Jost, H.-J., Richard, E., Schmidt, U., Toon, G., and McKenna, D. S.: Mixing and Ozone Loss in the 1999-2000 Arctic Vortex: Simulations with the 3-dimensional Chemical Lagrangian Model of the Stratosphere (CLaMS), J. Geophys. Res., 109, D02315, https://doi.org/10.1029/2003JD003792, 2004.

Koval, A. V., Toptunova, O. N., Motsakov, M. A., Didenko, K. A., Ermakova, T. S., Gavrilov, N. M., and Rozanov, E. V.: Numerical modelling of relative contribution of planetary waves to the atmospheric circulation, Atmospheric Chemistry and Physics, 23, 4105–4114, https://doi.org/10.5194/acp-23-4105-2023, 2023.

LeTexier, H., Solomon, S., and Garcia, R. R.: The role of molecular hydrogen and methane oxidation in the water vapour budget of the stratosphere, Q. J. R. Meteorol. Soc., 114, 281 – 295, 1988.

Lin, J., Brunner, D., Gerbig, C., Stohl, A., Luhar, A., and Webley, P., eds.: Lagrangian Modeling of the Atmosphere, vol. 200, American Geophysical Union, Washington, DC, 2013.

Linz, M., Plumb, R. A., Gerber, E. P., Haenel, F. J., Stiller, G., Kinnison, D., Ming, A., and Neu, J. L.: The strength of the meridional overturning circulation of the stratosphere, Nat. Geosci., 10, 663–667, 2017.

Mahieu, E., Chipperfield, M. P., Notholt, J., Reddmann, T., Anderson, J., Bernath, P. F., Blumenstock, T., Coffey, M. T., Dhomse, S. S., Feng, W., Franco, B., Froidevaux, L., Griffith, D. W. T., Hannigan, J. W., Hase, F., Hossaini, R., Jones, N. B., Morino, I., Murata, I., Nakajima, H., Palm, M., Paton-Walsh, C., III, J. M. R., Schneider, M., Servais, C., Smale, D., and Walker, K. A.: Recent Northern Hemisphere stratospheric HCl increase due to atmospheric circulation changes, Nature, 515, 104–107, https://doi.org/10.1038/nature13857, 2014.

Masson-Delmotte, V., Zhai, P., Pirani, A., Connors, S., Péan, C., Berger, S., Caud, N., Chen, Y., Goldfarb, L., Gomis, M., Huang, M., Leitzell, K., Lonnoy, E., Matthews, J., Maycock, T., Waterfield, T., Yu, O. Y. R., and Zhou, B., eds.: Climate Change 2021: The

Physical Science Basis. Contribution of Working Group I to the Sixth Assessment Report of the Intergovernmental Panel on Climate Change, Cambridge University Press, Cambridge, UK and New York, NY, USA, 2021.

Molina, M. J. and Rowland, F. S.: Stratospheric sink for chlorofluoromethanes: chlorine atom-catalysed destruction of ozone, Nature, 249, 810–812, 1974.

Morgenstern, O., Braesicke, P., Hurwitz, M. M., O'Connor, F. M., Bushell, A. C., Johnson, C. E., and Pyle, J. A.: The world avoided by the Montreal protocol, Geophys. Res. Lett., 35, L16811, https://doi.org/10.1029/2008GL034590, 2008.

Müller, S. K., Manzini, E., Giorgetta, M., Sato, K., and Nasuno, T.: Convectively Generated Gravity Waves in High Resolution Models of Tropical Dynamics, Journal of Advances in Modeling Earth Systems, 10, 2564–2588, https://doi.org/https://doi.org/10.1029/2018MS001390, 2018.

Newman, P. A., Oman, L. D., Douglass, A. R., Fleming, E. L., Frith, S. M., Hurwitz, M. M., Kawa, S. R., Jackman, C. H., Krotkov, N. A., Nash, E. R., Nielsen, J. E., Pawson, S., Stolarski, R. S., and Velders, G. J. M.: What would have happened to the ozone layer if chlorofluorocarbons (CFCs) had not been regulated?, Atmos. Chem. Phys., 9, 2113–2128, https://doi.org/10.5194/acp-9-2113-2009, 2009.

NOAA: Layers of the Atmosphere, URL https://www.noaa.gov/jetstream/atmosphere/layers-of-atmosphere, 2024.

NOAA: Chromatograph for Atmospheric Trace Species (CATS) in situ Halocarbons Program, URL https://gml.noaa.gov/hats/insitu/cats/, 2025.

Nyquist, H.: Certain topics in telegraph transmission theory, Transactions of the American Institute of Electrical Engineers, 47, 617–644, https://doi.org/10.1109/T-AIEE.1928.5055024, 1928.

Ploeger, F., Riese, M., Haenel, F., P.Konopka, Müller, R., and Stiller, G.: Variability of stratospheric mean age of air and of the local effects of residual circulation and eddy mixing, J. Geophys. Res., 120, 716–733, https://doi.org/10.1002/2014JD022468, 2015.

Ploeger, F., Legras, B., Charlesworth, E., Yan, X., Diallo, M., Konopka, P., Birner, T., Tao, M., Engel, A., and Riese, M.: How robust are stratospheric age of air trends from different reanalyses?, Atmos. Chem. Phys., 19, 6085–6105, https://doi.org/10.5194/gmd-12-2441-2019, 2019.

Ploeger, F., Diallo, M., Charlesworth, E., Konopka, P., Legras, B., Laube, J. C., Grooß, J.-U., Günther, G., Engel, A., and Riese, M.: The stratospheric Brewer–Dobson circulation inferred from age of air in the ERA5 reanalysis, Atmos. Chem. Phys. Discuss., pp. 1–27, https://doi.org/10.5194/acp-2020-1253, 2021.

Plumb, R. A.: Stratospheric transport, J. Meteorol. Soc. Jpn., 80, 793–809, 2002.

Polvani, L. M., Waugh, D. W., Correa, G. J. P., and Son, S.-W.: Stratospheric Ozone Depletion: The Main Driver of Twentieth-Century Atmospheric Circulation Changes in the Southern Hemisphere, Journal of Climate, 24, 795 – 812, https://doi.org/10.1175/2010JCLI3772.1, 2011.

Polvani, L. M., Abalos, M., garcia, R., Kinnison, D., and Randel, W. J.: Significant weakening of Brewer-Dobson circulation trends over the 21st century as a consequence of the Montreal protocol, Geophys. Res. Lett., 45, 401–409, 2018.

Pommrich, R., Müller, R., Grooß, J.-U., Konopka, P., Ploeger, F., Vogel, B., Tao, M., Hoppe, C. M., Günther, G., Spelten, N., Hoffmann, L., Pumphrey, H.-C., Viciani, S., D'Amato, F., Volk, C. M., Hoor, P., Schlager, H., and Riese, M.: Tropical troposphere to stratosphere transport of carbon monoxide and long-lived trace species in the Chemical Lagrangian Model of the Stratosphere (CLaMS), Geosci. Model Dev., 7, 2895–2916, https://doi.org/10.5194/gmd-7-2895-2014, 2014.

Prather, M. J., Hsu, J., DeLuca, N. M., Jackman, C. H., Oman, L. D., Douglass, A. R., Fleming, E. L., Strahan, S. E., Steenrod, S. D., Søvde, O. A., Isaksen, I. S., Froidevaux, L., and Funke, B.: Measuring and modeling the lifetime of nitrous oxide including its variability, J Geophys Res Atmos., 120, 5693–5705, https://doi.org/10.1002/2015JD023267, 2015.

Ramaswamy, V., Chanin, M. L., Angell, J., Barnett, J., Gaffen, D., Gelman, M., Keckhut, P., Koshelkov, Y., K., K. L., Lin, J. J. R., O'Neill, A., Nash, J., Randel, W., Rood, R., Shine, K., Shiotani, M., and Swinbank, R.: Stratospheric temperature trends: Observations and model simulations, Rev. Geophys., 39, 71–122, 2001.

Randel, W. J., Garcia, R. R., and Wu, F.: Dynamical balances and tropical stratospheric upwelling, J. Atmos. Sci., 65, 3584–3595, https://doi.org/{10.1175/2008JAS2756.1}, 2008.

Ray, E. A., Moore, F. L., Rosenlof, K. H., Davis, S. M., Sweeney, C., Tans, P., Wang, T., Elkins, J. W., Boenisch, H., Engel, A., Sugawara, S., Nakazawa, T., and Aoki, S.: Improving stratospheric transport trend analysis based on SF_6 and CO_2 measurements, J. Geophys. Res., 119, 14 110–14 128, 2014.

Riese, M., Ploeger, F., Rap, A., Vogel, B., Konopka, P., Dameris, M., and Forster, P.: Impact of uncertainties in atmospheric mixing on simulated UTLS composition and related radiative effects, J. Geophys. Res., 117, D16305, https://doi.org/10.1029/2012JD017751, 2012.

Rosenlof, K. H., Tuck, A. F., Kelly, K. K., Russell III, J. M., and McCormick, M. P.: Hemispheric asymmetries in the water vapor and inferences about transport in the lower stratosphere, J. Geophys. Res., 102, 13 213–13 234, https://doi.org/{10.1029/97JD00873}, 1997.

Russell, J. M., Gordley, L. L., Park, J. H., Drayson, S. R., Tuck, A. F., Harries, J. E., Cicerone, R. J., Crutzen, P. J., and Frederick, J. E.: The Halogen Occultation Experiment, J. Geophys. Res., 98, 10 777–10 797, 1993.

Seviour, W. J. M., Butchart, N., and Hardiman, S. C.: The Brewer-Dobson circulation inferred form ERA-Interim, Q. J. R. Meteorol. Soc., 138, 878–888, 2011.

Shannon, C. E.: Communication in the Presence of Noise, Proceedings of the IRE, 37, 10–21, https://doi.org/10.1109/JRPROC.1949.232969, 1949.

Skamarock, W. C.: Evaluating Mesoscale NWP Models Using Kinetic Energy Spectra, Monthly Weather Review, 132, 3019 – 3032, https://doi.org/10.1175/MWR2830.1, 2004.

Smith, A. K., Preusse, P., and Oberheide, J.: Middle atmosphere Kelvin waves observed in Cryogenic Infrared Spectrometers and Telescopes for the Atmosphere (CRISTA) 1 and 2 temperature and trace species, J. Geophys. Res. A, 107, 5–1–5–22, https://doi.org/https://doi.org/10.1029/2001JD000577, 2002.

Solomon, S.: Stratospheric ozone depletion: A review of concepts and history, Rev. Geophys., 37, 275–316, https://doi.org/10.1029/1999RG900008, 1999.

Solomon, S., Rosenlof, K., Portmann, R., Daniel, J., Davis, S., Sanford, T., and Plattner, G.-K.: Contributions of stratospheric water vapor to decadal changes in the rate of global warming, Science, 327, 1219–1223, https://doi.org/10.1126/science.1182488, 2010.

Stiller, G. P., Fierli, F., Ploeger, F., Cagnazzo, C., Funke, B., Haenel, F., Reddmann, T., Riese, M., and von Clarmann, T.: Shift of subtropical transport barriers explains observed hemispheric asymmetry of decadal trends of age of air, Atmos. Chem. Phys., 17, 11 177–11 192, 2017.

Strube, C., Ern, M., Preusse, P., and Riese, M.: Removing spurious inertial instability signals from gravity wave temperature perturbations using spectral filtering methods, Atmospheric Measurement Techniques, 13, 4927–4945, https://doi.org/10.5194/amt-13-4927-2020, 2020.

Vallis, G. K.: Atmospheric and oceanic fluid dynamics, Cambridge University Press, 2006.

Velders, G. J. M., Andersen, S. O., Daniel, J. S., Fahey, D. W., and McFarland, M.: The importance of the Montreal Protocol in protecting climate, Proc. Natl. Acad. Sci., 104, 4814–4819, https://doi.org/10.1073/pnas.0610328104, 2007.

Watanabe, S., Sato, K., Kawatani, Y., and Takahashi, M.: Vertical resolution dependence of gravity wave momentum flux simulated by an atmospheric general circulation model, Geoscientific Model Development, 8, 1637–1644, https://doi.org/10.5194/gmd-8-1637-2015, 2015.

Waugh, D. W.: The age of stratospheric air, Nature Geoscience, 2, 14–16, 2009.

Waugh, D. W. and Hall, T. M.: Age of stratospheric air: Theory, observations, and models, Rev. Geophys., 40, 1–27, 2002.

WMO: Scientific assessment of ozone depletion: 2022, GAW Report No. 278, WMO:Geneva, Switzerland, 2022.

Yang, G.-Y., Hoskins, B., and J., S.: Convectively Coupled Equatorial Waves: A New Methodology for Identifying Wave Structures in Observational Data, J. Atmos. Sci., 60, 1637–1654, https://doi.org/https://doi.org/10.1175/1520-0469(2003)060<1637:CCEWAN>2.0.CO;2, 2003.

Yasui, R., Sato, K., and Miyoshi, Y.: Roles of Rossby Waves, Rossby–Gravity Waves, and Gravity Waves Generated in the Middle Atmosphere for Interhemispheric Coupling, Journal of the Atmospheric Sciences, 78, 3867 – 3888, https://doi.org/10.1175/JAS-D-21-0045.1, 2021.

Žagar, N., Jelić, D., Alexander, M. J., and Manzini, E.: Estimating Subseasonal Variability and Trends in Global Atmosphere Using Reanalysis Data, Geophysical Research Letters, 45, 12,999–13,007, https://doi.org/https://doi.org/10.1029/2018GL080051, 2018.

Acknowledgments

Praise be to God.

I would like to express my appreciation to Felix Ploeger, Peter Preusse, and Manfred Ern. Their guidance and invaluable advice during our meetings were instrumental in resolving the challenges that arose during my research. A special thank you to Felix Ploeger for sharing his profound expertise in transport processes in the stratosphere and the Brewer-Dobson circulation, which greatly enriched this work. I am also incredibly grateful to Felix Ploeger and Jan Kaumanns for their meticulous proofreading of this thesis and their insightful feedback. My sincere thanks extend to all the members of ICE-4. Your collective efforts have made this a very good place to work and conduct research. Furthermore, I wish to acknowledge the developers of modern AI-based language software, which helped correct and improve the language throughout this thesis. Finally, I would like to extend my heartfelt thanks to my family and friends. Your unwavering support whenever it was needed has been a constant source of strength and encouragement.

Schriften des Forschungszentrums Jülich
Reihe Energie & Umwelt / Energy & Environment

Band / Volume 723
Geophysical characterization of landscapes along a climate and vegetation gradient in the Chilean coastal cordillera
I. Dal Bo (2026), 138 pp
ISBN: 978-3-95806-956-5 (Print)
ISBN: 978-3-95806-957-2 (E-Book)

Band / Volume 724
Model informed assessment of observation impact for emission rate optimization using four-dimensional variational data assimilation
A. Hermanns (2026), xvi, 109 Seiten
ISBN: 978-3-95806-958-9 (Print)
ISBN: 978-3-95806-959-6 (E-Book)

Band / Volume 725
Synthese und Bewertung hochaktiver Katalysatoren zur Herstellung höherer Alkohole aus Methanol als Kraftstoff
J. Häusler (2026), xiii, 265 Seiten
ISBN: 978-3-95806-962-6 (Print)
ISBN: 978-3-95806-963-3 (E-Book)

Band / Volume 726
Development and Characterization of Ni_3Fe Layered Double Hydroxide-Based Oxygen-Evolution Electrodes for Anion Exchange Membrane Water Electrolysis
I.Galkina (2026), vii, 173, xxxiii Seiten
ISBN: 978-3-95806-966-4 (Print)
ISBN: 978-3-95806-967-1 (E-Book)

Band / Volume 727
Surface Regeneration of Plasma-Facing Components by Wire-Based Laser Metal Deposition
J. Tweer (2026), XX, 186 pp
ISBN: 978-3-95806-970-1 (Print)
ISBN: 978-3-95806-971-8 (E-Book)

Band / Volume 728
Reducing the noble metal and titanium content of anode PTLs in PEM water electrolysis – performance and degradation
S. Zerressen (2026), XIII, 235 pp
ISBN: 978-3-95806-972-5 (Print)
ISBN: 978-3-95806-973-2 (E-Book)

Band / Volume 729
Gasfernleitungsnetze und deren Umstellung auf Wasserstoff
T. A. Triesch (2026), 364 pp
ISBN: 978-3-95806-978-7 (Print)
ISBN: 978-3-95806-979-4 (E-Book)

Band / Volume 730
Land-Atmosphere Coupling in a Changing Climate: Understanding Variability, Extremes, and Human Influence through Regional Climate Modeling
Y. Zhang (2026), 135 pp
ISBN: 978-3-95806-980-0 (Print)
ISBN: 978-3-95806-981-7 (E-Book)

Band / Volume 731
Abbildung gekoppelter Infrastrukturen in Energiesystemmodellen
P. Freitag (2026), XIX, 322 pp
ISBN: 978-3-95806-984-8 (Print)
ISBN: 978-3-95806-985-5 (E-Book)

Band / Volume 732
Cost-reduced and Sustainable Interconnects and their Coatings for Solid Oxide Cells
M. Hilger (2026), viii, 185 pp
ISBN: 978-3-95806-988-6 (Print)
ISBN: 978-3-95806-989-3 (E-Book)

Band / Volume 733
Liquid-Phase Synthesis of Silicon and Silicon Carbide Thin-Films via Atmospheric Pressure Chemical Vapor Deposition
B. Fischer (2026), xxii, 211, A15 pp
ISBN: 978-3-95806-990-9 (Print)
ISBN: 978-3-95806-991-6 (E-Book)

Band / Volume 734
Modellgestützte Transformationspfade des deutschen Energiesystems
R. Maier (2026), xxvii, 331 pp
ISBN 978-3-95806-994-7 (Print)
ISBN 978-3-95806-995-4 (E-Book)

Band / Volume 735
Dynamical drivers of deep and shallow branches in the stratospheric circulation and transport
R.- A. Baikhadzhaev (2026), 120 pp
ISBN 978-3-95806-996-1 (Print)
ISBN 978-3-95806-997-8 (E-Book)

Energie & Umwelt / Energy & Environment
Band / Volume 735
ISBN 978-3-95806-997-8

Mitglied der Helmholtz-Gemeinschaft

JÜLICH
Forschungszentrum